Design of Bulk Nanocrystalline Tungsten Alloys via Nano-Phase Separation Sintering

by

Mansoo Park

B.S., Materials Science and Engineering

Seoul National University, 2010

Submitted to the Department of Materials Science and Engineering
in Partial Fulfilment of the Requirements for the Degree of

Doctor of Philosophy in Materials Science and Engineering
at the
MASSACHUSETTS INSTITUTE OF TECHNOLOGY

February 2015

Signature redacted

Signature of Author: .....
Department of Materials Science and Engineering
January 16, 2015

Signature redacted

Certified by:.....
Christopher A. Schuh
Danae and Vasilis Salapatas Professor of Metallurgy
Thesis Supervisor

Signature redacted

Accepted by:.....
Donald Sadoway
Chair, Departmental Committee for Graduate Students

Design of Bulk Nanocrystalline Tungsten Alloys via Nano-Phase Separation Sintering

by

Mansoo Park

Submitted to the Department of Materials Science and Engineering
on January 16, 2015 in Partial Fulfilment of the Requirements for the
Degree of Doctor of Philosophy in Materials Science and Engineering

ABSTRACT

An accelerated sintering method called 'nano-phase separation sintering' is developed, with specific applicability to nanostructured tungsten alloys. Nanocrystalline tungsten alloys containing minority additions of chromium are produced by high-energy ball milling and then consolidated. Such alloys exhibit the onset of sintering at a very low temperature around 950 °C and a very rapid rate of densification. The mechanism of this accelerated sintering is established through understanding the role of nano-scale, solid second phase precipitation during the sintering cycle, as analyzed by thermomechanical analysis, electron microscopy and x-ray diffraction. In addition, control experiments are used to establish that the accelerated sintering is apparently accomplished from the combination of two features of the powders: (i) nanocrystallinity and (ii) alloy supersaturation. In addition to accelerating sintering, the incorporation of alloying elements and second phases are also beneficial for mitigating grain growth during a thermal cycle, so nano-phase separation sintering is thus naturally appropriate to the production of fine-grained bulk materials. Sintered compacts achieved through nano-phase separation sintering display 10~30 times smaller grain sizes at comparable densities than those produced by conventional accelerated sintering methods such as solid-state activated sintering and liquid phase sintering. The thermodynamic features and conditions for nano-phase separation sintering are further explored based on the binary phase diagram in order to generalize the concept to other alloy systems. After presenting a series of proposed alloy design rules, the consolidation of chromium with an addition of nickel is accelerated. Prospects of the technique for the development of full density bulk products in more complex alloy systems are also discussed.

Thesis Supervisor: Christopher A. Schuh

Title: Department Head, Danae and Vasilis Salapatas Professor of Metallurgy

Acknowledgements

I would appreciate the members of my thesis committee, Professor Yet-Ming Chiang and Professor Thomas Eagar for their guidance and insightful comments. I certainly believe that their comments have made my thesis stronger and more advanced.

I would like to specially thank my advisor, Professor Chris Schuh with my deepest respect for immeasurably encouraging and inspiring me. Before coming to MIT, I had been looking for an advisor whom I would admire personally as well as academically. I has been assured that he is the very one and I have always thought that I am blessed to accompany him throughout my Ph.D. journey. Although my four-year journey had not been easy and sometimes faced a big wave, I was able to overcome it and safely arrive the final destination thanks to his solid support and encouragement like a ballast to set up my central.

I am very grateful to all members in Schuh research group. They have been very kind and made my lab life so enjoyable. They have been always willing to help me out and given advice. I learned a lot academically and personally from conversations I had with them. I would like especially thank to Tongjai who tough me everything related to experiments and research from the very beginning when I joined in this group to the end.

I would like thank KGMSE for their support and especially Donghun and Yongwoo who have enriched my life at MIT. I truly relished every moment of my life with them. And last but not least, I am forever grateful to my family for being always there for me.

Table of contents

List of Figures

List of Tables

Chapter 1 Introduction

1.1 Tungsten sintering

Tungsten, one of the refractory metals, has the highest melting temperature, 3422 °C, among all metals, as well as high strength and density. Because of its intrinsically high melting point, sintering of tungsten is economically and technically preferred to melt casting when producing a bulk shape. Two methods of sintering are commonly employed: direct and indirect sintering (*1, 2*). In direct sintering, green compacts of tungsten are clamped by molybdenum or tungsten clips and then an electric current of several thousand amperes is passed through them. A schematic drawing of direct sintering is presented in Figure *1.1*. The current running through the compact is gradually raised until the temperature reaches 3100 °C. The soak time at the maximum temperature is between 30 and 60 minutes, which results in 88.5~96 % of the theoretical density of a final sintered product.

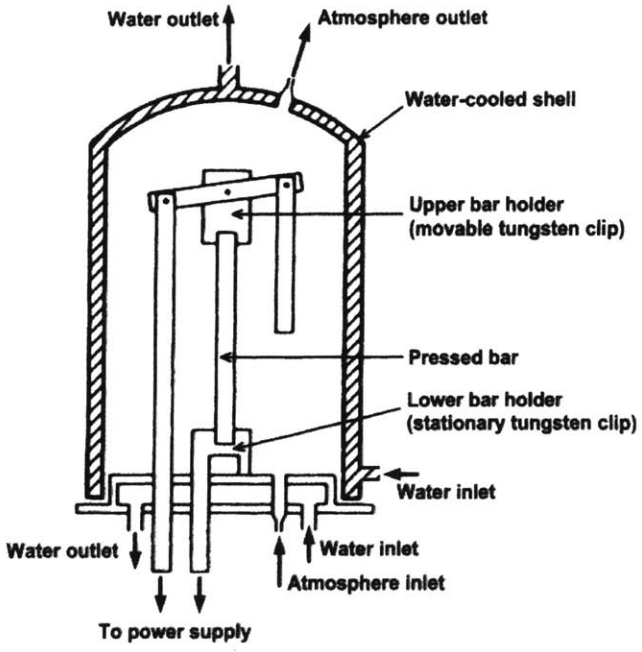

Figure 1.1 Schematic drawing of a direct sintering furnace *(1)*.

Indirect sintering uses a resistance element in order to generate heat, rather than directly Joule heating the compact. One of the advantages of indirect sintering is that is accommodates larger sized compacts than does direct sintering. Typical indirect sintering temperatures are between 2000 and 2700 °C and the temperature is usually held at the maximum for 6 to 10 hours (*1, 2*).

Whether direct or indirect sintering is employed for the production of bulk tungsten alloys, it is important to note that very high temperatures from 2000~3050 °C are generally required to achieve full density sintered compacts. Such temperatures are extremely challenging to work with at scale, degrade peripheral equipment relatively quickly, and have an associated high energy cost. For these reasons, it is has long been of interest to develop kinetically enhanced sintering methods for tungsten.

1.2 Enhanced tungsten sintering

1.2.1 Solid-state activated sintering

In 1959, Vacek (*3*) observed that a very small addition of nickel is highly effective in enhancing sintering kinetics of tungsten and lowering the sintering temperature to ~ 1200 °C. Since that observation, numerous research works have been conducted on the addition of transition metals such as Pd, Pt, Ni, Co and Fe into tungsten for the purpose of accelerating sintering (*4-15*). The effect has been called solid-state activated sintering.

The mechanism underlying activated sintering of tungsten has been widely studied and debated (*16-19*). Panichkina et al. (*15*) ascribed the low sintering temperature to the effects of transition elements to dislocation climb. Samsonov (*12*) suggested that the transfer of electrons from the additive to the d-orbital of tungsten could facilitate tungsten diffusion. Schintlmeister and

Richter (*14*) observed that the grain boundary diffusion rate of tungsten in Ni-doped tungsten is increased, as compared to pure tungsten. German and Munir (*7*) proposed that a Ni layer that develops on the surface of the tungsten particles provides a fast transport path for tungsten atoms, which increases tungsten diffusivity and densification rate.

In 2005, Luo et al. provided a thermodynamic and structural explanation for the solid-state activated sintering mechanism in refractory metals by employing the concept of grain boundary complexions (*20*). They first revealed the premelting of grain boundaries at 95 °C below the bulk eutectic temperature in Ni-doped W through high-resolution transmission electron microscopy (TEM) and Auger spectroscopy (*20*). Such premelting is referred to as a complexion transition at the grain boundary, and is associated with a rapid and discontinuous change in kinetic properties of the boundary. They therefore concluded that this nanometer thick disordered layer (analogous to amorphous phase) as shown in Figure 1.2 provides a fast transport layer to tungsten atoms, which accelerates sintering kinetics.

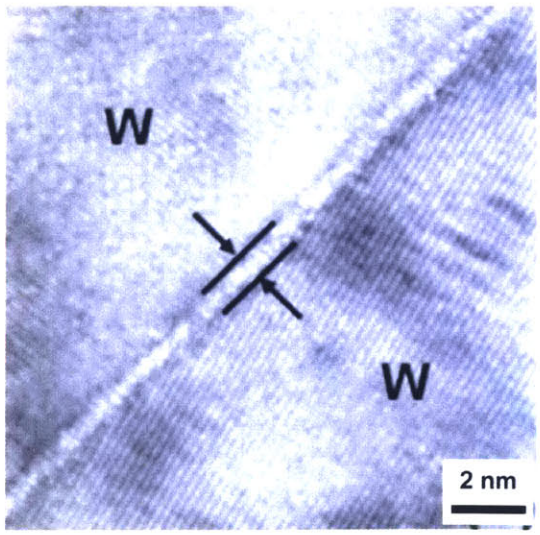

Figure 1.2 The nanometer thick quasi-liquid layer between tungsten particles in activated sintering *(21)*.

Luo and coworkers suggested that the stabilization of a nanometer thick quasi-liquid layer could be possible between powder particles even below the bulk melting temperature if the free energy penalty for forming the undercooled liquid film is overcompensated by the reduction in the interfacial energies as presented by Figure 1.3 and Eq. (1):

$$\Delta G_{amorph} h < \gamma_{gb} - 2\gamma_{cl} \equiv -\Delta\gamma \quad (1)$$

where ΔG_{amorph} is the change of free energy for forming an amorphous phase, h is the thickness of the amorphous layer, and γ_{gb}, γ_{cl} are the excess free energies for a grain boundary and crystal-liquid, respectively (*20*).

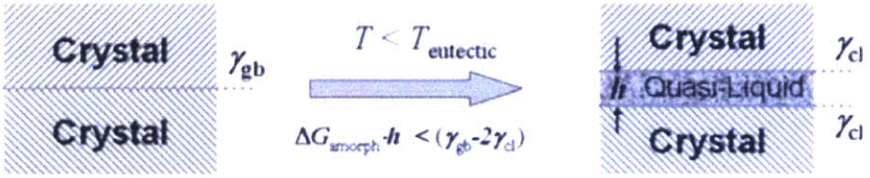

Figure 1.3 Schematic of the stabilization of a nanoscale quasi-liquid layer below the bulk eutectic temperature (*20*).

1.2.2 Liquid phase sintering

Liquid phase sintering refers to a sintering process facilitated by the formation of a liquid phase during sintering; an alloy containing more than one component, when sintered above the solidus line, will develop a second liquid phase. A liquid phase usually increases the densification rate for two reasons. First, the capillary force from the wetting liquid helps remove porosity by filling pores with liquid phase. Second, the diffusivities in liquid are relatively high, which allows faster bonding and densification (*22*). The theoretical foundations for the liquid phase sintering were established with a focus on tungsten heavy alloys (W-Ni-Fe and W-Ni-Cu), and since then liquid

phase sintering has been widely adopted for the manufacture of various products including refractory metals and ceramics (*22-28*). However, the accelerated kinetics associated with the presence of a liquid phase also lead to concomitant microstructural coarsening. *Figure 1.4* displays the final microstructure of the sintered tungsten alloy (W-1Ni-1Fe in wt.%) after liquid phase sintering, delineating average grain size ~50 μm which is 10 times larger than the initial particle size of 5 μm.

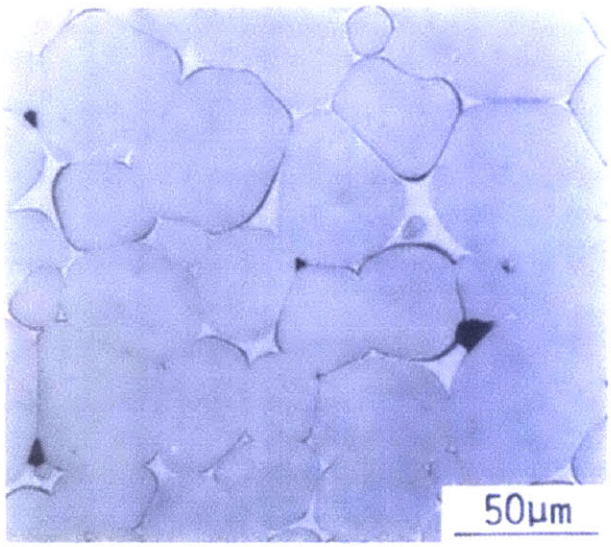

Figure 1.4 The microstructure of W-1Ni-1Fe specimen sintered at 1460 °C for 5 hours (*29*).

Even using nanopowders or nanocrystalline powders of tungsten alloy *(30, 31)* as an input for sintering, a sintered product with nanostructure has not yet proven possible to produce through liquid phase sintering. For example, nanocrystalline tungsten alloy powders of 93W-3.5Ni-1.5Fe-2.0Co and 93W-5.6Ni-1.4Fe in wt.%, both which had an average grain size of 16 nm before sintering, yielded final sintered products with grain sizes of ~15 and ~40 μm, respectively, achieved through liquid phase sintering as shown in Figure *1.5*.

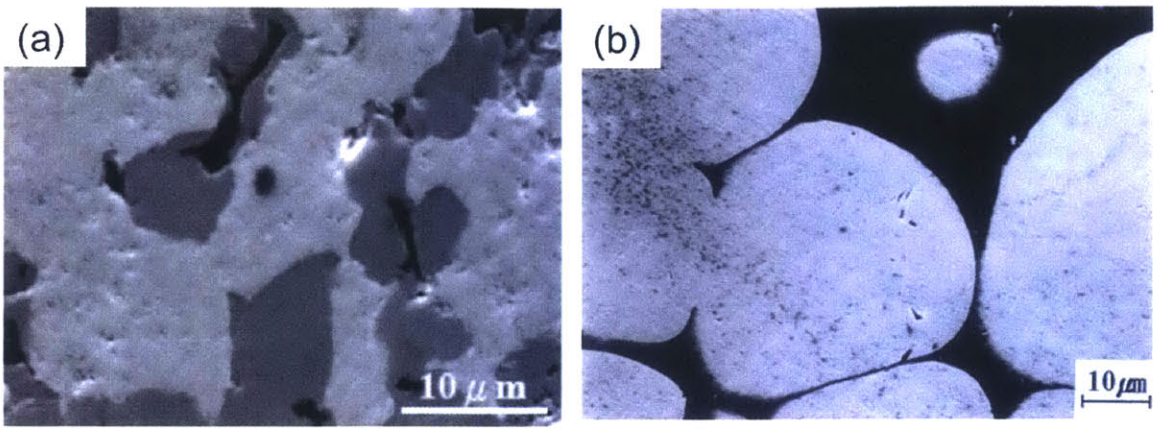

Figure 1.5 The secondary electron images after liquid phase sintering of (a) 93W-3.5Ni-1.5Fe-2.0Co alloy (*30*) and of (b) 93W-5.6Ni-1.4Fe (*32*).

1.3 Nanocrystalline tungsten

1.3.1 Properties of nanocrystalline tungsten

Unique properties, such as high strength and increased corrosion and creep resistance, can be realized in nanocrystalline metals (*33, 34*) with an average grain size typically smaller than 100 nm. Body-centered cubic (BCC) nanocrystalline metals have been of interest for unusual deformation phenomenon such as suppressed strain sensitivity (*35*) and localized shearing instead of uniform plastic deformation under high rate loading (*36-38*) as compared with microcrystalline materials of the same composition. BCC tungsten has been reported to show localized shearing and adiabatic shear banding when it is nanostructured, as shown in Figure *1.6*.

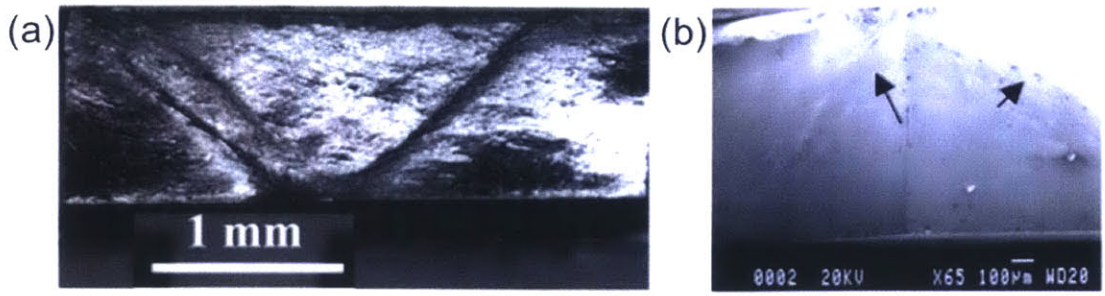

Figure 1.6 (a) Optical micrograph of and (b) Scanning electron microscopy (SEM) micrograph of adiabatic shear bands in nanocrystalline tungsten (*39*).

The formation of shear bands under high rate loading is desirable for a kinetic energy penetrator material, in that more energy should be conveyed to the object rather than dissipated for plastic deformation of the penetrator. There has been great deal of interest in nanocrystalline tungsten for kinetic energy penetrator applications as a prospective replacement for the chemically toxic depleted uranium, because of its intrinsically high density and strength (*36, 40-44*).

1.3.2 Methodologies for the production of nanocrystalline tungsten

Two general classes of processing methodology have been developed over the past few decades for manufacturing nanocrystalline materials: bottom-up and top-down approaches. Top-down approaches refine a bulk coarse grained material into the nanoscale regime. Bottom-up methods assemble bulk materials from nanostructured precursors.

One of the top-down methods for refining the grain size of tungsten is severe plastic deformation (SPD). SPD is an extension of the concept of "redundant work" (*45*), where excess shear strain is used for the sole purpose of accumulating defect energy and structural refinement. Two SPD techniques have become typical in the research community: equal-channel-angular-pressing (ECAP) and high-pressure torsion (HPT) as shown in *Figure 1.7* (*46*). ECAP can reduce the

grain size of tungsten only to a few micron sizes due to dynamic recrystallization and grain growth caused by its high processing temperature around 1000 °C (*43*). Therefore, a warm rolling process has been proposed as a follow-on process after ECAP to obtain a grain size in the ultra-fine grain regime (*39*). Another SPD processing method, HPT, is to apply high pressure and torsion to a disk shape of tungsten (*46*). After a large amount of plastic strain HPT yields a finer grain size about 100 nm (*43*). These SPD techniques produce W that exhibits elastic-perfectly-plastic deformation at room temperature (no strain hardening), considerably reduced strain rate sensitivity, and finally, shear localization in ultra-fine grained tungsten.

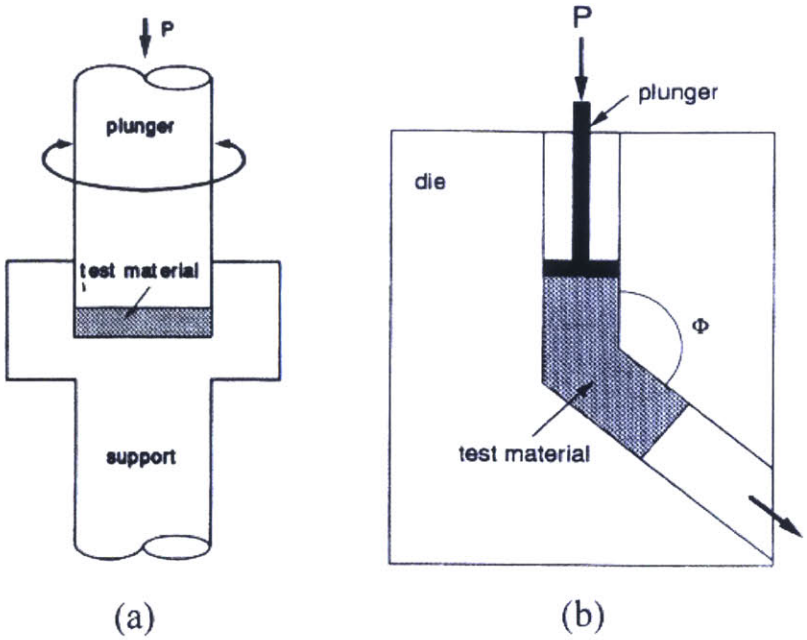

Figure 1.7 Principles of SPD methods: (a) high pressure torsion (HPT), (b) equal-channel-angular-pressing (ECAP) *(46).*

Despite these demonstrations aimed at producing nanocrystalline tungsten, there are several problems with bulk SPD techniques. First, these techniques dramatically limit the scale of the products. Second, the fine grain size is not stable, and will not likely be maintained if subsequent

processing such as hot shape forming is needed. Third, these techniques do not offer precise control over grain size.

For bottom-up methods, nano-sized or nanostructured particles should be synthesized first, and then these particles consolidated in a "two-step" process (*43*). Several studies proposed bottom-up methodology for nanocrystalline tungsten with powders synthesized through ball milling or high-energy milling (*32, 47-53*). Although they successfully achieved nano-sized grain tungsten (5~15 nm) in the powder particles, the nanostructure was highly susceptible to thermally activated grain growth during the consolidation process at high temperature (*54, 55*).

1.4 Research objectives and structure of thesis

The above studies suggest that conventional accelerated tungsten sintering methods including solid-state activated sintering and liquid phase sintering are not applicable to nanocrystalline tungsten powder and are not suitable for generating fine-grained structures. The aims of this thesis are to develop a new accelerated sintering method specifically applicable to nanocrystalline tungsten alloy powders and to achieve nanocrystalline bulk tungsten alloys via sintering without any external forces. This thesis is comprised of three main parts.

- Chapter 2: Nanocrystalline tungsten alloy powder is synthesized through a high-energy ball mill. The synthesized powders are physically and chemically characterized through electron microscopy and x-ray diffraction. Finally, thermal stability of the synthesized powders is confirmed.

- Chapter 3: Compacts of the as-processed powder are annealed and their length change is measured by a thermomechanical analyzer. Accelerated sintering is shown for alloys that contain Cr, and associated with structural changes. The resulting technique is referred to as "nano-phase separation sintering" because of the emergence of a second phase that accelerates densification. A comparison of this approach with conventional enhanced tungsten sintering (including solid-state activated sintering and liquid phase sintering) is presented.
- Chapter 4 and Chapter 5: Applications of nano-phase separation sintering are explored. First, the mechanism of nano-phase separation sintering is shown to be generally applied to other alloy systems to accelerate their consolidation. Second, nanocrystalline bulk tungsten alloy is achieved via nano-phase separation sintering.

Chapter 2 Synthesis and Characterization of Nanocrystalline Tungsten Powders

This thesis involved the production of powders of several different alloys, characterization of those powders, evaluation of the structural evolution of those powders upon heating, and finally characterization of the density and structural changes of the powders during a sintering cycle. To accomplish these studies, a number of techniques and procedures were used extensively.

The sections below begin by outlining the general procedures and experimental methods used before delving into any specific alloy system.

2.1 Synthesis and characterization procedures of powders

High-energy ball milling

The several powders were used in this thesis: average particle size (APS) 1~5 μm W powder (99.9 % purity), APS<10 μm Cr powder (99.2 % purity), APS 2~3 μm Ni powders (99.9 % purity), -150 mesh Ti powder (99.9 % purity), and they are all from Alfa Aesar. W and W alloys (W-Cr, W-Ti, W-Ti-Cr), and Cr alloys (Cr-Ni) powders were produced with those commodity powders. For the synthesis of nanocrystalline powder, high-energy ball milling was used, which leads to grain size refinement to the nanoscale. Powders were mechanically milled or alloyed by a SPEX 8000 high-energy ball mill in an high purity argon-filled glove box with 1 wt.% stearic acid as a process control agent. Tungsten carbide vial and a ball-to-powder ratio of 5 to 1 were used for milling. All synthesized powders use the same milling procedures except for milling time (corresponding milling time is specified in each section).

X-ray diffraction

X-ray diffraction (XRD) patterns were measured using a Panalytical X'Pert Pro diffractometer using Cu-Kα radiation at 45 kV and 40 mA. All alloyed powders were scanned from 30 to 120 ° using a step size of 0.0167 ° and time per step of 90 sec. The phases present, lattice parameters, and grain sizes were assessed by Rietveld refinement using a NIST LaB_6 standard.
In-situ XRD was measured using the Panalytical X'Pert Pro diffractometer with increasing temperature at a constant heating rate of 10 °C/min under flowing ultra-high purity argon. Diffraction patterns were collected at 850, 900, 950, 1000, and 1050 °C for three diffraction peaks around 40, 74, and 102 degrees (2 theta) to minimize phase evolution during measurement; each peak was scanned for less than 1 minute.

Electron microscopy

Powders were characterized using several different types of microscopy. An XL30 Environmental FEG SEM from Philips and FEI Helios NanoLab DualBeam focused in beam were used for imaging of the powders. TEM specimens were prepared by mixing the powder in epoxy, manually grinding a powder/epoxy disk until it was less than 1 μm thick, and then ion-milled by a Fischione 1010 ion mill maintained at -110 °C by liquid nitrogen. Bright-field images and diffraction patterns were acquired using a JEOL 2010F TEM operating at 200 kV. After individual grains were manually traced, an average grain size was estimated through their spherical-equivalent diameters measured. Scanning transmission electron microscopy (STEM) with energy dispersive spectroscopy (EDS) was used to obtain local composition measurements, elemental maps and imaging of structures after powder processing. The probe size used for measuring local composition was 0.2 nm.

Laser diffraction particle size analyzer

The particle sizes of all powders were measured using a laser diffraction particle size analyzer from Horiba LA950V2 which can measure particle sizes from 15 nm to few hundreds microns.

Thermomechanical analysis

Characterization of the density during a thermal exposure was accomplished by a thermomechanical analyzer (TMA). Powder was compacted by cold press into 6 mm diameter and 3~4 mm high cylindrical disks. This cold-pressed compact was then heated without applied pressure at a constant heating rate (10 °C/min) under flowing Ar+3% H_2 while measuring the change in compact density as a function of temperature and time with the TMA from Netzsch Instruments. The force on the compact from the alumina push-rod of the TMA was 100 nm.

2.2 Nanocrystalline tungsten

Nanocrystalline tungsten was produced through a high-energy ball mill using the procedure outlined in section 2.1. XRD patterns were acquired with various milling times as shown in Figure *2.1* to examine the milled structure and the change in the grain size. Broadening of tungsten peaks is observed in Figure *2.1* with milling time due to the grain size refinement and the strain from lattice defects. Crystallite refinement to the nanoscale occurs by continuous welding and fracturing during ball milling, and the average grain size of tungsten assessed by the Rietveld refinement method is reduced into around 20 nm after 6 hours of milling. As shown in Figure *2.1*, the peaks of tungsten carbide start to be noticeably detected after 6 hours of milling, which is obtained from the milling media. The as-milled grain size and the detection of impurity match those found in literature (*50*).

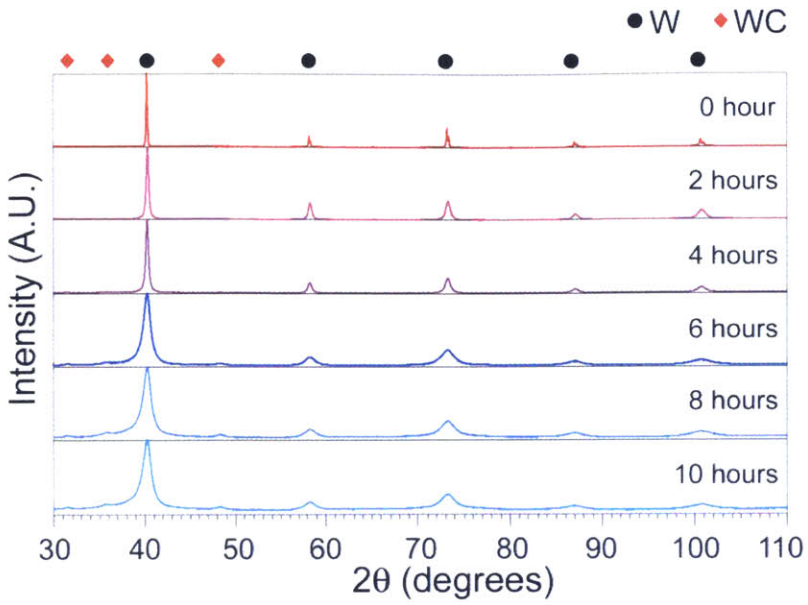

Figure 2.1 XRD patterns of ball-milled pure tungsten at different milling times (Courtesy of Dr. Chookajorn).

We constructed a baseline of the sintering curve of nanocrystalline W prepared using the same procedure outlined in section 2.1 for 20 hours of milling. The powder of nanocrystalline W was compacted by cold press into 6 mm diameter and 3~4 mm high cylindrical disks of 0.62 relative density. The change in compact density is shown in Figure *2.2* as a function of temperature.

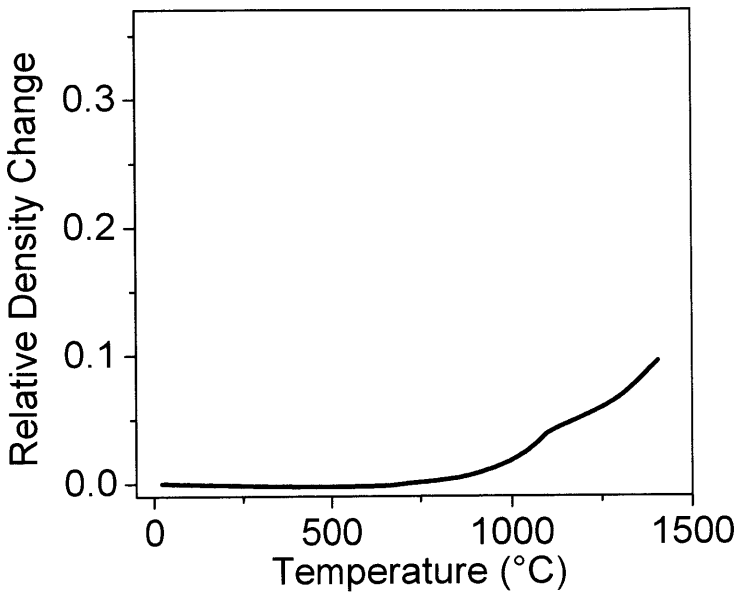

Figure 2.2 Relative density change of nanocrystalline W as a function of temperature.

As shown in Figure *2.2*, nanocrystalline W does not demonstrate any rapid densification and failed to achieve full density. The onset of sintering at low temperature and the rapid rate of densification are apparently required to produce bulk nanocrystalline tungsten by minimizing grain growth during a thermal cycle, and therefore the addition of an alloying element into tungsten is desirable to accelerate consolidation.

2.3 Nanocrystalline W-Cr alloys

2.3.1 Alloying element selection

Since this thesis is concerned with production of nanocrystalline W alloys after a sintering cycle, additives to the system should promote the retention of fine grains during the thermal exposure. We therefore are interested specifically in alloying elements that not only may

lowering the onset of densification, but which will have positive effects on maintaining grain size. Chookajorn et al. studied stability of nanocrystalline tungsten alloys and constructed a stability map for tungsten-based binary alloys with positive heats of mixing, shown in Figure *2.3* (*56*, *57*).

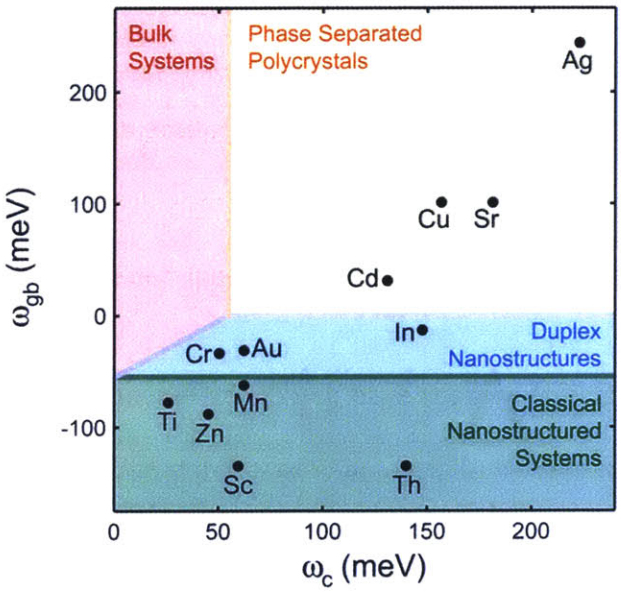

Figure 2.3 Stability map of tungsten-based alloys populated with alloy's material parameters (*57*).

Figure *2.3* represents three stability regions and binary solute additions to tungsten are classified into these regions. The elements which lie in regions of classical and duplex nanostructures (the green and blue region) were found to help stabilize a nanocrystalline state: Ti, Sc, Zn, Mn, Th, Cr, Au, and In.

In addition, they experimentally confirmed that titanium suppresses grain growth of tungsten; nanoscale grain structure of nanocrystalline W-20 at.% Ti was retained after annealing at 1100 °C for a week (*56*). This promising level of thermal stability suggests that W-Ti alloys may be suitable for consolidation, although the temperature tested by Chookajorn et al., 1100° C, still lies below the range where tungsten would sinter. Therefore, we heated nanocrystalline W-Ti

alloys to examine its sinterability. The relative density change of nanocrystalline W-20 at.% Ti prepared using the same procedure outlined in section 2.1 for 20 hours of milling was measured as a function of temperature as shown in Figure *2.4*. This titanium-tungsten alloy unfortunately shows almost no densification although it might retain the nanoscale grain size during the thermal cycle.

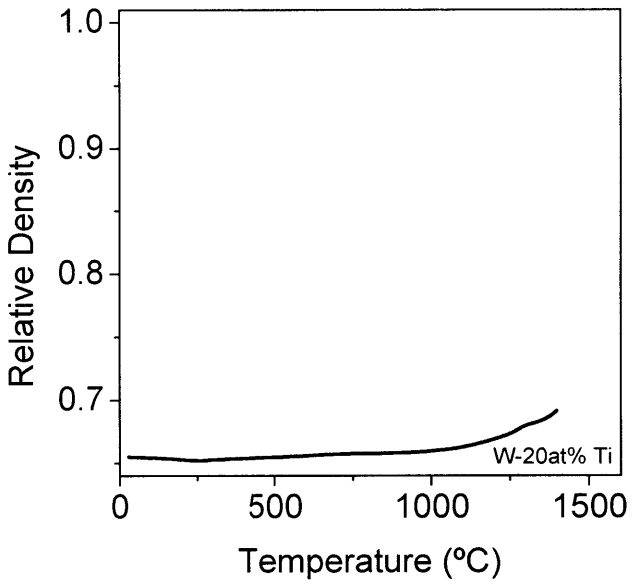

Figure 2.4 Relative density change of nanocrystalline W-20 at.% Ti as a function of temperature.

The above result confirms that while some elements may promote thermal stability of a nanoscale grain structure, there may still be a consolidation challenge for such powders. In the case of W-Ti, pressureless sintering may not be a viable route to full density compacts. It would therefore be very desirable to find an element that can not only promote nanostructure, but which can also accelerate sintering.

Among the several elements presented in Figure *2.3*, we chose to further explore chromium as an alloying element. The map shows that this alloy pair lies in a unique regime called the "nano-

duplex" regime, which suggests evolution of the nanostructure to a nanoscale two-phase structure; this in turn could affect long-range transport of matter across the structure as required for sintering. Furthermore, the W-Cr system has no intermetallic compounds at any temperature based on the equilibrium phase diagram of W-Cr alloy in Figure *2.5*. We assumed that an intermetallic compound having strict stoichiometry might be a kinetic obstacle to densification; the W-Cr system possesses only Cr and W rich phases up to a critical temperature.

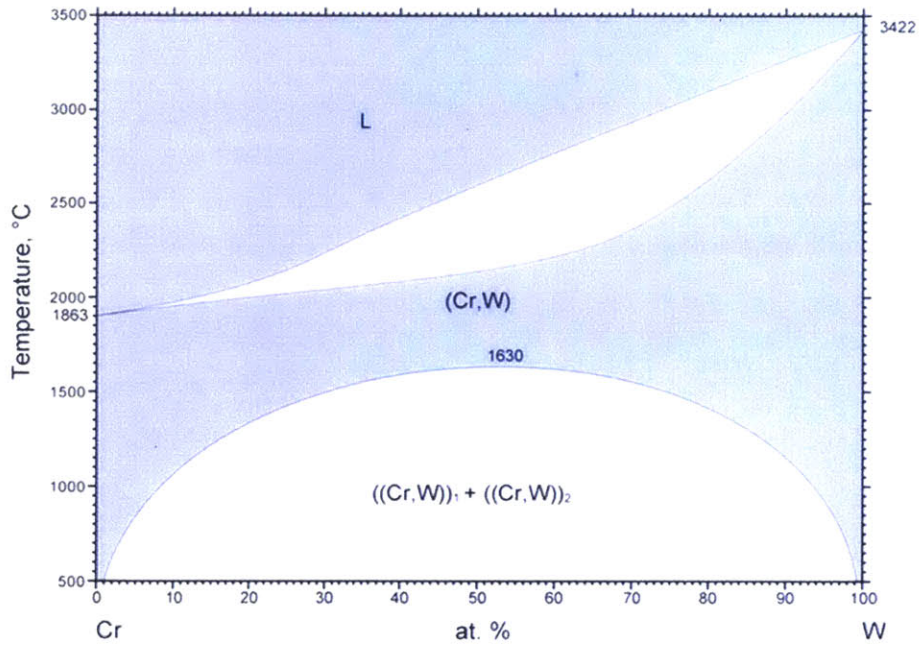

Figure 2.5 Equilibrium phase diagram of W-Cr alloy (*58*).

In the following section, we show how to determine a set of parameters for powder processing such as the addition level of Cr and ball-milling time.

2.3.2 Cr addition level and milling time

Cr addition level

W and Cr powder were mechanically milled for 20 hours using the same procedure outlined in section 2.1, and XRD patterns of as-milled W-Cr alloys were obtained with varying Cr contents as shown in Figure *2.6*, showing the broadening of tungsten peaks due to grain refinement. Another characteristic in XRD patterns with increasing the Cr content is that the tungsten peaks are shifted to the right. The shift of tungsten peaks suggests that Cr atoms are dissolved into W after ball-milling process (*59*).

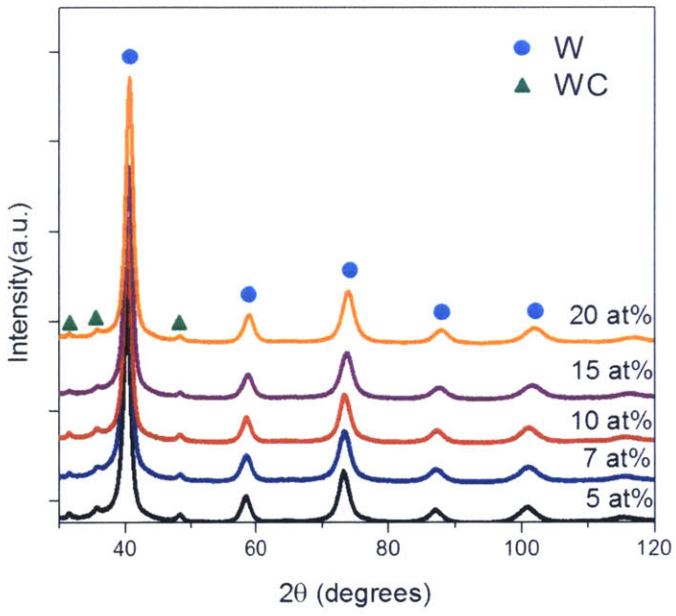

Figure 2.6 X-ray diffraction patterns of W-Cr systems with varying Cr content.

The as-milled grain size and change in the lattice parameter of W after 20 hours of ball-milling were measured by the Rietveld refinement method and represented with increasing Cr content in *Figure 2.7*. *Figure 2.7* shows that grain sizes reach nanoscale dimensions at all Cr contents after milling and they all have a similar grain size around 10 nm. The blue circle points in *Figure 2.7* represent the change in the lattice parameter of tungsten, showing an abrupt increase between 10 and 15 at.% Cr.

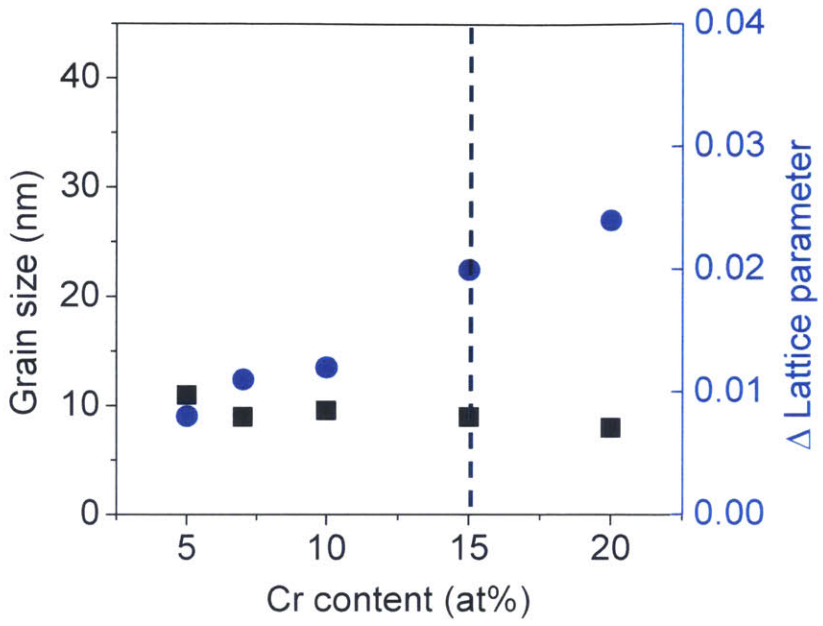

Figure 2.7 As-milled grain size and change in the lattice parameter of W-Cr systems after ball-milling.

The solubility of Cr in W seems to be beyond the saturation limit at 15 at.%. How much Cr dissolves into W is a very core concept in accelerating tungsten sintering kinetics which will be discussed later. We choose W-15 at.% Cr as a model composition for further in-depth study. We will return briefly to other compositions after understanding the mechanisms of sintering in this alloy system.

High-energy ball milling time

After setting the content of Cr at 15 at.%, we examined the effects of ball-milling time on tungsten alloy powders to determine proper one. XRD patterns of W-15 at.% Cr are shown in Figure *2.8*(a) as a function of milling time. With increasing milling time, the W peak (green point) is broadened and shifted to the right and the Cr peak (red point) is gradually disappearing. The as-milled grain size and change in the lattice parameter of W after ball-milling were

measured by the Rietveld refinement method and represented as a function of milling time in Figure *2.8*(b).

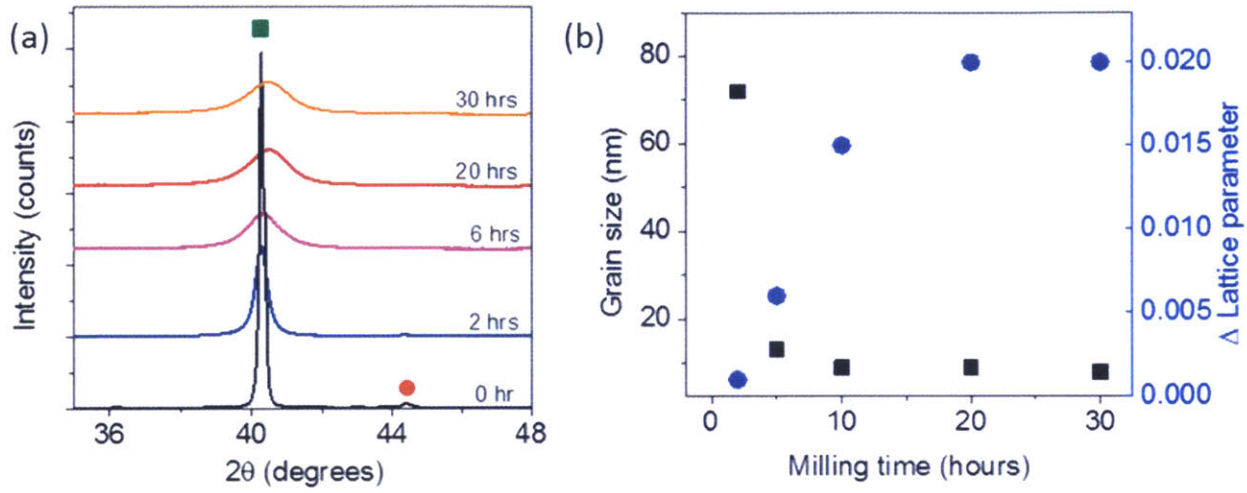

Figure 2.8 (a) X-ray diffraction patterns of W-15 at.% Cr with varying milling time. (b) As-milled grain size and change in the lattice parameter of W-15 at.% Cr as a function of milling time.

The grain size (black squares) shows an abrupt drop and reaches ~ 10 nm at 5 hours of milling. The lattice parameter change of tungsten is increasing as a function of milling time due to Cr dissolving into W. This lattice parameter change shows a plateau after 20 hours of milling, suggesting that the maximum solubility of Cr in W is achieved between 10 and 20 hours of milling. Therefore, we chose 20 hours of milling for powder processing in all of the subsequent experiments. The amount of tungsten carbide, picked-up from abrasion of the milling media, is around 1~2 weight percent after 20 hours of milling, as assessed by Rietveld refinement. Therefore, the following discussions will all focus upon tungsten alloy powders having a specific Cr content of 15 at.% processed for 20 hours of milling.

2.3.3 Particle and crystalline size

The SEM micrograph of as-milled W-15 at.% Cr after 20 hours of milling shown in Figure *2.9*(a) reveals that as-processed powder particles are micron-size in diameter.

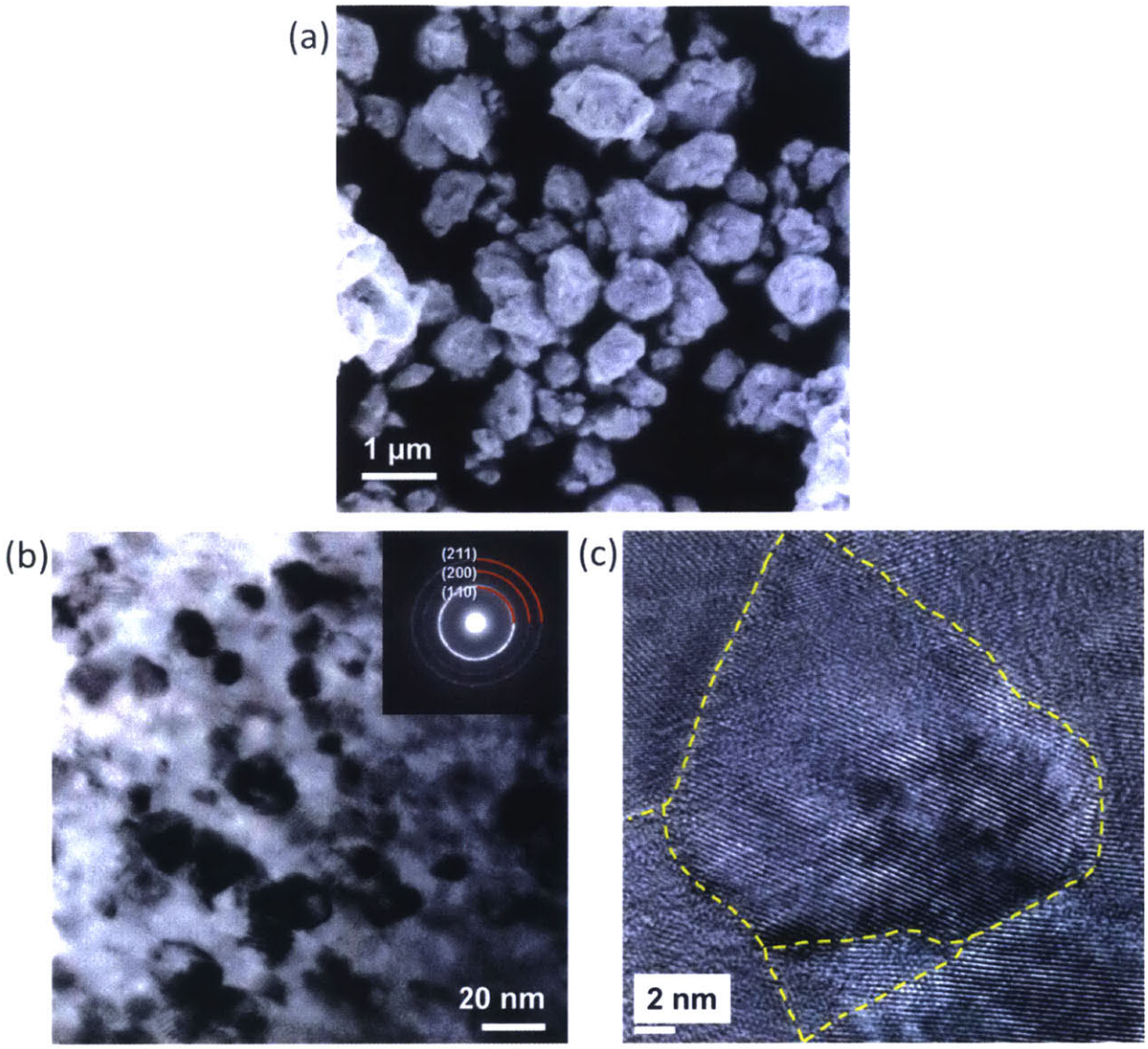

Figure 2.9 SEM and HR-SEM micrographs of nanocrystalline W-15 at.% Cr after 20 hours of milling showing (a) micron-scale particle size. (b) Bright-field TEM micrograph of nanocrystalline W-15 at.% Cr exhibiting nanoscale grains with the inset of selected area diffraction pattern and (c) HR-TEM micrograph showing a grain of nanoscale dimension.

Although the refinement of the grain size into nanoscale regime is successfully achieved through a high-energy ball mill, the particle size still remains at a micron-scale dimension. The reduction

in particle size during ball milling is highly limited because cold-welding increases particle size while fracturing simultaneously reduces it leading to a steady-state equilibrium particle size (*60, 61*). The average particle size after 20 hours of milling is 1.2 μm, which implies that the sintering driving force with regards to surface energy is unchanged by the milling process. This is an important point of differentiation from the sintering of nanopowders, which exhibit low sintering temperature caused by the excess surface energy due to the use of nano-sized particles.

TEM micrographs shown in Figure *2.9*(b) and (c) exhibit nanoscale W-alloy grains after 20 hours of milling as expected, and the average grain size estimated with TEM micrographs is revealed to be 12 nm which is very close to that assessed by the Rietveld refinement method (10 nm). The comparison in size distribution between particles measured by the laser diffraction particle size analyzer and grains is delineated in *Figure 2.10*. This comparison confirms that each milled powder particle is polycrystalline with nanoscale grains (*62, 63*), which is an important distinction as compared to, e.g., nanopowders, where every particle is of nanometer scale dimension and typically is a single crystal.

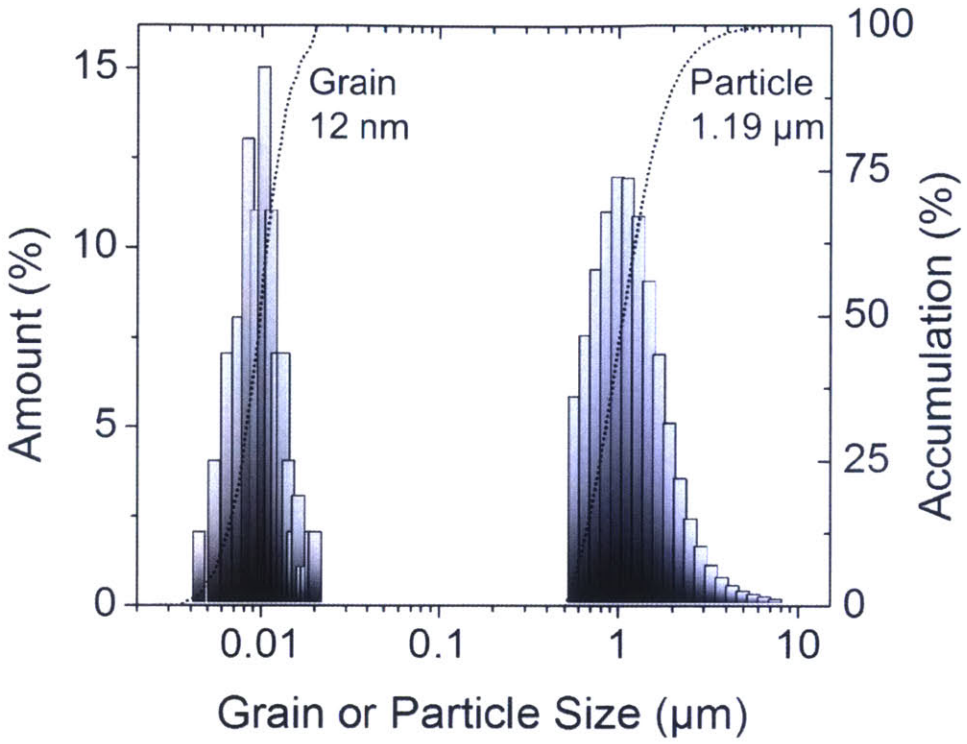

Figure 2.10 The distribution of particle and crystalline size of nanocrystalline W-15 at.% Cr after 20 hours of milling.

So far we physically characterized as-milled tungsten alloy powders and in the following section, we review chemical effects which a high-energy ball mill leads to.

2.3.4 Supersaturation

The selected-area diffraction pattern shown in the inset of Figure *2.9*(b) only exhibits diffraction rings from a tungsten bcc solid solution while chromium's is not visible, suggesting that Cr atoms are dissolved into W, in agreement with the XRD results presented earlier. This tungsten dissolution level does not align with the equilibrium phase diagram of W-Cr which expects a

negligible equilibrium solubility of chromium in tungsten at room temperature as shown in Figure *2.5* (*58*).

Atomic level mixing above an equilibrium solubility occurs during ball milling due to the severe plastic deformation and continuous shearing across interfaces (*60, 64*). This non-equilibrium process thus has been employed to synthesize supersaturated solid solutions in various immiscible alloy systems (*59, 65-68*). Such forced atomic mixing by mechanical attrition in immiscible alloy systems can sometimes be balanced by a demixing tendency to lower free energy, which would obey a diffusional kinetics. However, in the W-Cr system the diffusion distance at low temperature is extremely short due to low diffusion coefficients (*69*), which finally leads to a supersaturated tungsten solid solution at room temperature.

We confirm this supersaturated tungsten solid solution using XRD and STEM. As shown in the XRD pattern of Figure *2.8*(a), the intensity of chromium diffraction gradually decreases with increasing milling time and eventually disappears after 20 hours of milling. The dark field STEM micrograph of W-15 at.% Cr after 20 hours of ball-milling with EDS measurements of local composition shown in Figure *2.11* also demonstrates that the Cr atoms are homogeneously distributed over the entire tungsten particle without showing noticeable contrast variation at any specific spot.

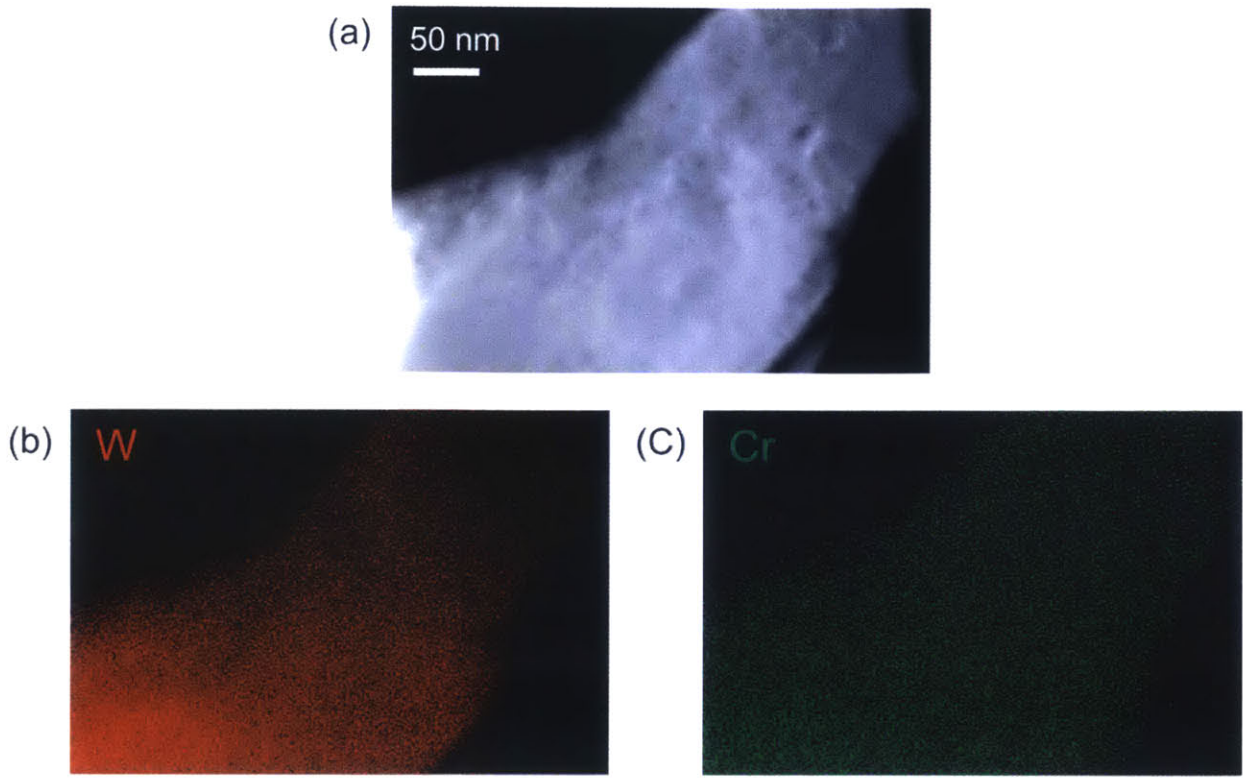

Figure 2.11 (a) Dark field STEM micrograph of nanocrystalline W-15 at.% Cr after 20 hours of ball-milling with energy dispersive spectroscopy (EDS) measurements of (b) W and (c) Cr composition.

All datasets including XRD, TEM, and STEM clearly imply that ball milling of W-15 at.% Cr for 20 hours generates a supersaturated tungsten solid solution.

2.3.5 Thermal stability[1]

The as-milled structure of W-15 at.% Cr is a non-equilibrium uniform solid solution and it is therefore expected to evolve upon heating where phase separation should occur (*57*). In case of the W-Cr system, which has a simple miscibility gap, phase separation could theoretically occur via either one of two ways: spinodal decomposition or nucleation and growth. The mechanism of

[1] The contents of this section have been published previously in reference (*57*).

phase separation in as-milled W-15 at.% Cr would be nucleation and growth instead of spinodal decomposition for two reasons. First, the composition of 15 at.% Cr is outside of the chemical spinodal region as shown in Figure *2.12*. Second, spinodal decomposition requires the certain amount of supercooling from a critical temperature to overcome the strain energy and the W-Cr system needs a supercooling on the order of 1650 °C (*70, 71*). Therefore, a supersaturated W-15 at.% Cr solid solution is expected to decompose at high temperatures by nucleation and growth.

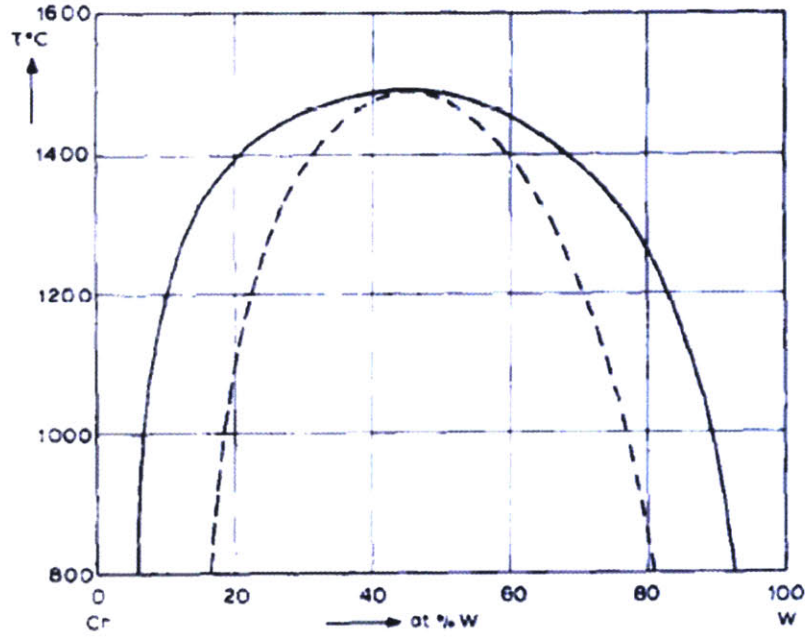

Figure 2.12 Miscibility gap in the W-Cr system (solid line) with the calculated chemical spinodal (dashed line) (*71*).

The as-milled W-15 at.% Cr powder was compacted and annealed to high temperatures at a constant heating rate of 15 °C/min in a reducing atmosphere of argon with 3% H_2 and cooled down rapidly under flowing argon with 3% H_2 after the target temperature was reached. We find that in W-15 at.% Cr, nano-sized Cr precipitates start to emerge near 950°C, mostly next to grain

boundaries and triple junctions, as delineated with green lines in the bright-field TEM image of Figure *2.13*(a).

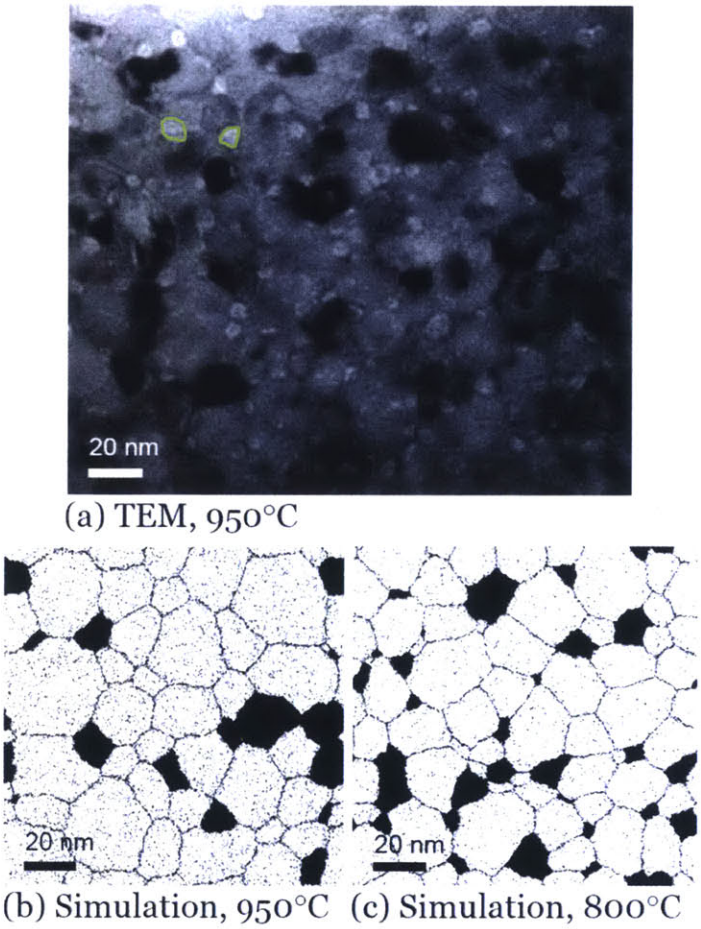

Figure 2.13 A W-15 at.% Cr alloy after heating to 950°C and cooling. (a) A bright-field TEM image shows the emergence of nanoscale Cr precipitates mostly next to grain boundaries and triple junctions after annealing up to 950°C; a few such Cr domains are encircled for clarity. For comparison, MC simulation results of the same system at (b) 950°C and (c) 800°C are shown (Simulation results are courtesy of Dr. Chookajorn).

The preferential formation of the Cr-rich phase at grain boundaries and triple junctions confirms that the decomposition occurs via a nucleation and growth mechanism as expected; spinodal decomposition leads to homogeneous precipitation rather than concentration at points of facile nucleation (*70*).

Heat dissipated during nucleation can be calculated using the enthalpy of mixing: $H_{mix} \times X \times (1 - X)$ where H_{mix} is the enthalpy of mixing and X is the alloy composition. When supersaturated W-15 at.% Cr is decomposed into the W-rich and the Cr-rich phase at 950 °C, generated heat is 2.436 kJ/mole. This estimated heat is the very upper bound because nucleation does not occur all at once based on the low diffusivity of Cr in W (*77*). Temperature increase occurred by the dissipated heat is ~98 °C calculated using the specific heat of tungsten. Such a small amount of released heat, which would evolve gradually during decomposition and therefore would not cause a significant temperature rise for a very long time, is unlikely to be a significant effect on the overall sintering kinetics of the system.

Monte Carlo (MC) simulations for nanostructured W-Cr alloys were conducted to simulate an equilibrium microstructure (by Chookajorn). Figure *2.14* shows a series of simulations of the W-Cr systems with nanoscale grain boundaries available. The structures are shown at temperatures from 900 to 1500°C, which capture the crossing of the solvus (the cooling procedure was described in (*57*)). The size of Cr-rich precipitates here is highly refined to the nanoscale. At a certain solute composition, the structure evolves from being both grain boundary-segregated and phase-separated at lower temperature to displaying solute-segregated grain boundaries at high temperature.

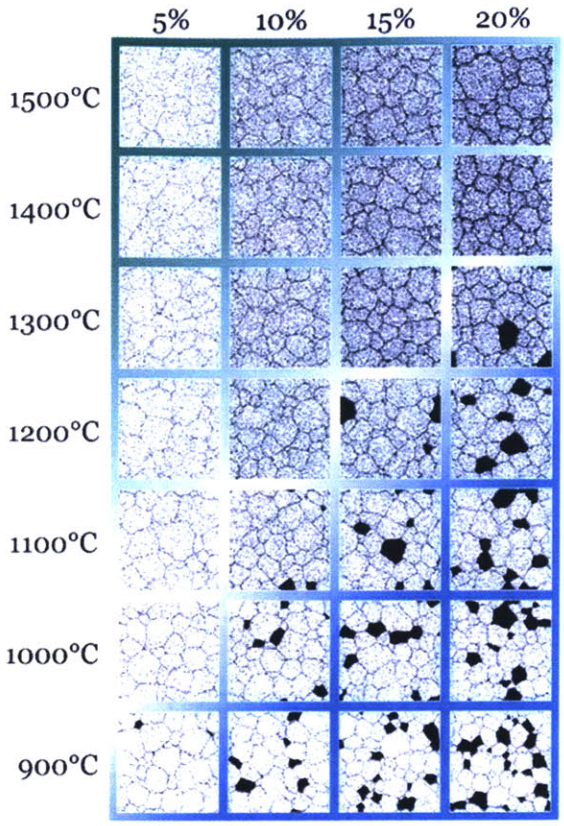

Figure 2.14 Changes in equilibrium structure with Cr composition and temperature in nanostructured W-Cr alloys, as predicted by the Monte Carlo model (*57*).

The microstructure experimentally observed in Figure *2.13*(a) is consistent with the MC results of Figure *2.13*(b) at the same temperature, comparing qualitatively favorably in terms of characteristic scales and prevalence of the second phase Cr particles, but with somewhat higher volume fraction and smaller Cr particles than the simulation. This is most likely due to the short heating cycle we used experimentally (a constant heating rate followed by gas-cooling), which may not fully evolve the structure to an equilibrated state. Indeed, comparing with simulations at a slightly lower temperature of 800 °C, which might be more reflective of the average time-at-temperature conditions experienced by the experimental sample, shows an improved agreement. The volume fraction of Cr-rich phase assessed from Figure *2.13*(a) is around 17%, which matches that of MC result at 800 °C in Figure *2.13*(c) at 17%. The average size of Cr-rich grains

in Figure *2.13*(a) at ~8 nm is also close to that from the 800 °C MC structure in Figure *2.13*(c) at ~9 nm.

Chapter 3 Nano-Phase Separation Sintering

The previous chapter established the procedures for synthesizing nanocrystalline alloy powder, and led to a downselection onto the W-15 at.% Cr alloy system for more detailed study. It also established that the system is capable of retaining a nanoscale structure through a significant thermal exposure, and yet undergoes a decomposition by nucleation and growth to a two-phase "nano-duplex" structure in which Cr domains decorate the grain boundaries and triple junctions of W grains within each powder particle.

With this background, we now proceed to explore the sintering in this system, with an eye towards understanding the sintering mechanisms.

3.1 Density and structure changes upon heating

i) The change in density upon heating

W-15 at.% Cr powder was ball-milled using the same procedure outlined in section 2.1 and was then compacted by cold press into 6 mm diameter and 3~4 mm high cylindrical disks of 0.63 relative density. Cold-pressed compacts of as-milled W-15 at.% Cr powder were heated without applied pressure at a constant heating rate (10 °C/min) under Ar+3% H_2 and cooled down rapidly under Ar+3% H_2 after the target temperature was reached. The change in compact density as a function of time and temperature was measured with the TMA. As shown in *Figure 3.1*, sintering is found to initiate at ~950 °C. Such sintering temperatures are significantly lower than typical W sintering temperatures, which can reach 3000 °C for micron-size powders (*72*); recall in Figure *2.2* and Figure *2.4* that the W used in this study does not sinter appreciably for the same thermal excursion, and a grain-size-stabilizing addition of Ti does not change this. The sintering of W-15 at.% Cr at these temperatures is thus noteworthy.

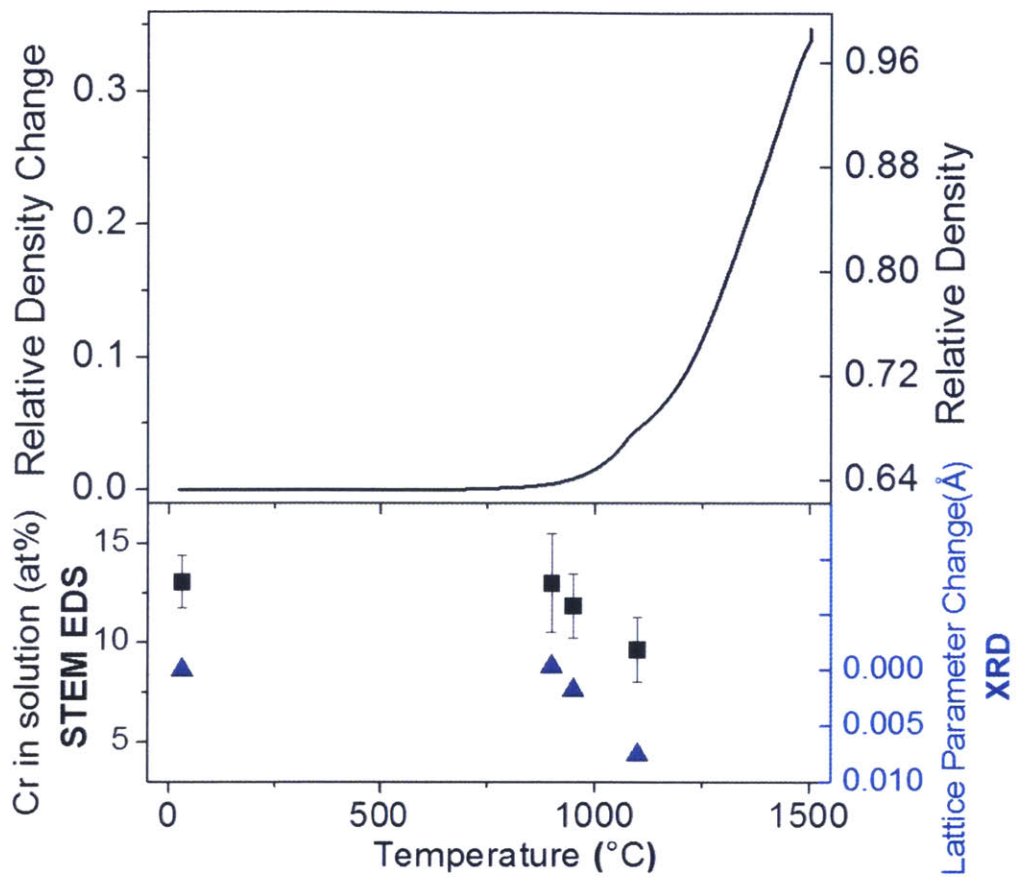

Figure 3.1 The change in relative density, Cr content in W solution, and lattice parameter of supersaturated W with increasing temperature.

Figure 3.1 illustrates that nearly full density is achieved without any external pressure after 155 minutes of annealing (final density > 98%).

ii) The change in microstructure upon heating

As shown in the SEM micrograph in back-scattered mode in *Figure 3.2*(a), a chromium-rich phase precipitates from the supersaturated solution upon heating. The chromium is found covering tungsten particle surfaces in small domains and forming necks between the tungsten

powder particles. These Cr-rich domains are delineated by the yellow, dashed lines in *Figure 3.2*(a).

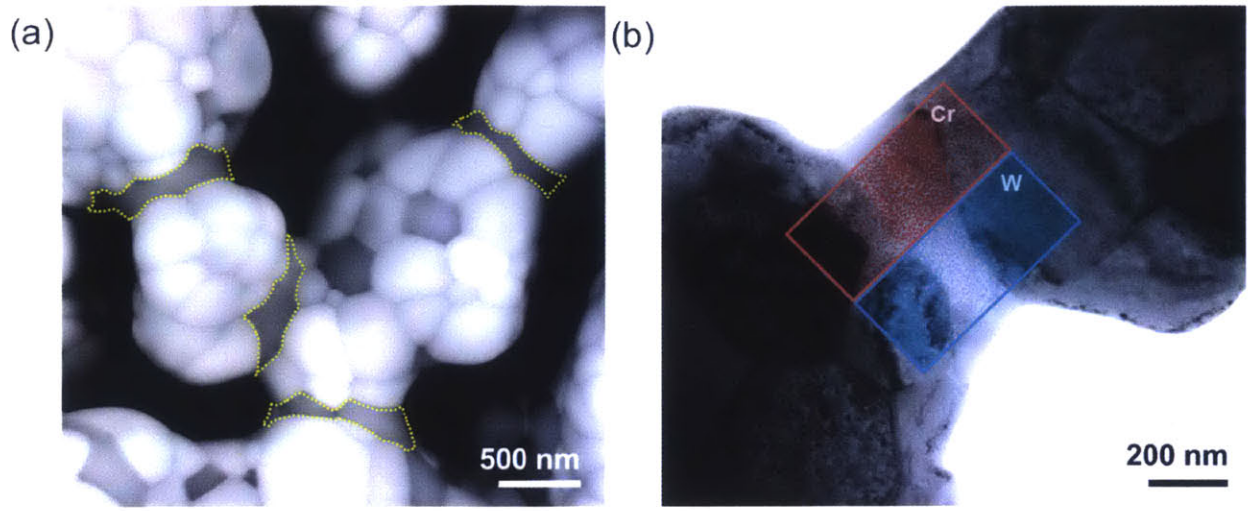

Figure 3.2 Postsintering microstructures of W-15 at.% Cr alloy. (a) SEM in back-scatter mode reveals a chromium-rich phase forming necks between the compact particles upon heating up to 1300 °C. (b) A direct visualization of a Cr-rich neck adjacent to W-rich particles is shown in the bright-field TEM image with W and Cr elemental map (superimposed on the micrograph) using STEM-EDS.

The Cr-rich nature of the neck between the two particles is confirmed in *Figure 3.2*(b) through STEM-EDS measurements of local tungsten and chromium composition, explicitly showing that the powder particles are rich in W and the neck is rich in Cr. The interparticle contact point where the necks form is a thermodynamically favored site for phase separation and growth; phase separation and growth at such sites is also observed in other alloy systems (*73, 74*). By assuming the classical sintering model of two spherical particles in contact with each other, excess vacancies ($\Delta C = C_0 \frac{V_0 \gamma}{RTr}$, C_0: vacancy concentration on flat surface, V_0: the molar volume, γ: the surface energy, r: the radius of neck curvature, R: gas constant, T: temperature) exist over the equilibrium concentration beneath the concave surfaces of the particle contact point. These geometrically-induced excess vacancies cause chromium atoms to diffuse more rapidly in the

area surrounding the contact point. This accelerated diffusion makes these sites favorable for nucleation of the second phase. In addition to geometric effects, diffusional flow of chromium caused by a gradient in vacancy concentration occurs more rapidly than tungsten due to its higher diffusion coefficient (*69*), which results in interparticle necks enriched with chromium. This accounts for the fact that the Cr-rich phases delineated in *Figure 3.2*(a) and (b) preferentially decorate interparticle necks and the surfaces.

We also examined the microstructure of W-15 at.% Cr at nearly full density after sintering, as shown in Figure *3.3*. We have circled in red those regions that are likely the original powder particles, and which are now W rich, having ejected Cr from solution. Such particles tend to be decorated around their perimeter with Cr-rich domains. The structure here is consistent with those at lower densities presented in Figure *3.2*.

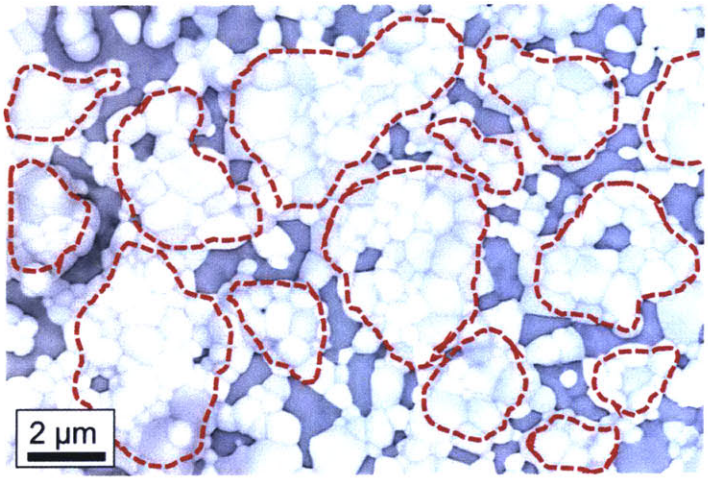

Figure 3.3 SEM micrograph in back scattering mode of W-15 at% Cr with near-full density after sintering.

3.2 Sintering mechanism and kinetics

i) Sintering mechanism

In order to examine the abnormal, low-temperature sintering mechanism, a detailed chemical and microstructural analysis was performed. More specifically, the Cr content in the supersaturated W solution was measured by STEM-EDS and lattice parameter of supersaturated W estimated by the Rietveld refinement method were observed through a sintering cycle as shown in *Figure 3.1*. The microstructures of nanocrystalline W-15 at.% Cr upon heating were examined by dark-field STEM, with typical results presented in *Figure 3.4*.

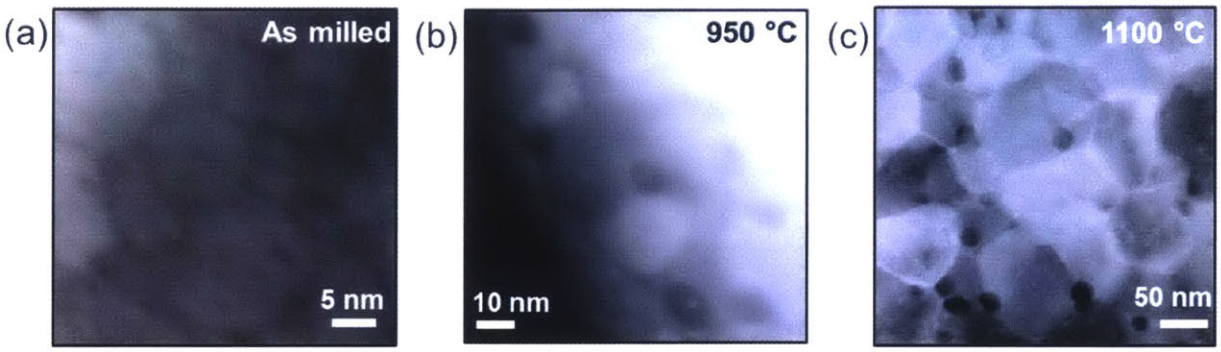

Figure 3.4 Dark-field STEM micrographs of nanocrystalline W-15 at.% Cr (a) before annealing, (b) at 950 °C, and (c) at 1100 °C.

The Cr content in the tungsten solution as function of temperature denoted as the black points in *Figure 3.1* is found to drop simultaneously with the emergence of phase separation. The Cr-rich phases, which are seen as darker phases in dark field STEM micrographs, begin to precipitate at grain boundaries and triple junctions at the same temperatures at which chemistry begins to evolve (*Figure 3.4*(b)). The lattice parameter of the tungsten solid solution as a function of heating temperature (the blue points in *Figure 3.1*), begins changing at the same temperature as the initial observation of phase separation. All of these data verify that phase separation is triggered around 950 °C, which is the same temperature as the onset of densification.

We attribute the onset of sintering at low temperature and the rapid rate of densification in the W-Cr system to the nanoscale phase separation generating fast diffusion pathways for tungsten

atoms. Once the Cr-rich phase has been ejected out of the supersaturated tungsten and formed an interparticle neck, the solubility of W in the neck increases as temperature increases (*58*), suggesting that it is capable of dissolving W atoms and providing a transport pathway. The STEM-EDS measurement of local tungsten and chromium composition (*Figure 3.2*(b)) visibly shows a large amount of tungsten dissolved in the Cr-rich neck. Therefore, we posit that densification occurs by the W atoms i) dissolving from the particle into the neck, ii) diffusing through the Cr-rich phase in the neck to the lower free energy sites at the neck edge, and iii) filling and annihilating the pore between particles, which is illustrated through a schematic structure in Figure *3.5*.

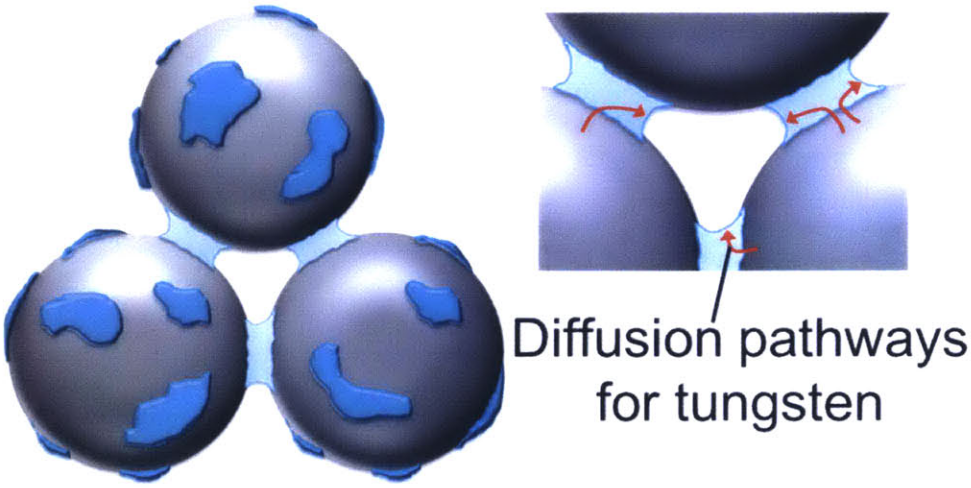

Figure 3.5 A schematic for densification during nano-phase separation sintering, illustrating that chromium-rich phase provides a short-circuit diffusion pathway for tungsten atoms, which controls the kinetics of sintering.

ii) Sintering kinetics

We identify the characteristic atomic processes which form the rate-limiting step during sintering by determining the sintering activation energy, and corroborate the proposed sintering

mechanism. To determine the sintering activation energy, the master sintering curve method (*75, 76*) was employed. The atomic flux contributing to filling the pores is related to instantaneous shrinkage rate of a compact.

$$-\frac{dL}{L\,dt} = \frac{\gamma\Omega}{k\mathrm{T}} \times \left(\frac{D_v\Gamma_v}{G^3} + \frac{\delta D_b\Gamma_b}{G^4}\right) \quad (1)$$

where γ is the surface energy, Ω is the atomic volume, k is the Boltzmann constant, T is the temperature, G is the average particle or grain size, ρ is the relative density, t is time, δ is the grain boundary thickness, D_v and D_b are the coefficients for volume and grain boundary diffusion, Γ is a parameter which relates the driving force, mean diffusion distance, and other geometric features of the microstructures. Assuming isotropic shrinkage, Eq. (1) can be related to the integral form of the instantaneous densification rate as follows:

$$\int_{\rho_0}^{\rho} \frac{(G(\rho))^n}{3\rho\Gamma(\rho)}\,d\rho = \int_0^t \frac{\gamma\Omega D_0}{kT}\exp\left(-\frac{Q}{RT}\right)dt \quad (2)$$

where Q is the sintering activation energy, R is the gas constant, ρ is the relative density, $D_0 = (D_v)_0$ and n = 3 for volume diffusion, and $D_0 = (\delta D_b)_0$ and n = 4 for grain-boundary diffusion. Eq. (2) can be rearranged into an equivalence of two terms: one including all microstructural and materials properties (Eq. (3)) and the other which depends only on Q and the heating time-temperature profile, $T(t)$ (Eq. (4)).

$$\Phi(\rho) \equiv \frac{k}{\gamma\Omega D_0}\int_{\rho_0}^{\rho} \frac{(G(\rho))^n}{3\rho\Gamma(\rho)}\,d\rho \quad (3)$$

$$\Theta(t, T(t)) \equiv \int_0^t \frac{1}{T}\exp\left(-\frac{Q}{RT}\right)dt \quad (4)$$

If a single sintering activation energy exists, then is the correct value of Q will collapse all the heating profiles of Eq. (4) onto a single curve. To assess the sintering activation energy in the W-

Cr system, several density-temperature profiles were acquired at heating rates of 5, 10, 15, and 20 °C/min. The raw density-temperature profiles are represented in Figure *3.6*. We perform the normalization process according to Eq. (4) in the next section.

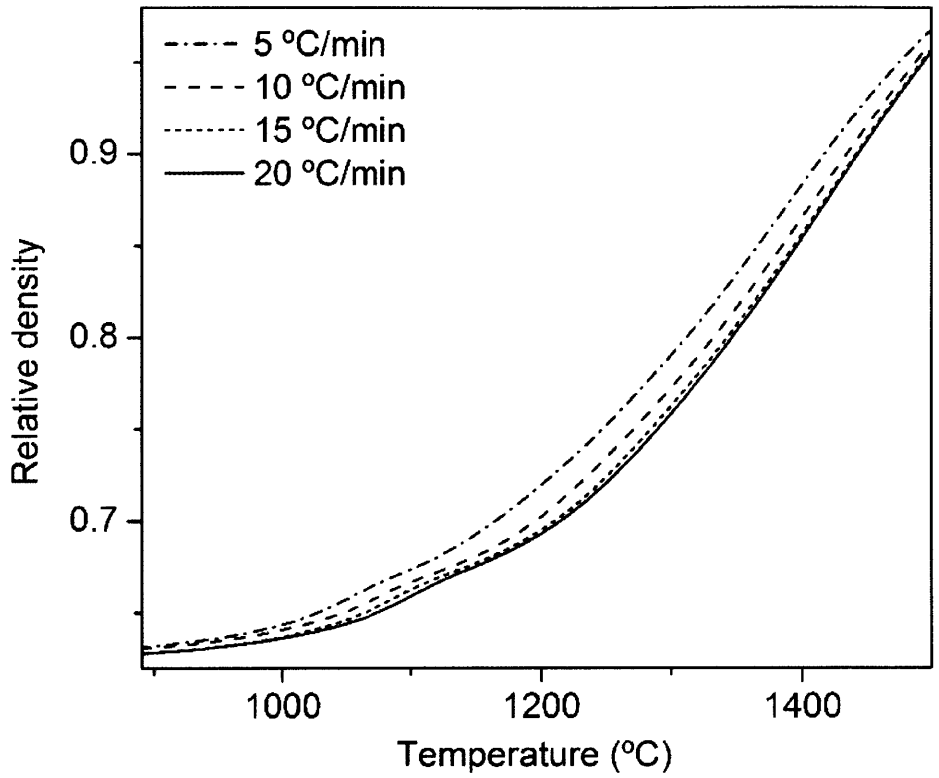

Figure 3.6 Heating profiles of nanocrystalline W-15 at.% Cr as function of temperature with 5, 10, 15, 20 °C/min heating rates.

Figure 3.7(a) exhibits the mean residual squares of the fitting process as a function of Q. *Figure 3.7*(b) illustrates normalized heating profiles at three different sintering activation energies denoted in *Figure 3.7*(a), showing dispersion between normalized profiles when the correct activation energy is not chosen. The best convergence of heating profiles to a single curve occurs for a sintering activation energy of 373 kJ/mol.

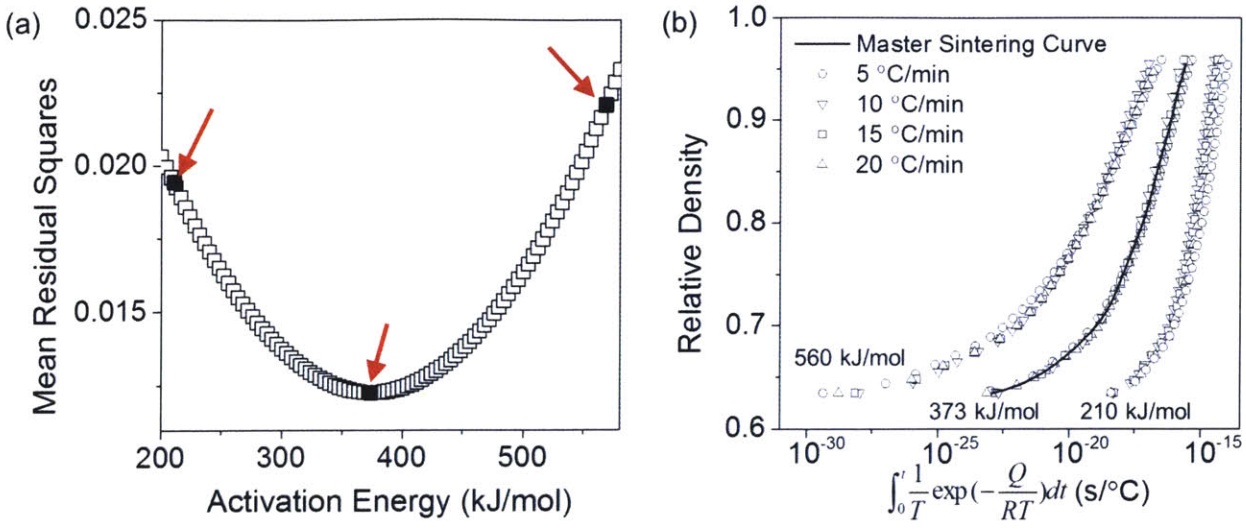

Figure 3.7 (a) The mean residual squares as function of sintering activation energy, (b) normalized heating profiles at three different activation energies denoted in (a).

This activation energy is very close to that for tungsten diffusion in chromium, 386 ± 33 kJ/mol (*77*), which is much lower than that for W self-diffusion, 550~670 kJ/mol (*78*) and even farther from that for Cr diffusion in W which is 547 kJ/mol (*79*). This kinetics is in line with the mechanism proposed that precipitated Cr-rich phases provide fast diffusion paths to tungsten which is the base element controlling sintering. Therefore, the nanocrystalline W with the addition Cr exhibits the rapid sintering rate at anomalously low temperature unlike pure tungsten sintering itself, which possesses a much higher sintering activation energy.

iii) Driving force for sintering

The driving force for sintering in the case of nano-phase separation sintering can be estimated using prior models, e.g., that for liquid phase sintering. A model geometry is shown in Figure *3.8*, and corresponds to the one shown in Figure *3.2* or Figure *3.5*. Although the model for liquid

phase sintering is employed here, the phase between two particles in the model of Figure *3.8* is a crystalline Cr phase instead of the liquid one that is a rapid diffusion pathway for tungsten.

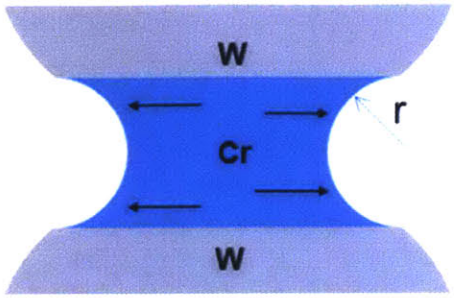

Figure 3.8 A model geometry for an interparticle neck during nano-phase separation sintering. The blue region is the crystalline Cr phase and the W particles are grey.

The driving forces for any mass-transport controlled process are gradients in chemical potentials of the species involved in the transport. For sintering in the geometry represented in Figure *3.8*, the relevant gradient is $\nabla(\mu_w - \mu_v)$ where μ_w, μ_v are the chemical potentials of a W atom and of a vacancy, respectively. The capillary pressure at the neck provides the gradient. Therefore the driving force for sintering is finally estimated as $-\frac{\alpha\Omega_w\gamma_{cr}}{r}$ where α is a constant, Ω_w is the atomic volume of W, γ_{cr} is the surface energy of Cr, and r is the radius of pore as delineated in Figure *3.8*. If the dominant mass transport process leading to densification is assumed to be W diffusion through Cr, the W aomic flux can be converted to a densification rate using the microstructural geometry following the formulation of DeHoff: $-\frac{dL}{Ldt} = \frac{\gamma\Omega_w}{kT}\left(\frac{\Gamma_b\delta D_b}{G^4}\right)$ where L is the length of the compact, γ is the surface energy, G is the average particle size, t is time, δ is the thickness of the Cr-rich layer, D_b are the coefficients for W diffusion in Cr, and Γ is a parameter which relates the driving force, mean diffusion distance, and other geometric features of the microstructures (*76*). Introducing reasonable values for each parameter at the onset of sintering into the right-hand side of this equation ($\gamma \sim 2.3$ J/m^2 (*80*), $\Gamma_b \sim 10^4 - 10^5$ (*76*), $D_b \sim 10^{-19} - 10^{-18}\ m^2/sec$

(*77*), G $\sim 10^{-6}\ m$, $\delta \sim 120$ nm) results in 2.5×10^{-7}/sec ~2.5×10^{-6}/sec which has the same order of magnitude as the initial shrinkage rate ($-\frac{dL}{L\,dt}$) of nanocrystalline W-15 at.% Cr that we experimentally measured, ~ 10^{-6}/sec at the onset of sintering. This confirms that tungsten diffusion through the Cr-rich phase at such a low temperature is sufficient to lead to the observed change in the length of the compact.

3.3 Conditions for nano-phase separation sintering

The acceleration in densification via nano-phase separation sintering is achieved only when it is prepared as a (i) 'supersaturated' and (ii) 'nanocrystalline' powder. To confirm that both of these two conditions were necessary for accelerated sintering in the W-Cr system, a series of control experiments were designed to produce powders which possessed one of these conditions at a time, while not possessing the other. In effect, the experiments were conducted to vary supersaturation, grain size and alloy compositions independently of one another. The results are shown in *Figure 3.9*, all of which utilized micron-size powders to remove particle size effects (Information of the particle size of each control experiment is in Appendix A).

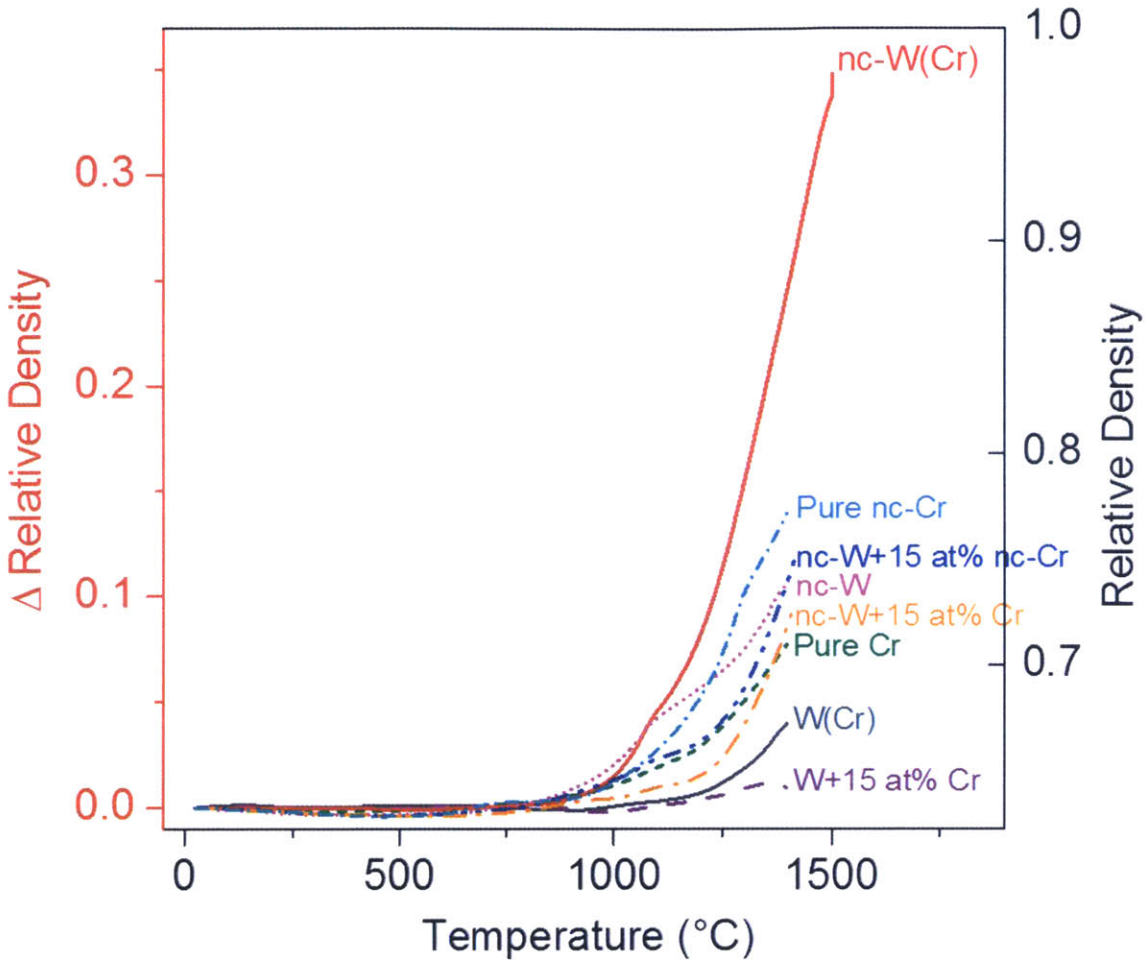

Figure 3.9 Changes in density of milled W-15 at.% Cr and a series of control experiments upon heating.

We first prepared a simple mixture of W-15 at.% Cr in the absence of both nanoscale grains and supersaturation. 15 at% Cr was dry-mixed with W for approximately 15 minutes without mechanical alloying or milling. The resulting sample was a mixture of W-15at.% Cr, but had no nanoscale grain structure nor supersaturation; it met neither condition (i) nor (ii). This powder was then compacted into 6 mm diameter and 3~4 mm high cylindrical disks of 0.67 relative density and annealed (purple). This control showed almost no densification, implying that the rapid rate densification is not accompanied without both alloy supersaturation and nanocrytallinity within a particle. In addition, this result also

implies that the enhanced sintering kinetics does not arise from the simple chemical effect of chromium.

The next controls are pure nanocrystalline tungsten and nanocrystalline tungsten with an addition of 15 at.% microcrystalline chromium and 15 at.% nanocrystalline chromium. In case of pure nanocrystalline tungsten, pure tungsten was mechanically milled using the same procedure outlined in section 2.1. The resulting sample had a grain size of 10 nm as revealed by the Rietveld refinement method, but no Cr, and thus met condition (ii) but not (i). This powder was then compacted into 6 mm diameter and 3~4 mm high cylindrical disks of 0.62 relative density. In the case of pure nanocrystalline tungsten with the addition of microcrystalline chromium, powder of 15 at.% Cr was added to pure nanocrystalline W with a dry mixing method for approximately 15 minutes without milling or mechanical alloying. The resulting sample comprised W with a grain size of 10 nm as revealed by the Rietveld refinement method, and contained chromium, but not in an alloyed or supersaturated condition; it met condition (ii) but not (i). This powder was then compacted into 6 mm diameter and 3~4 mm high cylindrical disks of 0.63 relative density. In case of pure nanocrystalline tungsten with the addition of nanocrystalline chromium, powder of 15 at.% nanocrystalline Cr, produced using the same procedure outlined in section 2.1, was added to pure nanocrystalline W with a dry mixing method. The resulting sample comprised W particles with a grain size of 10 nm and Cr particles with a grain size of 17 nm as revealed by the Rietveld refinement method, but not in an alloyed or supersaturated condition; it met condition (i) but not (ii). This powder was then compacted into 6 mm diameter and 3~4 mm high cylindrical disks of 0.65 relative density.

These pure nanocrystalline tungsten (magenta) and nanocrystalline tungsten with the

addition of microcrystalline chromium (dark blue) and nanocrystalline chromium (yellow) were annealed. As shown in *Figure 3.9*, they do not demonstrate any rapid densification, suggesting that nanocrystallinity alone is not sufficient to achieve the observed rapid sintering.

The last control is supersaturated W-15 at.% Cr with micron-scale grain produced by the following procedure. W-15 at% Cr powders were mechanically milled in a SPEX 8000 high-energy mill for 30 minutes using tungsten carbide media without any process control agent. The resultant powder was then sealed in a quartz tube, first evacuated to 10^{-6} Torr using a turbo pump, and then backfilled with high-purity argon gas to 120 Torr. The sealed ampoule was annealed in a furnace at 1400 °C for 20 hours and then quenched. The resulting powder was a supersaturated W(Cr) solution, but with a coarse grain size in excess of one micron; it met condition (i) but not (ii). This tungsten solid solution powder was then compacted into 6 mm diameter and 2~3 mm high cylindrical disks of 0.65 relative density and annealed (dark gray). This compact does not display any acceleration on its density change due to the fact that chromium diffusion coefficient in tungsten is extremely low, e.g. $\sim 10^{-27}$ m^2/s at 1000 °C (*79*), which does not enable Cr-rich precipitates to form at low temperature. This result clearly demonstrates that a supersaturated solid solution alone is not enough to accomplish nano-phase separation sintering.

When the two features, alloy supersaturation and nanocrystallinity, are simultaneously combined, the compact finally densifies with a rapid rate and a low onset temperature for sintering at ~950 °C (red curve). For the comparison with sintering of chromium, the compacts of pure Cr and pure nanocrysatalline Cr were prepared. APS<10 μm pure

chromium powder Cr powder purchased from Alfa Aesar was compacted into 6 mm diameter and 3~4 mm high cylindrical disks of 0.67 relative density and annealed (green). Nanocrystalline Cr was mechanically milled using the same procedure outlined in section 2.1. The resulting sample had a grain size of 17 nm as revealed by the Rietveld refinement method; it was nanocrystalline but contained no alloying additions, and thus met condition (ii) but not (i). It also contained no tungsten, and provides a limiting case if the kinetics of densification were dominated by the low melting point of Cr in W-Cr systems. This powder was compacted into 6 mm diameter and 3~4 mm high cylindrical disks of 0.66 relative density and annealed (cyan). As shown in *Figure 3.9*, the sintering onset temperature of nanocrystalline W-15 at.% Cr (red) is even lower than both the onset for pure chromium sintering and for pure nanocrystalilne chromium sintering.

The low onset of sintering and rapid rate of densification in nanocrystalline W-15 at.% Cr apparently result for two reasons. First, nanoscale grain size along with a number of crystal defects generated during ball milling can facilitate short-circuit diffusion pathways and heterogeneous nucleation of the Cr-rich phase, which thus permits second phase nucleation in a much shorter time and with a higher number density of nuclei. Second, crystal defects homogeneously distributed over a whole powder volume provide possible nucleation sites which increases the possibility of generating fast diffusion pathways through every powder particle by allowing a second phase to preferentially and uniformly decorate particles and to form interparticle necks. This was confirmed by closer examination of supersaturated W-15 at.% Cr with micron-scale grains (dark gray). In the micron grain size sample, nucleation of second phases takes a much longer time, and the locations of the precipitates are highly

random. As the precipitates are not properly located on necks, this does not create fast diffusion paths through which powder particles can exchange mass.

3.4 Comparison to conventional enhanced sintering

There are many other, well-studied methods for enhancing the sintering kinetics of high temperature materials such as tungsten. The two main methods for accelerating tungsten sintering are activated sintering and liquid-phase sintering. It is instructive to compare nano-phase separation sintering to these two conventional methods. In addition, we will also compare nano-phase separation sintering with seed assisted sintering which is a well-known method for the production of ceramic materials.

3.4.1 Sintering mechanism

i) Seed assisted sintering

Both seed assisted sintering and nano-phase separation sintering involve the precipitation of a second phase during sintering. However, mechanistically they are quite different, because the function of the second phase in accelerating sintering is very different. Nano-phase separation sintering employs nucleated phases as a fast transport layer that preferentially decorates interparticle necks, and which thereby directly increases the diffusivity of the base element and thus the densification rate. In contrast, seed assisted sintering uses nucleated phases in a structural way; a high number of density of nucleated "seeds" prohibit the formation of a micrometer scale phase, which significantly discourages sintering at low temperature.

In addition, since nano-phase separation and seed assisted sintering use the second phase in a different way, the conditions for selecting it are also different. For example, ceramic oxide seed particles should be isostructural with the final phase for effective heterogeneous nucleation in the case of seed assisted sintering (*81, 82*). However, a low melting point element that need not be isostructural is required in the case of nano-phase separation sintering in order to obtain increased diffusivity of a base element during sintering.

Finally, the different usages of the second element between these two mechanisms naturally induces dissimilar microstructures; the second element is preferentially located on particle surfaces and interparticle neck regions in the case of nano-phase separation sintering as shown in Figure *3.2*, but is uniformly distributed in the bulk in the case of seed assisted sintering. In the following sections, we review the mechanisms of solid state and liquid phase sintering, and provide further evidence that nano-phase separation sintering operates with a distinct mechanism.

ii) Solid-state activated sintering

According to a recent theory of solid-state activated sintering (*20, 83*), a nanometer thick disordered layer provides a fast transport layer to tungsten atoms, which accelerates sintering kinetics as discussed in section 1.2. The stabilization of a nanometer thick disordered layer could be possible between powder particles even below the bulk melting temperature as shown in Figure *1.2* if the free energy penalty for forming the undercooled liquid film is over-compensated by the reduction in the interfacial energies represented (for details, see section 1.2).

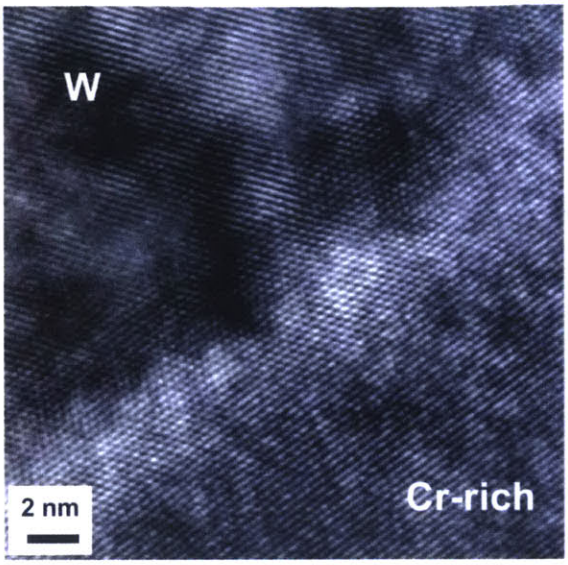

Figure 3.10 The crystalline phase between tungsten and chromium-rich layer at 1300 °C produced by nano-phase separation sintering.

However, as shown in *Figure 3.10*, no such amorphous phase was observed between particles in the case of nano-phase separation sintering even at 1300 °C. We therefore conclude that nano-phase separation sintering is distinct in mechanism from solid-state activated sintering. The distinction can be also quantitatively confirmed by thermodynamic calculations; the value of $\Delta\gamma$ of Eq. (1) in the W-15 at.% Cr system computed using the CALPHAD method is 72.4 mJ/m^2 even at 2795 °C, right below melting temperature. This quantitative analysis confirms that forming a disordered intergranular film is thermodynamically unfavorable.

iii) Liquid phase sintering

We measured the size of the Cr-rich layer for several specimens, which were at different densities and attained at different temperatures. Figure *3.11* shows the Cr layer thickness as a function of temperature during a TMA heating cycle. The size of the Cr-rich layer may be constant over the range of temperatures relevant to nano-phase separation sintering. What is

more, the trend in Figure *3.11*(a) suggests a possible increase in the Cr layer thickness. The increasing layer thickness as a function of density is at odds with the trends observed in liquid phase sintering, where densification would lead to flow and compression of these layers.

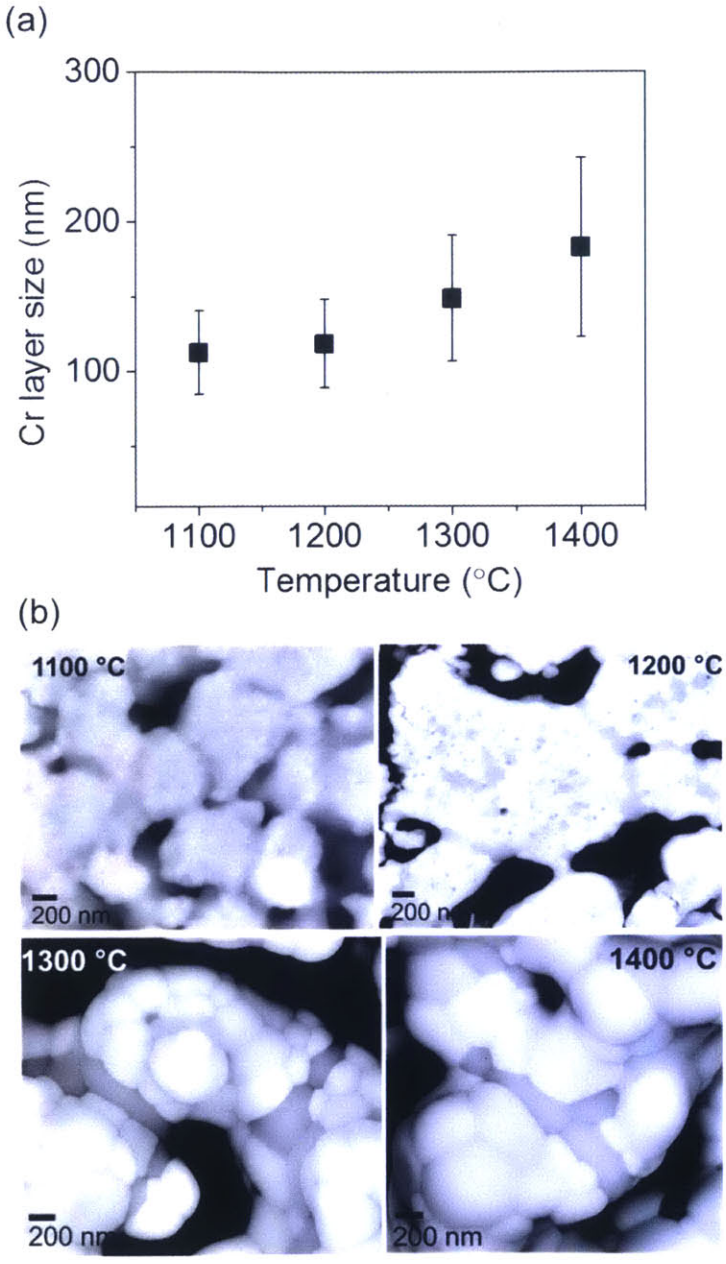

Figure 3.11 (a) The thickness of the Cr-rich layer during sintering as a function of temperature. (b) SEM micrographs in back-scatter mode of W-15 at.% Cr at various temperatures.

Therefore, the densification shape change is accommodated by W relocation, not the mechanical squashing of the Cr phase. This is in contrast to liquid phase sintering, where the second phase accommodates the shape change. The W-Cr phase diagram provides additional evidence that liquid-phase sintering is not active; the temperature where liquid phase starts to appear is around 2800 °C in the W-15 at.% Cr system (*58*), which is much higher than the onset of sintering, ~950 °C.

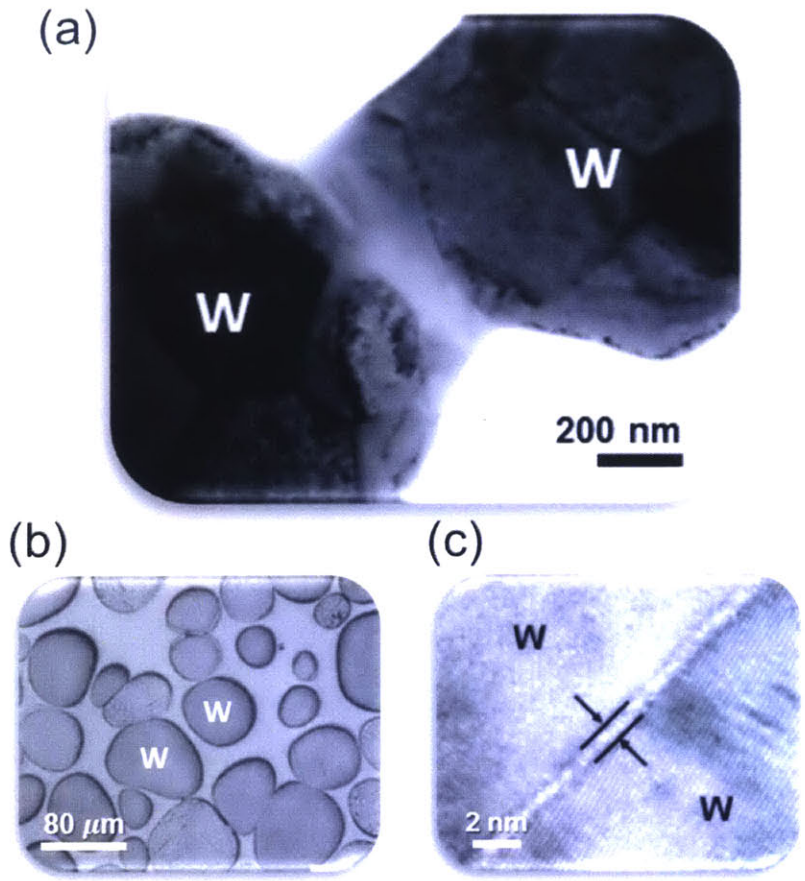

Figure 3.12 The comparison is illustrated with typical microstructures of (a) nano-phase separation sintering, (b) liquid phase sintering (*26*), and (c) solid-state activated sintering (*21*).

The microstructures resulting from nano-phase separation, liquid phase, and solid-state activated sintering are shown in Figure *3.12*. In liquid phase sintering (*26*), Figure *3.12*(b), W particles are

embedded in a liquid matrix that is a rapid transport path. In solid-state activated sintering (*21*), Figure *3.12*(c), a disordered film at grain boundary acts as a rapid transport path. In nano-phase separation sintering, Figure *3.12*(a), the separation of the supersaturated solution decorates the interparticle necks with a second solid phase that is a rapid diffusion pathway. Therefore, nano-phase separation sintering is distinct in both mechanism and resulting microstructure from solid-state activated sintering and liquid phase sintering.

3.4.2 Grain size

As retention of fine grain sizes during sintering is of technological importance, the microstructure of the compacts was investigated. The SEM micrograph in *Figure 3.13*(a) shows the final microstructure of the fully sintered compact of nanocrystalline W-15 at.% Cr after the sintering cycle of *Figure 3.1*. *Figure 3.13*(b) details the change in the compact's grain size as a function of relative density. The compact exhibits an average grain size in the range of 500~800 nm above 90 % relative density.

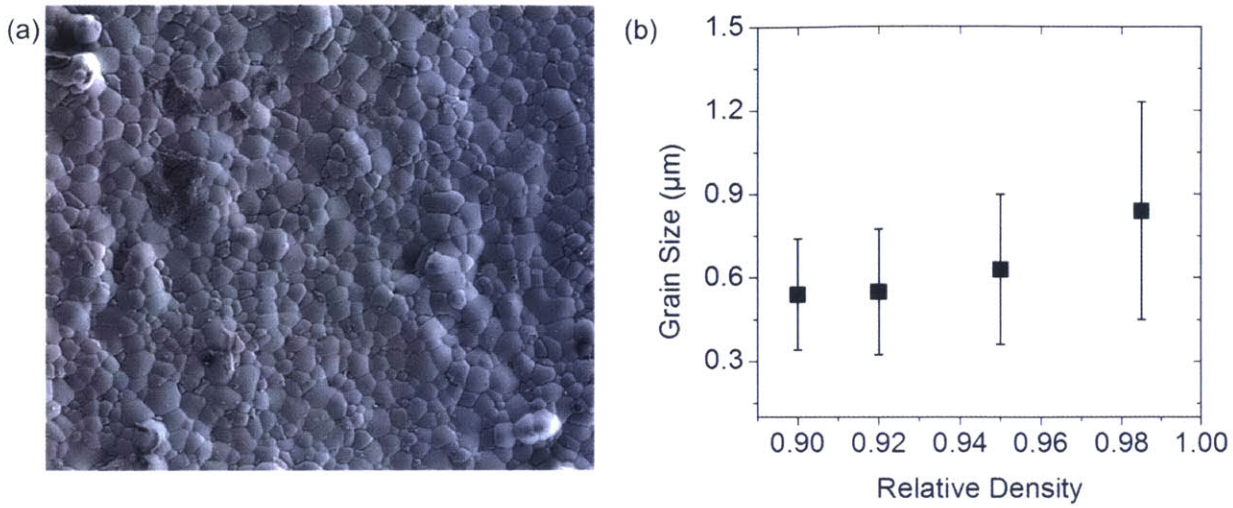

Figure 3.13 (a) The SEM micrograph of W-15 at.% Cr after sintering. (b) The change in grain size of W-15 at.% Cr as function of density.

Although the compact in Figure *3.13*(b) was produced using an unoptimized arbitary thermal cycle of constant heating rate, the grain size attained through nano-phase separation sintering is found to be much smaller at comparable relative density compared to those of other sintered products. For example, solid-state activated sintering results in grain sizes from 3~50 microns (*20, 21, 84*) and liquid phase sintering results in grins sizes less than 100 microns (*26, 27, 29, 85*). Evidently, nano-phase separation sintering is more suitable for producing nano- or ultrafine grained structures (*30*). *Figure 3.14* visually represents each sintering method in terms of its achievable grain size and relative densities. Nano-phase separation sintering occupies a unique area of grain size-relative density map.

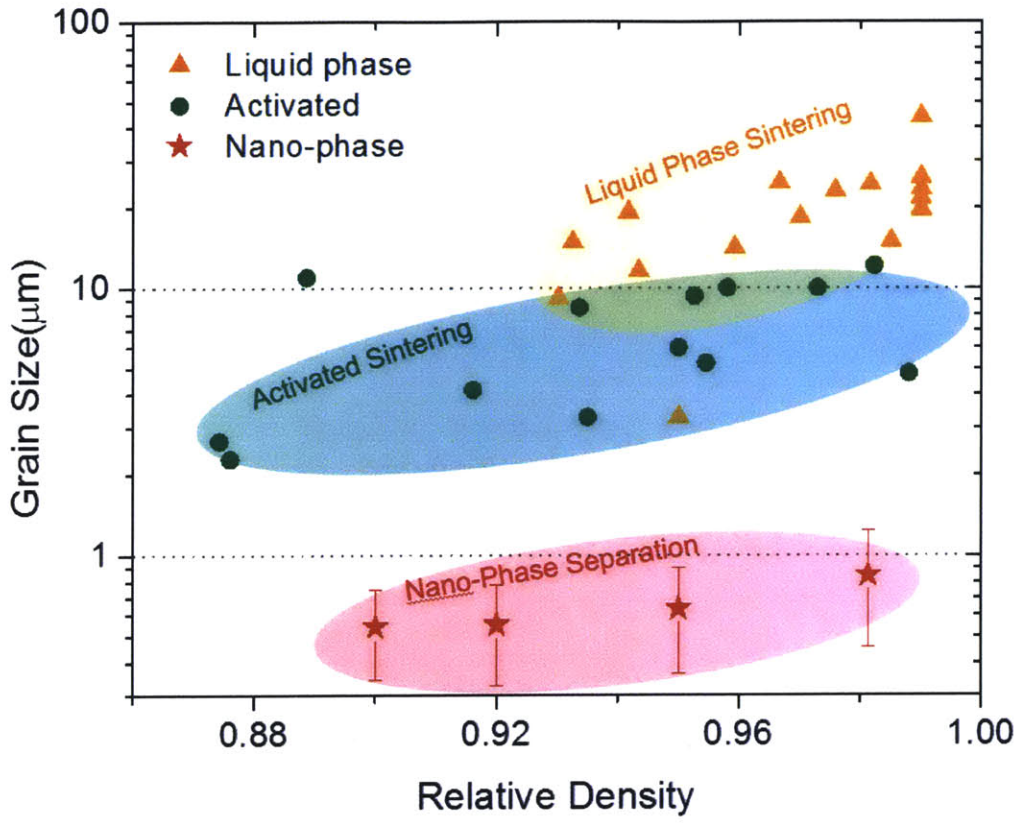

Figure 3.14 The comparison of nano-phase separation sintering with activated sintering and liquid phase sintering with regards to grain size and relative density of sintered tungsten alloys.

The fine grain size which results from nano-phase separation sintering could be accomplished by second phase pinning as well as grain boundary segregation. In addition to the kinetics aspect, the fine grains of W-Cr system have also been identified to be thermodynamically stabilized where entropic stabilization induces an equilibrium state (*57*). Nano-phase separation sintering is a promising method to produce fine-grained materials, and further optimization of alloy composition as well as the temperature-time cycle should permit a large measure of control over grain sizes in the ultrafine-to-nanoscale range in full-density sintered products.

3.5 The effect of process variables

3.5.1 Milling time

The effect of milling time of W-15 at.% Cr on powder densification behavior was investigated. *Figure 3.15*(a) shows the change in relative density of several compacts of W-15 at.% Cr as function of temperature for several different milling times. The densification is gradually accelerated with increasing ball milling time.

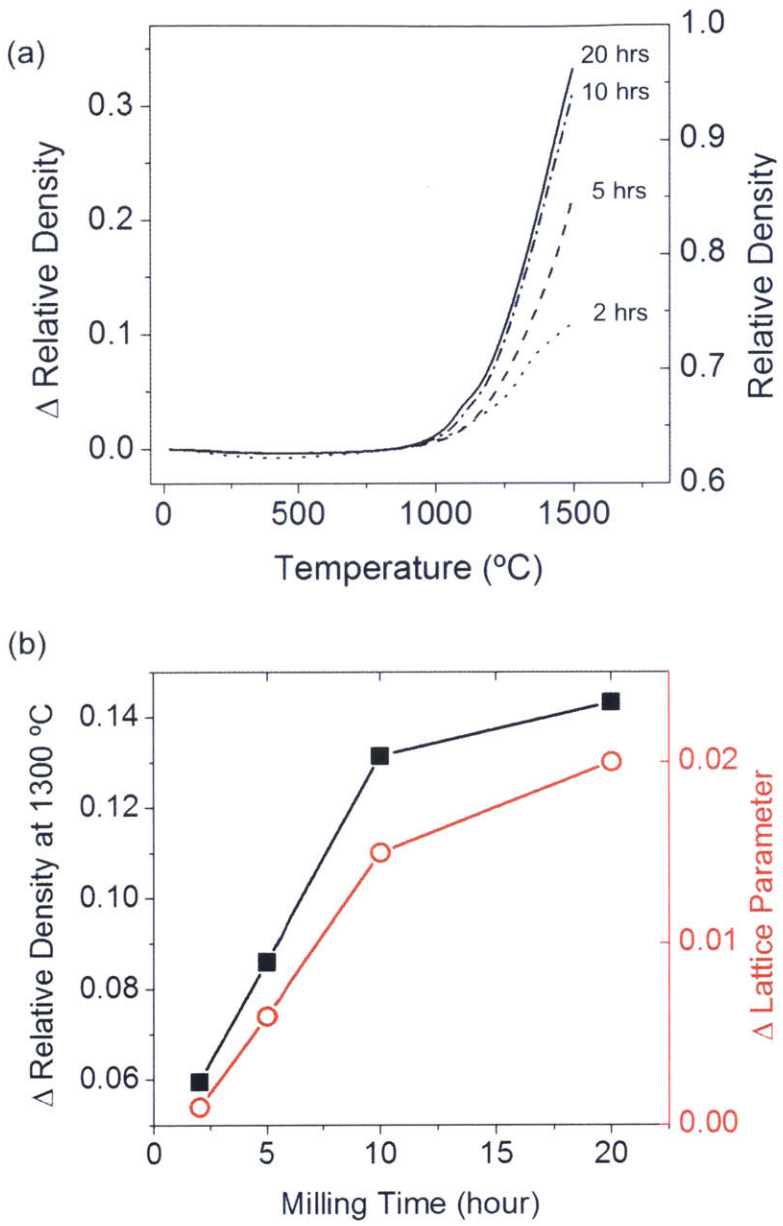

Figure 3.15 (a) The change in the relative density of W-15 at.% Cr as a function of temperature for powders milled for various times. (b) The relative density at 1300 °C (black), change in lattice parameter before annealing (red), and as-milled grain size (blue) of various samples as a function of milling time.

Figure 3.15(b) delineates the amount of relative density change at a specific temperature of 1300 °C (square points) and lattice parameter change before annealing (circle points) as a function of milling time. It is informative that these two parameters follow the same trend. The

change in the tungsten lattice parameter after milling represents the degree of supersaturation, suggesting that more Cr is dissolved into W with increasing milling time. More dissolved Cr leads to more precipitation of Cr-rich phases at high temperatures. Such precipitates are needed to form the Cr-rich neck between tungsten particles where accelerated sintering actually occurs. This result aligns with no densification of W-Cr 15 at.% in the absence of supersaturation (purple line) in *Figure 3.9*; it is the amount of the precipitated Cr-rich second phase rather than initial Cr content before milling that causes the rapid rate of densification. One thing to note in Figure *3.15*(a) is that the onset of sintering of each compact is gradually pulled down to lower temperature with increasing milling time. This is due to the fact that increasing supersaturation lowers the activation barrier to nucleation; the critical free energy of nucleation of the Cr-rich phase scales as $\Delta G_{crit} \propto 1/(lnS)^2$, S: the degree of supersaturation, and ΔG_{crit}: the critical free energy of nucleation (*86*). The lower activation barrier leads to noticeable second phase precipitation at lower temperatures. In addition, increasing milling time leads to more crystal defects which become possible heterogeneous nucleation sites and also assist the early onset of sintering. Volume fraction of crystal defects within the powders is roughly proportional to the inverse grain size. Measurements of the grain size as shown in Figure *2.8*(b) demonstrate that the volume fraction of crystal defects increases abruptly during the first 5 hours of milling.

3.5.2 Cr content

The effect of Cr content before ball milling on densification was investigated through isochronal milling of powders with varying Cr content. Figure *3.16* shows the sintering curves of the resulting powders, demonstrating that the rate of densification increases with increasing Cr content.

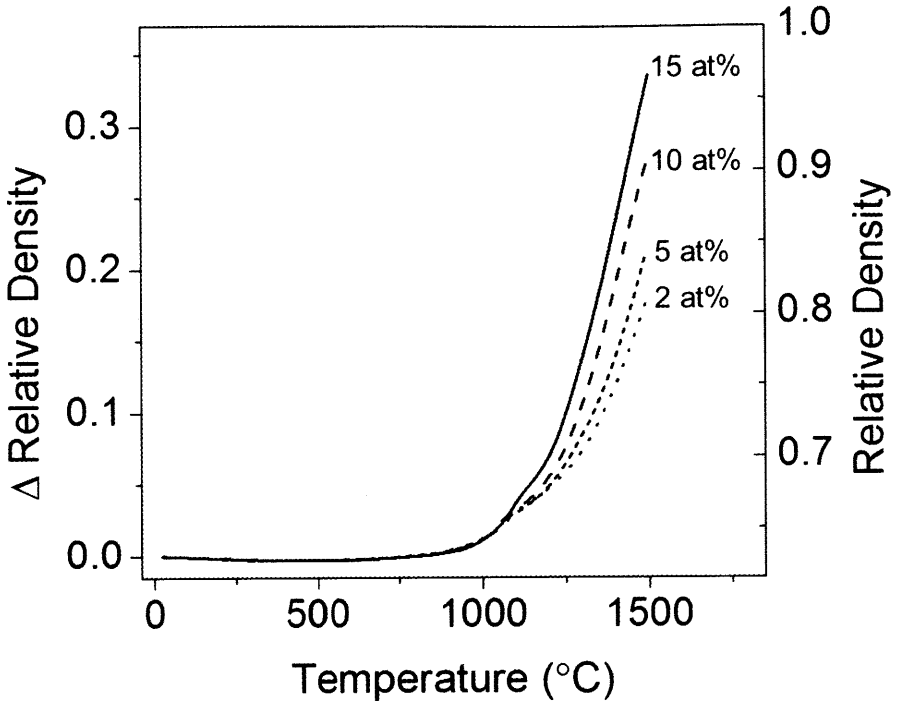

Figure 3.16 The change in relative density of W-Cr systems with various initial Cr contents.

Since the degree of supersaturation increases with increasing initial solute content (*60*), more Cr is available in solution to precipitate and form the Cr-rich necks needed to accelerate sintering. The above discussion in 3.5.1 and 3.5.2 suggests that a variety of sintered compacts with different densification behavior could be obtained by controlling alloy composition and ball milling time.

3.6 Applicability to larger samples

In order to confirm that the mechanism of nano-phase separation is insensitive to sample size, a 15 mm diameter and 11 mm height cylindrical sample was sintered in a normal high temperature furnace under Ar + 3% H_2 atmosphere. The sample shown below in Figure *3.17*, achieved full

density (> 98%) under the same conditions specified in section 3.1, verifying that the mechanism of nano-phase separation sintering remains operative at larger sample sizes and in a conventional furnace.

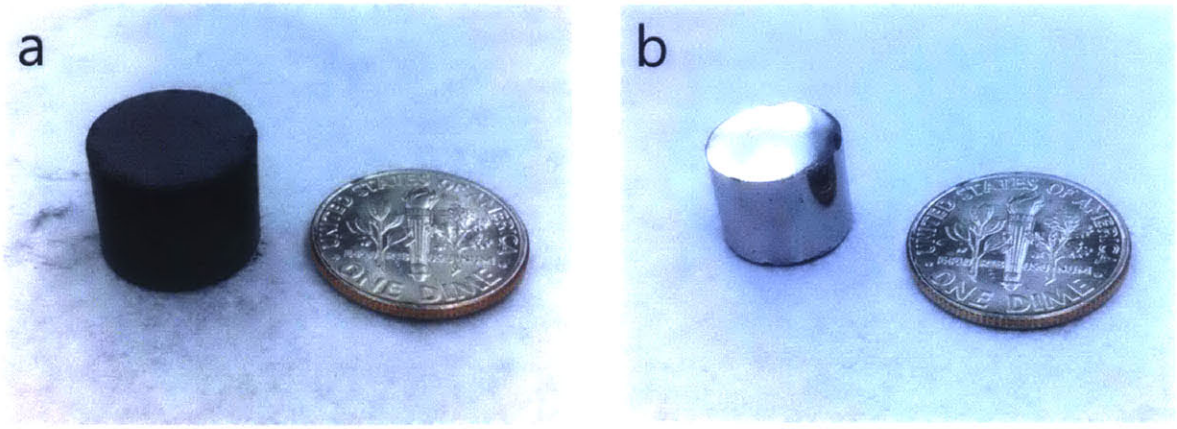

Figure 3.17 The large size sample of W-15 at.% Cr (a) before sintering, in the as-pressed condition and (b) after pressureless sintering in a furnace and cleaning.

We thus believe that the mechanism of nano-phase separation sintering is a fundamentally scalable process and that this method thus could be useful in industrial settings.

Chapter 4 Generalization to Other Systems

The above section demonstrated a dramatic acceleration of sintering in a nanocrystalline W-15at.% Cr alloy, and this acceleration was argued to arise specifically due to the nature of the system as being both nanocrystalline, and capable of phase separation to develop rapid transport pathways during the sintering cycle. The specific example of W-Cr is interesting and potentially useful for applications such as those described in the introduction. However, the prospect of a new, generalizable rapid sintering method for many different nanostructured alloys increases the potential application of this thesis research many fold. In this chapter we discuss the conditions under which the same kind of accelerated sintering might be possible in other alloy systems, and proceed to provide a proof-of-concept demonstration for a second (non-tungsten) alloy system.

4.1 Thermodynamic conditions for nano-phase separation sintering

Nano-phase separation is accomplished only when the system is processed as a non-equilibrium 'supersaturated' and 'nanocrystalline' powder, as established for the W-Cr system through the several control experiments in section 3.3. With increasing temperature, the system evolves toward equilibrium, and its thermodynamic characteristics can help understand how phases behave upon heating.

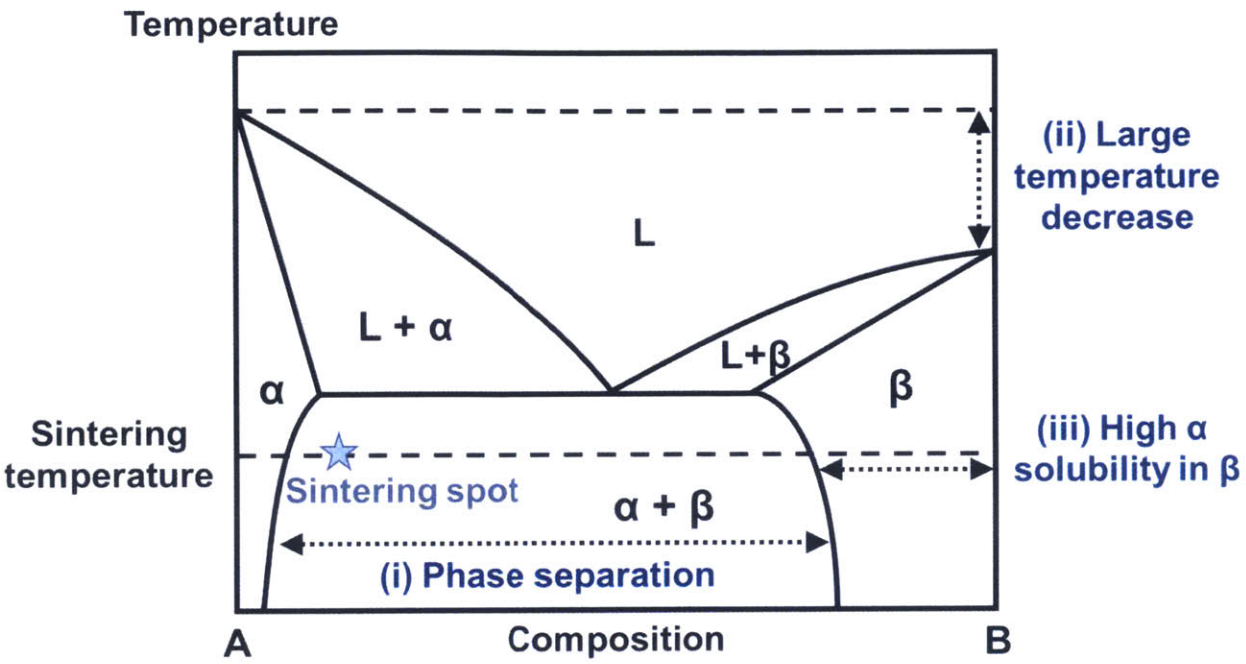

Figure 4.1 A model binary phase diagram showing the optimum spot and three thermodynamic conditions for nano-phase separation sintering.

Figure *4.1* shows a model binary phase diagram on the composition and temperature axes, delineating the features that we believe to be conducive to nano-phase separation of an A-rich alloy. A system that would exhibit nano-phase separation sintering would tend to lie at a location such as that denoted by the star at the sintering temperature of interest. The optimum condition would be at a composition within the α + β region. The key thermodynamic features of nano-phase separation sintering could be categorized into three parts.

1. First, a binary alloy pair should possess a phase separation region in order to achieve a supersaturated powder after processing. In addition, this phase separation region should be extended above a sintering temperature of interest so that system can still retain the driving force for phase separation at a sintering temperature. In order that a relatively

low level of alloying can be used to accelerate sintering, a low solubility of B in the A-rich phase would seem to be preferred.

2. Second, the minority element (B) should provide a fast transport pathway to the base element (A) atoms. To a first approximation, the diffusion rate should scale with the melting temperature of the second element, which therefore should have a lower melting temperature than the base element. A larger difference in melting temperatures would lead to the onset of sintering of the base element at a lower temperature and a faster densification rate.
3. Third, the precipitated second phase should be capable of dissolving the base element which, as temperature increases, diffuses through the second phase, acting as a fast transport layer on particle surfaces and necks. Therefore a high solubility of A in the B-rich phase is preferred.

These thermodynamic characteristics align with those of the equilibrium phase diagram of the W-Cr system as shown in *Figure 2.5*. Other binary systems which satisfy three thermodynamic conditions discussed would include at least the following: Fe-Mo, Fe-Ni, Mn-Ti, Mn-Ni, Fe-Mn, Mo-Ni, Mo-Ru, W-Ru, Mo-Re, Ni-Ru, Nb-Ni, Ni-V, Pd-Ta, Pd-Rh, Re-W, Pt-W, Hf-Ta, Ta-V, Al-Zn, Ag-Al, Ag-Cu, Ag-Pt, As-Ge, Au-V, Au-Ni, Ni-Be, Be-Cu, Co-V, Co-Cu, Co-Ti, Mo-Cr, Cr-Re, Cr-Fe, Cr-Ru, Cr-Nb, Cr-Ni, Cr-Ti, Cu-Mn, Ag-Cu, Cu-Ti, Fe-Ti, and Fe-V.

As a first step to establish the generality of this approach, we select one of these systems to subject to further proof-of-concept testing. Since Cr is another metal known to be challenging to sinter, we select it as the base metal for this experiment. The equilibrium phase diagram of Cr-Ni in Figure *4.2* shows that the Cr-Ni system satisfies three thermodynamic conditions: (i) the Cr-Ni system exhibits a miscibility gap, (ii) nickel has a significantly lower melting temperature than

chromium, and (iii) the Ni-rich phase has a large solubility of Cr, but the Cr-rich phase has a relatively lower solubility for Ni; the Ni-rich phase is therefore formed at relatively low Ni additions, and would tend to dissolve (and transport) a great deal of Cr.

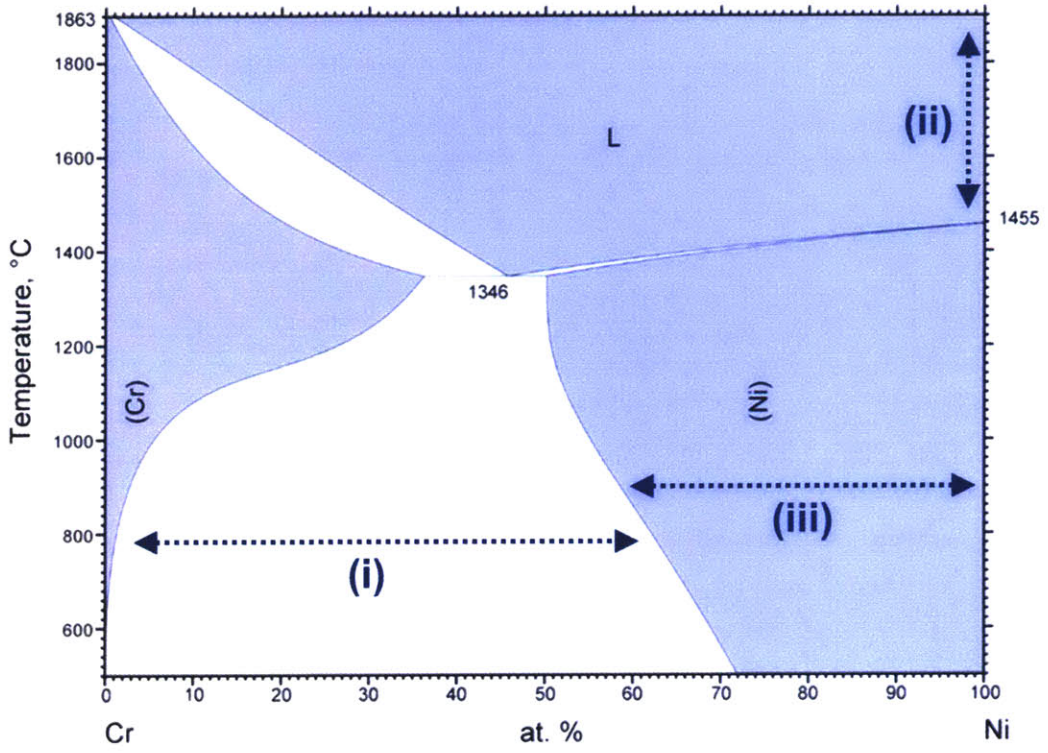

Figure 4.2 Equilibrium phase diagram of Cr-Ni alloy (*58*).

4.2 The Cr-Ni system

In order to achieve nanocrystallinity, one of the conditions for nano-phase separation sintering, high-energy ball milling was employed for the purpose of the grain refinement, similar to the W-Cr system in Chapter 2. Cr and Ni powder were mechanically alloyed using the same procedure outlined in section 2.1 for 15 hours of milling and the resultant alloyed powder was characterized.

4.2.1 Characterizations of pre-sintering powders

i) Supersaturation

Extended solubility in the Cr-Ni system could result from forced atomic mixing during high-energy ball milling (*65-68*), which is established through XRD, TEM-selected area diffraction, and STEM-EDS. XRD patterns of Cr-15 at.% Ni are measured with increasing milling time from 0 to 15 hours as shown in Figure *4.3*(a) which shows a gradual decrease in the intensity of Ni peaks denoted by the red stars. Figure *4.3*(b) represents the change in the Cr (110) peak, which eventually disappeared after reaching 15 hours of milling.

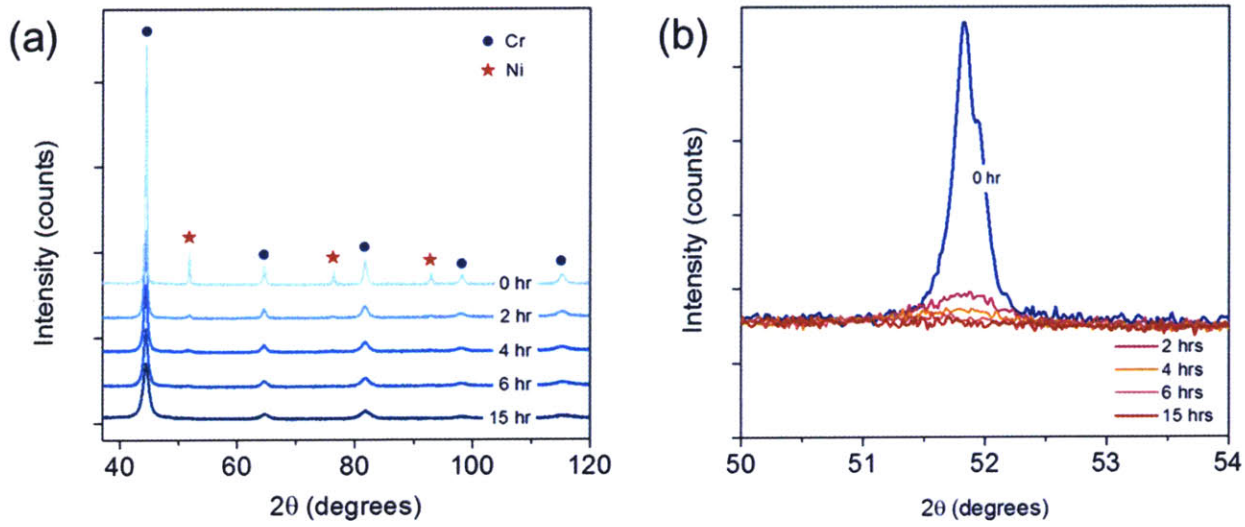

Figure 4.3 (a) X-ray diffraction patterns of Cr-15 at.% Ni with various milling time (b) The change in the Ni (110) peak with increasing milling time.

After 15 hours of milling, the electron diffraction pattern of Cr-15 at.% Ni shown in the inset of Figure *4.5*(b) displays only chromium bcc rings without showing any diffraction spots related to nickel, implying that Ni is completely dissolved into Cr. This chromium solid solution would not

be expected based on the equilibrium phase diagram of Cr-Ni system which depicts complete separation at room temperature due to almost no Ni solubility in Cr as shown in Figure *4.2* (*58*). The resultant solid solution also aligns with the elemental measurement of Cr and Ni obtained through STEM-EDS along with the dark-field STEM image in Figure *4.4*, showing that Ni is uniformly distributed over the Cr particle in absence of a perceptible contrast distinction.

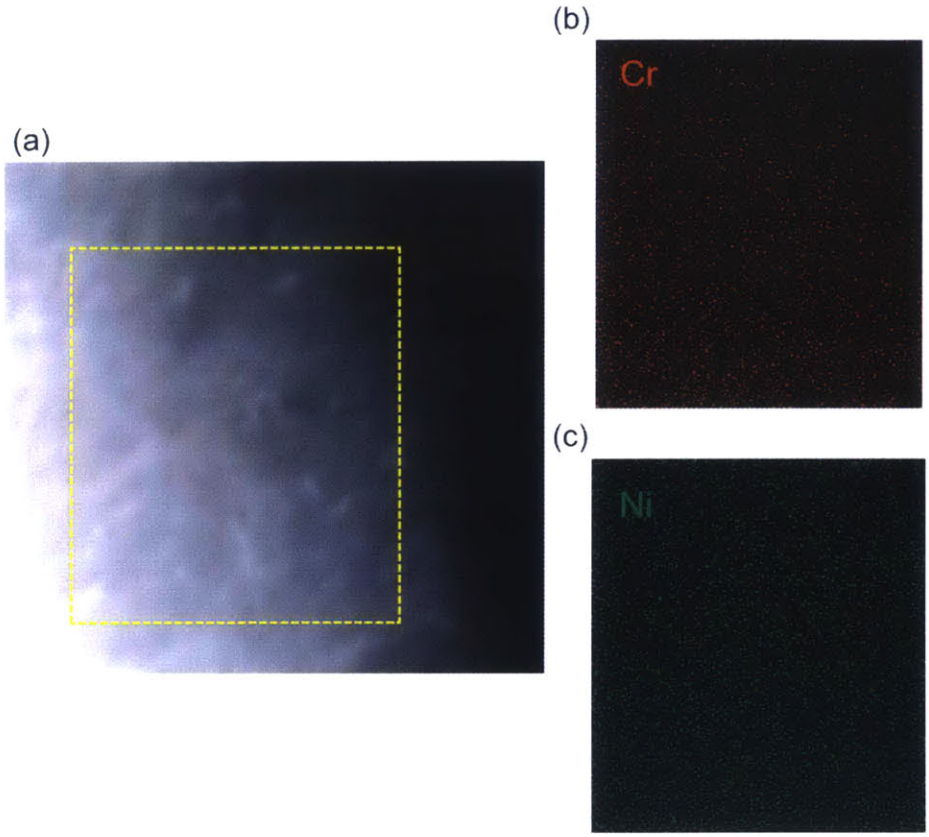

Figure 4.4 (a) A dark-field STEM micrograph of nanocrystalline Cr-15 at.% Ni after 15 hours of ball-milling with energy dispersive spectroscopy (EDS) measurements of (b) Cr and (c) Ni.

All datasets acquired from XRD, TEM, and STEM-EDS indicate that Cr-15 at.% Ni turns into a supersaturated solid solution after 15 hours of high-energy milling.

ii) Particle and grain size

The TEM micrograph of as-milled chromium with an addition of 15 at.% nickel in Figure *4.5*(b) exhibits nanoscale grains. The average grain size is 12 nm, which is in agreement with the value assessed by the Rietveld refinement method.

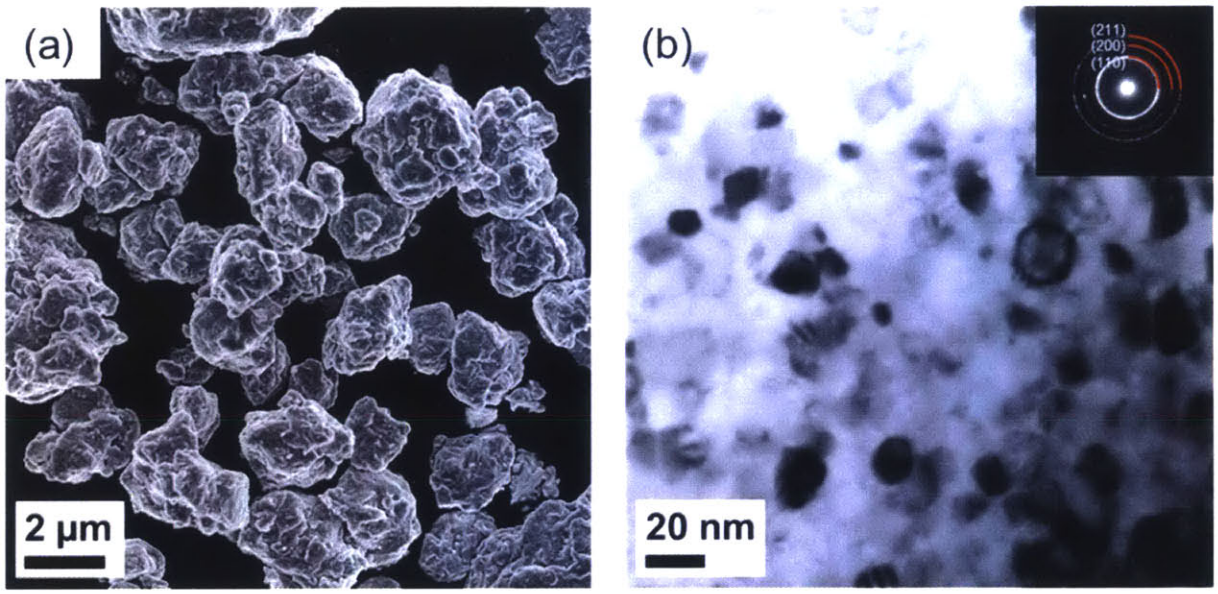

Figure 4.5 (a) An SEM micrograph and (b) a TEM micrograph of the as-milled Cr-15 at.% Ni powder.

As seen in ball milling processing of other alloy powders (*62, 63*), Cr-15 at.% Ni after 15 hours of milling is also composed of microscale polycrystalline particles with nanoscale grains. The SEM micrograph in Figure *4.5*(a) shows micron-sized particles of the as-milled powder, and their average size measured by the laser diffraction particle size analyzer is 4.3 µm (Figure *4.6*).

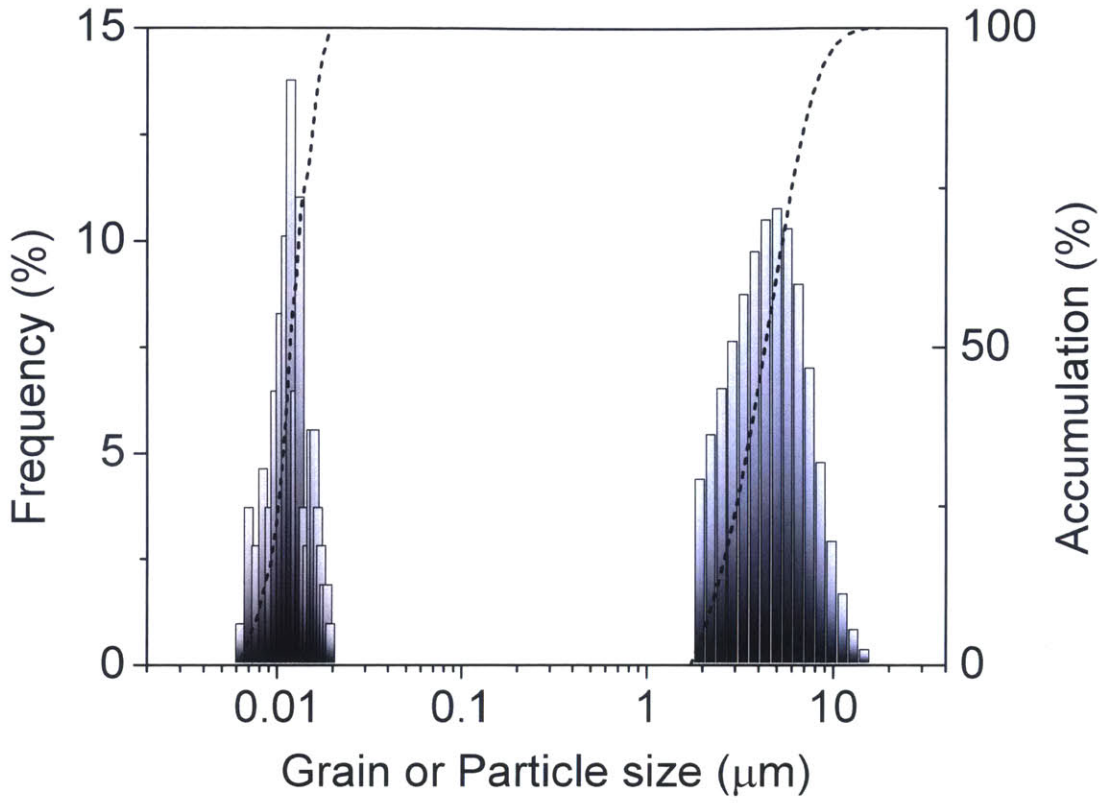

Figure 4.6 The comparison of grain and particle size distribution of as milled powder of Cr-15 at.% Ni after 15 hours milling.

The comparison in size distribution between particles and grains in Cr-15 at.% Ni after 15 hours of milling is facilitated by Figure *4.6*, which illustrates each particle being constituted of nanoscale grains.

4.2.2 Characterizations of post-sintering bulk

i) Density changes

As-milled nanocrystalline Cr-15 at.% Ni powder was compacted and heated using the same procedure outlined in section 3.1. The change in density of the compact was measured using the TMA as a function of temperature without any external force. As shown in Figure *4.7*, the compact (labeled nc-Cr(15 at% Ni)) starts to densify at low temperature, ~600 °C, and shows an abrupt surge in the relative density at around 1050 °C.

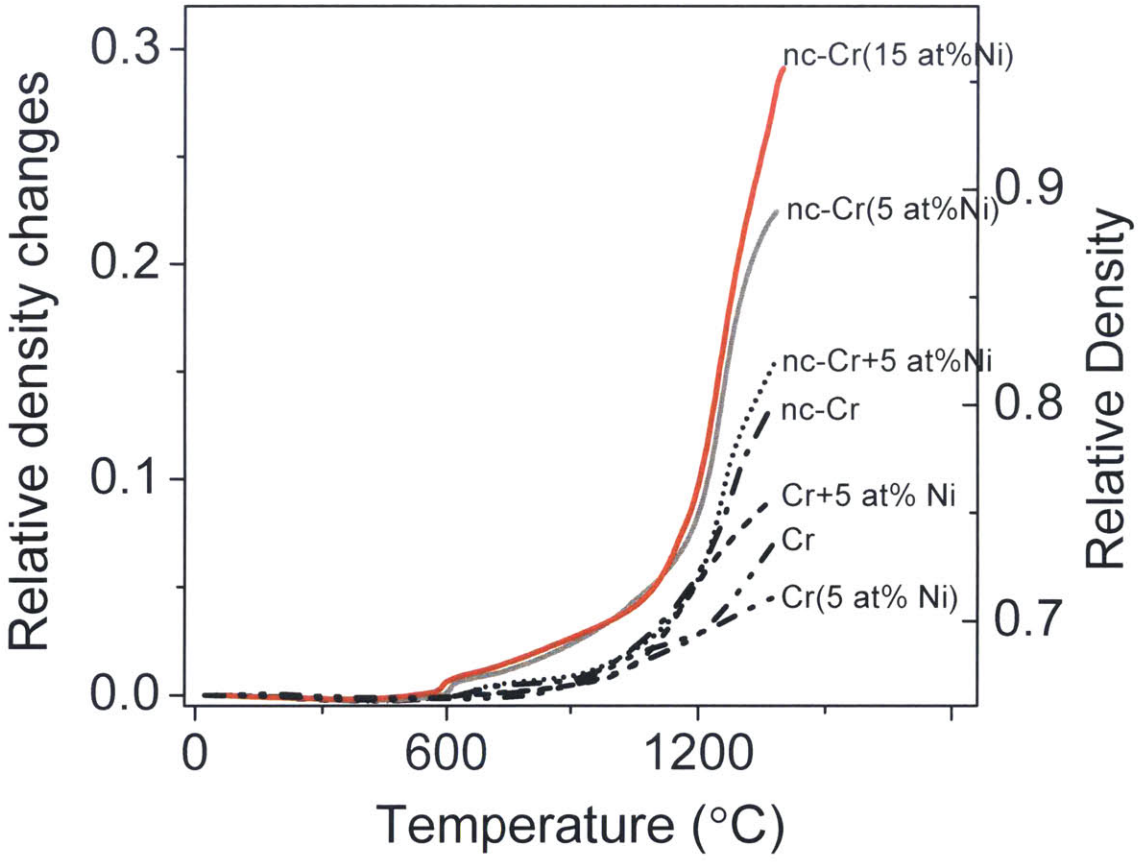

Figure 4.7 Changes in relative density of nanocrystalline Cr-15 at.% Ni shown with a series of control experiments upon heating.

The acceleration of consolidation is more drastically revealed when compared to the sintering of conventional chromium powder (micron-sized particle, labeled Cr); it shows only 0.07 change in relative density while nanocrystalline Cr-15 at.% Ni displays a 0.29 change after reaching

1400 °C. Even with the addition of 5 at.% Ni into Cr, densification is accelerated (nc-Cr(5 at% Ni). Multiple control experiments (nc-Cr, nc-Cr+5 at% Ni, Cr+5 at%Ni, Cr (5 at% Ni)) related to Cr-5 at.% Ni were prepared using the same procedure outlined in section 3.3 and heated as shown in Figure *4.7*. Their poor sinterability supports the idea that the accelerated sintering in Cr-Ni systems is achieved by nano-phase separation sintering.

ii) Structure changes

High-energy ball milling generates a non-equilibrium Cr-15 at.% Ni, suggesting that the second Ni-rich phase would precipitate at high temperature. Based on the mechanism of nano-phase separation sintering, this Ni-rich precipitated phase, which preferentially decorates particle surface and forms an interparticle neck (*73, 74*), would offer a fast transport layer for Cr atoms, which accelerates the sintering kinetics of chromium. Thus, one of the most crucial check points in microstructure is whether a Ni-rich phase precipitates and consequently forms interparticle necks between the chromium particles after the onset of sintering. An SEM-EDS measurement of local chromium and nickel composition superimposed on the SEM micrograph in Figure *4.8*(a) visually illustrates a Ni-rich neck and Cr-rich particles. This SEM-EDS measurement suggests that a Ni rich-phase is ejected out of the supersaturated chromium solid solution upon sintering and preferentially deposited between two Cr-rich particles.

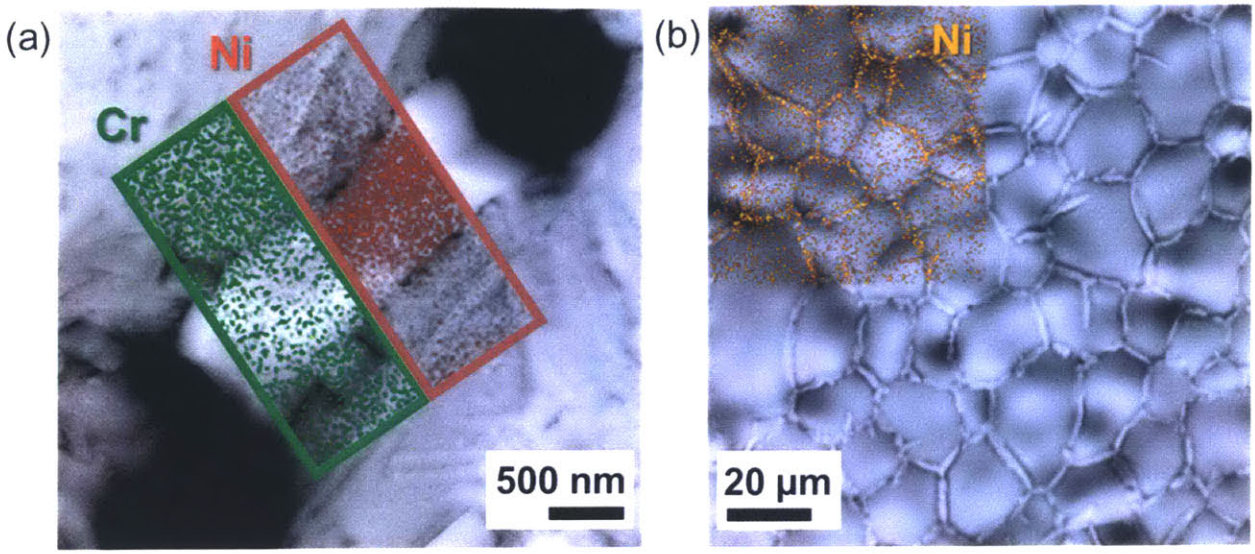

Figure 4.8 Post-sintering microstructures of Cr-15 at.% Ni alloy. (a) The SEM micrograph with EDS measurements of local composition of Cr and Ni reveals a nickel-rich phase forming necks between the compact particles upon heating. (b) A direct visualization of Ni-rich necks entirely enclosing Cr-rich particles is shown with Cr and Ni elemental measurement (superimposed on the SEM micrograph) using SEM-EDS.

In addition, a substantial amount of dissolved chromium in the Ni-rich neck as shown in Figure *4.8*(a) indicates that the Ni-rich phase is capable of dissolving and transporting Cr atoms, which is expected with increasing temperature based on the equilibrium phase diagram of the Cr-Ni system (*58*). The microstructure after sintering is presented in Figure *4.8*(b), showing the Ni-rich precipitates completely enclosing the Cr-rich particles. The acceleration on sintering kinetics of nano-phase separation sintering is accompanied by the exquisite usage of the fact that sintering is generally all about the transport of atoms to the neck between particles and that this very neck is thermodynamically favorable for phase separation.

iii) Sintering activation energy and kinetics

Assessing the characteristic quantity of a sintering activation energy and comparing it to a reference are significant for quantitatively corroborating that nano-phase separation sintering is in active operation. The master sintering curve method (*75, 76*) is used to estimate the sintering activation energy. The several density-temperature profiles of nanocrystalline Cr-15 at.% Ni were acquired at heating rates of 3, 5, 10, 15, and 20 °C/min. The raw density-temperature profiles are represented in Figure *4.9*.

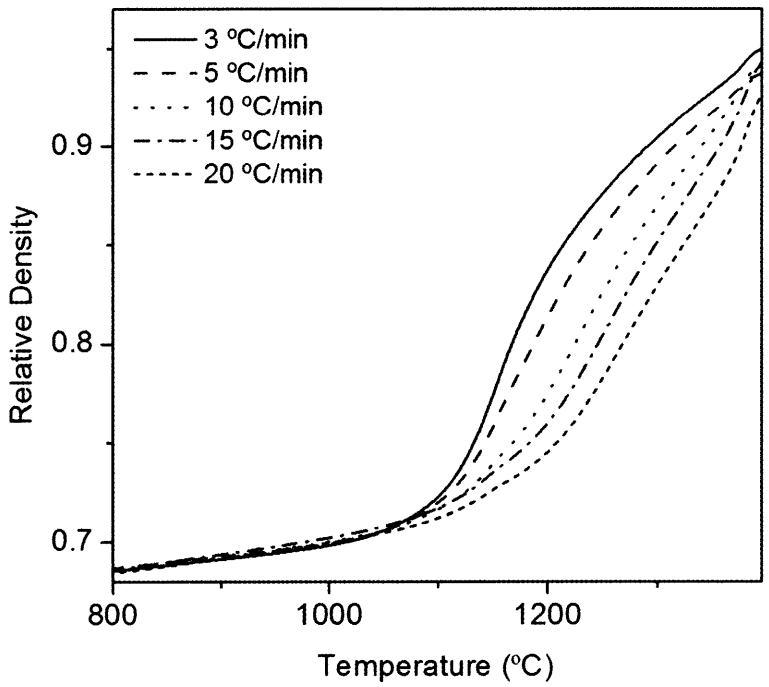

Figure 4.9 Density-temperature profiles of nanocrystalline Cr-15 at% Ni as a function of temperature at heating rates of 3, 5, 10, 15, and 20 °C/min.

Sintering profiles collected over several heating rates are normalized to $\int_0^t \frac{1}{T}\exp(-\frac{Q}{RT})\,dt$. The correct value of Q is evaluated when all the normalized heating profiles are collapsed onto a single curve. The mean residual squares as a function of sintering activation energy in

nanocrystalline Cr-15 at.% Ni is presented in Figure *4.10*(a), showing the minimum value at 265 kJ/mol.

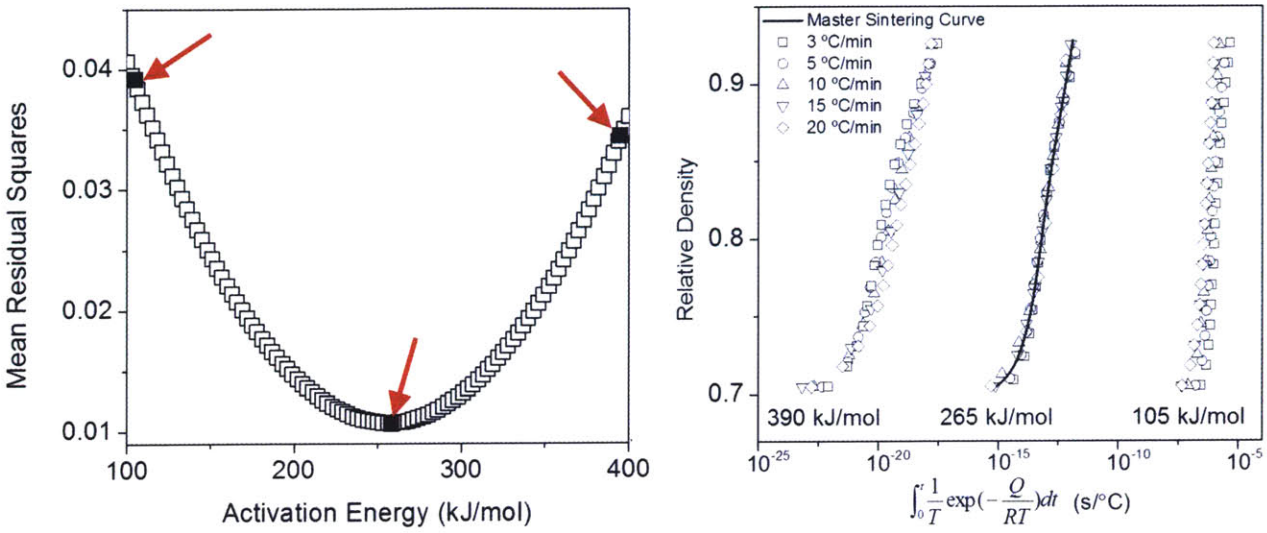

Figure 4.10 (a) The mean residual squares as a function of sintering activation energy, (b) normalized heating profiles at different activation energies at three activation energies denoted in (a).

Several normalized heating profiles at different activation energies which are denoted as three points in Figure *4.10*(a) are presented in Figure *4.10*(b), showing dispersion between normalized profiles when the correct activation energy is not chosen. Normalized heating profiles converge into a single curve at the best-fit sintering activation energy of 265 kJ/mol. This value is very close to the diffusion activation energy of chromium in nickel, 273 kJ/mol (*87*), and is much lower than for chromium self-diffusion, 435 kJ/mol (*88*), which normally controls the sintering of Cr. The assessed sintering kinetics therefore conform to the expected sintering mechanism of nano-phase separation sintering where Ni-rich precipitates provide short-circuit diffusion paths to Cr atoms.

Chapter 5 Production of Nanocrystalline Bulk Tungsten Alloys

5.1 Stabilizer for suppressing grain growth

Not only is nano-phase separation sintering suitable specifically for nanostructured alloys, the addition of second phases and alloying elements is generally useful to retain nanocrystalline structures during a thermal cycle. This mechanism thus lends itself naturally to the production of fine-grained materials; ultrafine W-Cr bulk specimen could be achieved through nano-phase separation sintering in Chapter 3. One clear direction for additional work on this consolidation method is to consider not only the addition of a sintering accelerator, but to further include a ternary element to additionally suppress grain growth. When both inputs, an accelerator and a stabilizer, are employed together, nanocrystalline bulk alloys could be achieved.

In order to produce nanocrystalline bulk tungsten alloys, we should first consider which element is proper as a stabilizer for tungsten alloys. As discussed in section 2.3.1, Chookajorn et al. studied stability of nanocrystalline tungsten alloys and constructed a stability map for tungsten-based binary alloys with positive heats of mixing, shown in Figure *2.3* (*56*, *57*). Among such alloying elements, we chose Ti as a stabilizer for two reasons. First, Ti has been experimentally proved to inhibit grain growth in nanocrystalline tungsten alloy during a thermal cycle (*56, 89*). The TEM micrograph of the W-20 at.% Ti alloy microstructure after high-energy ball milling as shown in *Figure 5.1*(b) exhibits nanoscale grains and the average grain size is 22 nm.

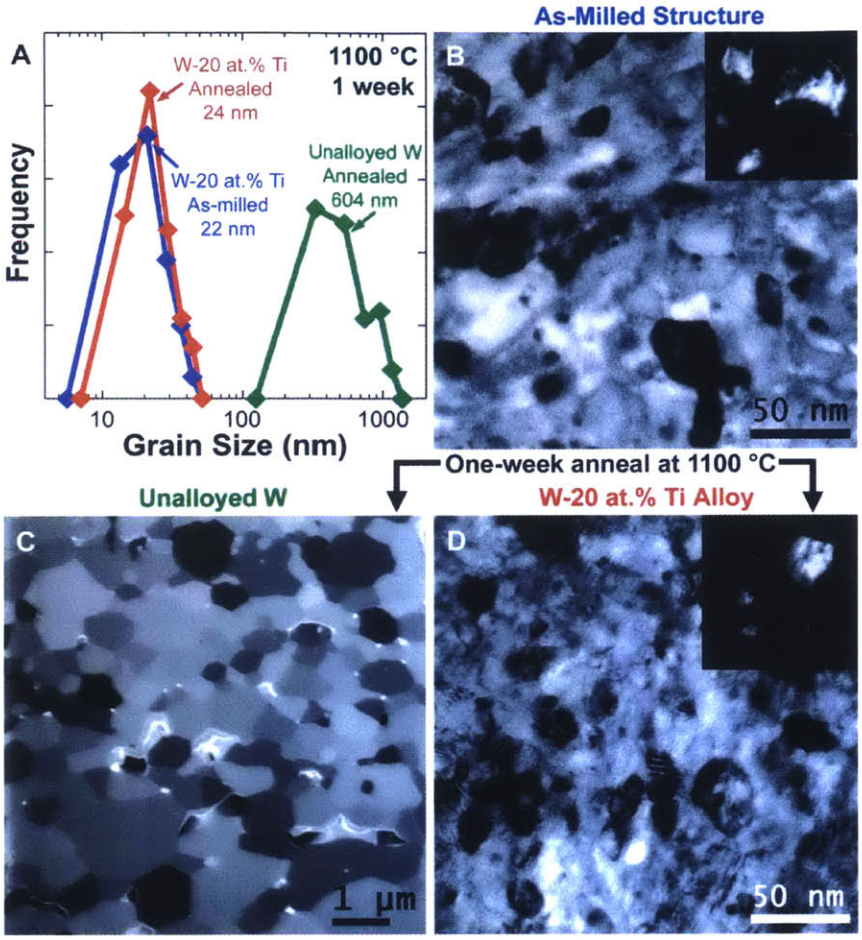

Figure 5.1 Pre- and postannealing grain structures of tungsten powders after one week at 1100°C. (a) The grain size histograms reveal only a minor change in the W–20 at. % Ti alloy after prolonged annealing and an almost two-orders-of-magnitude coarsening in unalloyed W. (b) The bright-field transmission electron microscopy (TEM) image shows a uniform distribution of nanometer-sized grains in the as-milled structure of the W–20 at. % Ti alloy, with the dark-field TEM image (inset) showing different diffracting crystallites. The postannealing structures vary with alloying: (c) a coarsened grain structure in unalloyed W, presented in a focused ion beam image, and (d) a retained nanocrystalline structure in W–20 at. % Ti, shown in a bright-field TEM image with a dark-field TEM (inset) (*56*).

After annealing at 1100 °C for a week, unalloyed W displays an average grain size of around 604 nm. In contrast, W-20 at.% Ti exhibits an average grain size of 24 nm which is almost the same as the milled powder, showing that Ti successfully suppresses the grain growth of tungsten during a thermal cycle. However, as shown earlier in Figure *2.4*, Ti does not accelerate sintering

of W. The possible addition of Cr as a sintering accelerator is therefore of interest for this system. The Ti-Cr system is a compatible one: the two elements alone form a solution at our processing temperatures based on the equilibrium phase diagram of Cr-Ti alloy shown in Figure *5.2* (*90*). It therefore seems plausible that the two elements might be combined to improve both the sinterability and thermal stability of the nanostructure in W.

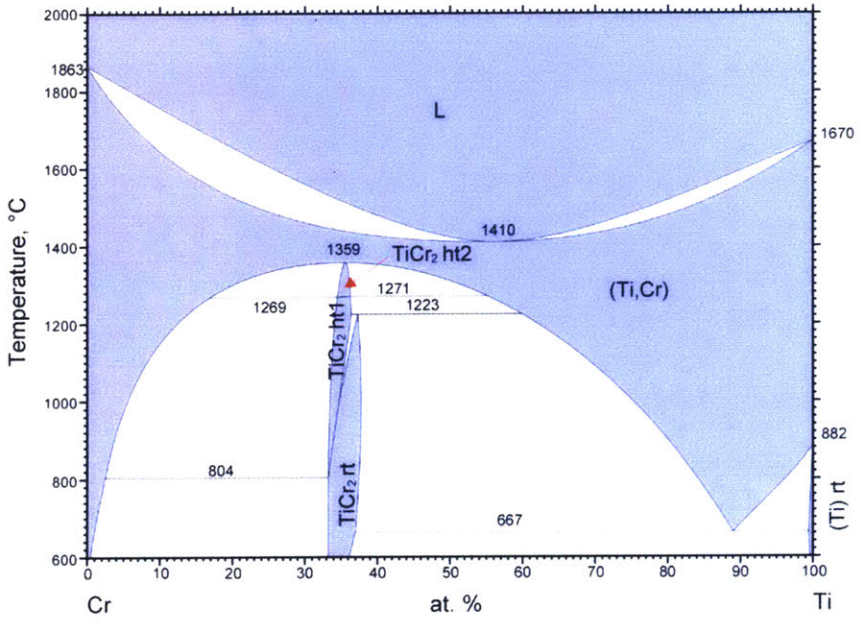

Figure 5.2 Equilbrium phase diagram of Cr-Ti alloy *(90)*.

5.2 Synthesis of W-Ti-Cr alloys

For grain refinement of powders, high-energy ball milling is employed as we did with all of the systems described in Chapter 2 and Chapter 4. W, Ti, and Cr powder were mechanically alloyed using the same procedure outlined in section 2.1. For finding a proper alloy's composition, we started with W-15 Ti-15 at.% Cr and annealed it using the same procedure outlined in section 3.1. The change in compact density is shown in Figure *5.3*.

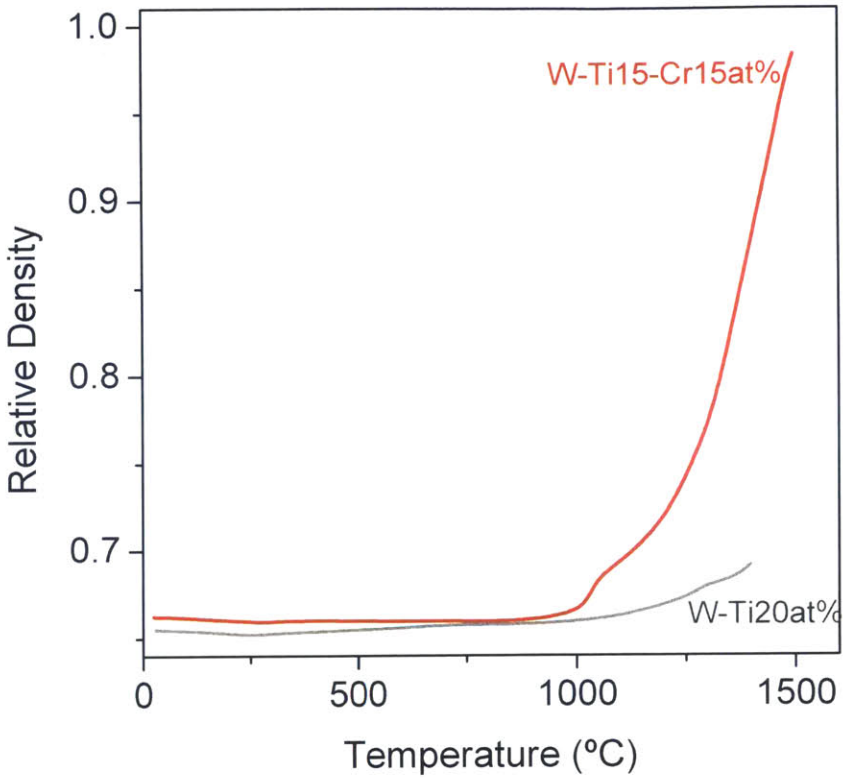

Figure 5.3 Change in relative density of nanocrystalline W-15 Ti-15 at.% Cr (red) and W-20 at.% Ti (grey).

Nanocrystalline W-20 at.% Ti alloy, which is free of the accelerator, Cr, was also prepared and annealed for comparison purposes. In contrast to nanocrystalline W-20 at.% Ti alloy, nanocrystalline W-15 Ti-15 at.% Cr starts to densify at low temperature and shows a rapid rate of densification. The grain size of W-15 Ti-15 at.% Cr after sintering is ~230 nm (shown in *Table 5.1*) which is much lower than that of W-15 at.% Cr without a stabilizer, Ti in section 3.4 (~840 nm). Figure *5.3* demonstrates that nano-phase separation sintering remains operative in the ternary alloy W-Ti-Cr system through the addition of chromium and that bulk nanocrystalline tungsten alloys could be achieved with control over the grain size through changing alloy compositions.

Table 5.1 presents the information of several W-Ti-Cr alloys that we studied, including grain sizes and relative densities of sintered products and final heating temperatures.

Table 5.2 Information of W-Ti-Cr alloys.

Alloy composition (at.%)	Initial relative density	Final relative density	Final temperature (°C)	d_{XRD} (μm)[2]	d_{SEM} (μm)[3]
W-30Ti-10Cr	0.68	0.935	1350	> 0.1	0.135
W-30Ti-10Cr	0.68	0.98	1410	> 0.1	-
W-15Ti-15Cr	0.663	0.97	1490	> 0.1	0.227
W-20Ti-15Cr	0.662	0.986	1500	> 0.1	0.264
W-35Ti-10Cr	0.69	0.983	1350 (Isothermal holding for 7 min)	0.092	0.1

Clearly, with some changes in the alloy chemistry and the thermal cycle used in sintering, the ternary W-Cr-Ti system should be amenable to a great deal of tuning to achieve an optimum combination of density and fine grains. Among the samples produced in *Table 5.1*, the last one listed has the best combination of these parameters, being genuinely nanocrystalline with d~100 nm and nearly fully dense. This alloy is examined in more detail below.

Figure *5.4* exhibits X-ray diffraction pattern of as-milled W-35 Ti-10 at.% Cr and the grain size of as-milled powder assessed by the Rietveld refinement method is 9 nm.

[2] Grain size is measured by the Rietveld refinement method.
[3] Grain size is measured by SEM micrographs.

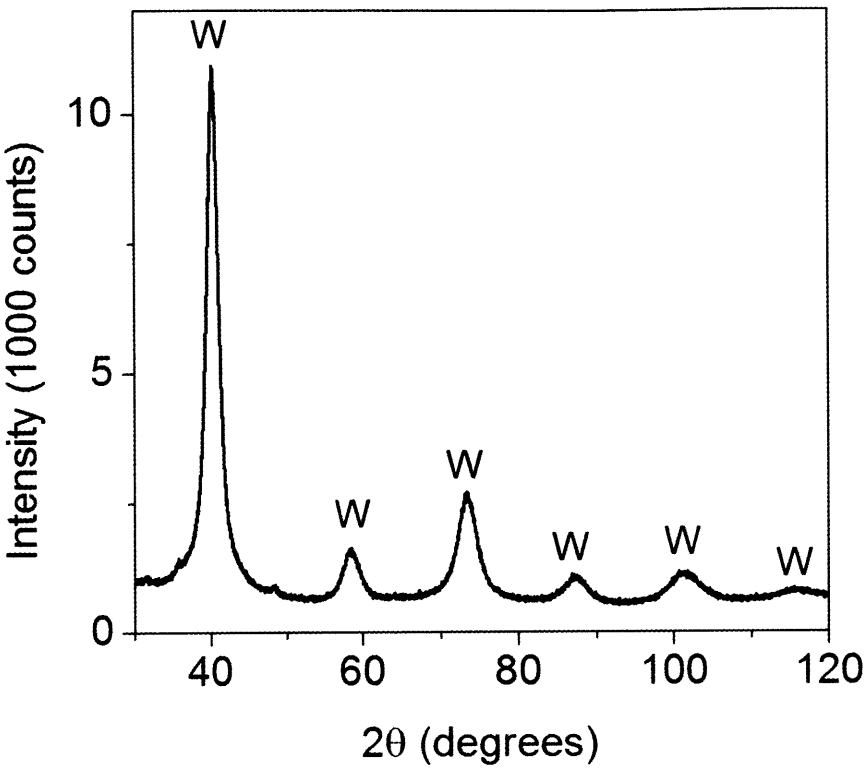

Figure 5.4 X-ray diffraction pattern of nanocrystalline W-35 Ti-10 at.% Cr after 30 hours milling.

The distribution of particle size of as-milled W-35 Ti-10 at.% Cr measured by the laser diffraction particle size analyzer is shown in Figure *5.5*, and the average particle size is revealed to be 4.5 μm. As expected, nanocrystalline W-35 Ti-10 at.% Cr after 30 hours of milling is comprised of micron-scale polycrystalline particles with nanoscale grains.

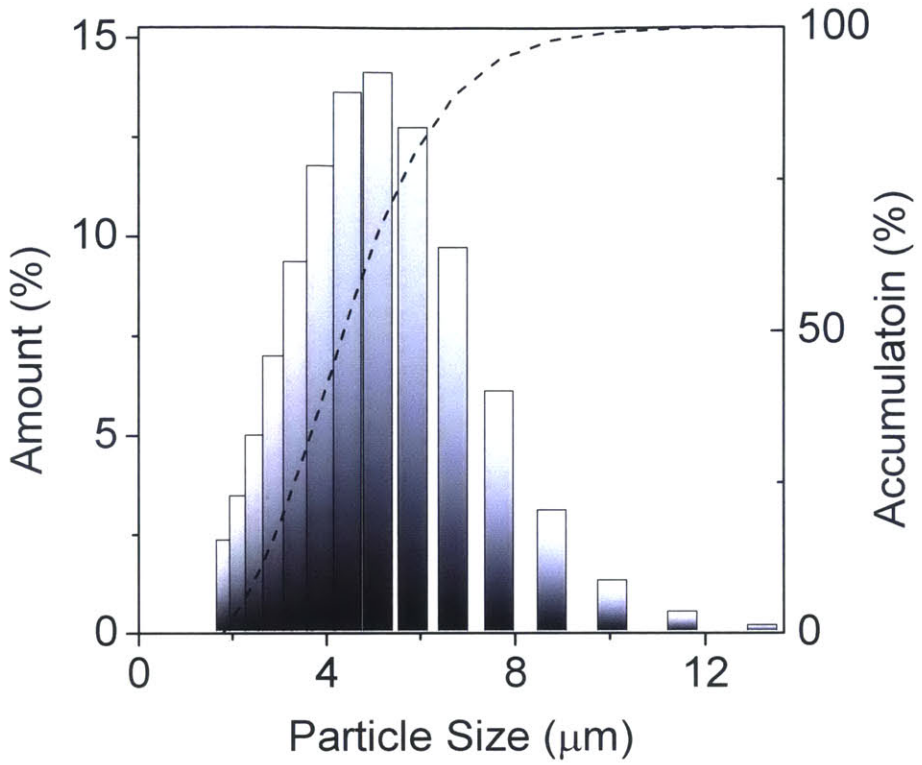

Figure 5.5 Particle size distribution of nanocrystalline W-35 Ti-10 at.% Cr after 30 hours of milling.

Compacts of nanocrystalline W-35 Ti-10 at.% Cr was pressurelessly annealed up to 1350 °C and soaked for 7 minutes under the same atmosphere outlined in section 2.1. The blue line in Figure *5.6* is the change in compact density, showing accelerated densification and almost full density after the sintering process.

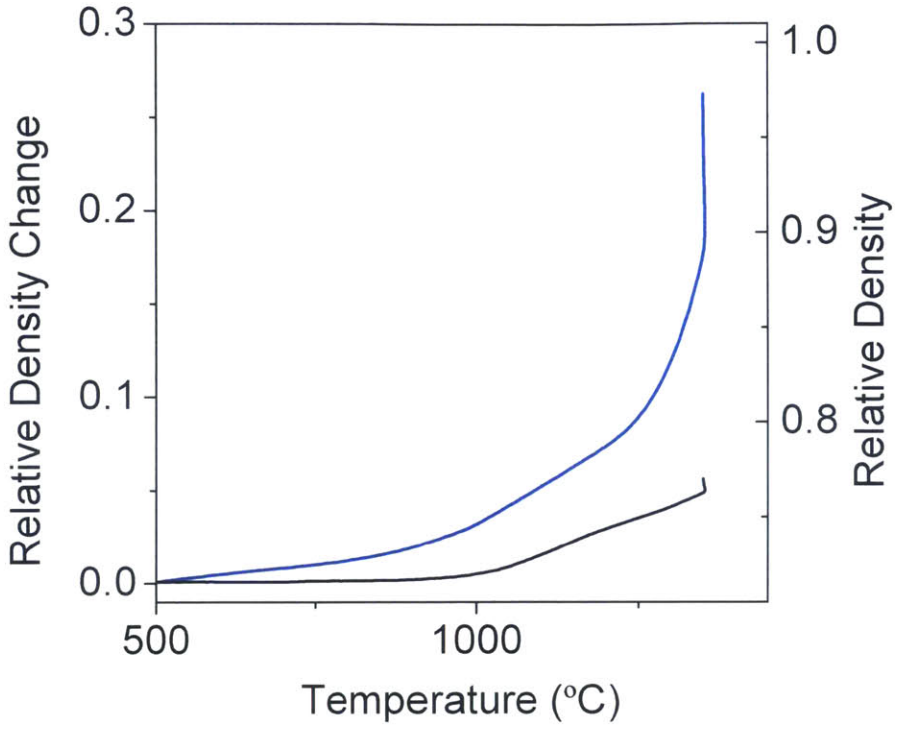

Figure 5.6 Change in relative density of nanocrystalline W-35 Ti-10 at.% Cr (blue) and W-35 at.% Ti (black).

The rapid rate of densification is more explicitly revealed as compared to the sintering of nanocrystalline W-35 at.% Ti (black line in Figure *5.6*) which does not possess an activator, Cr. Although nanocrystalline W-35 at.% Ti might retain nanoscale grain size after sintering based on the work of Chookajorn et al. (*56*), it does not display any sinterability and fails to form a bulk shape as shown in Figure *5.6*. The microstructure of nanocrystalline W-35 Ti-10 at.% Cr after sintering was observed through HR-SEM in Figure *5.7*, illustrating a grain size of about 100 nm at nearly full density.

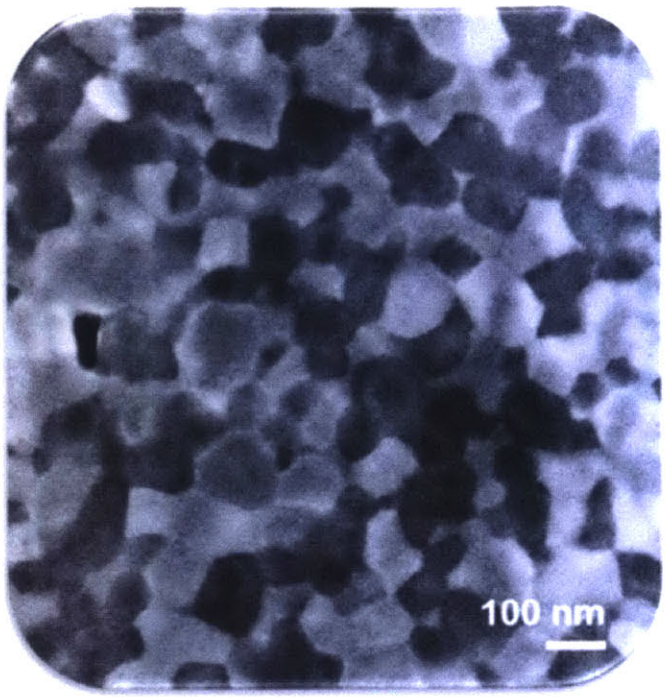

Figure 5.7 SEM image of a bulk (6 x 4 mm right cylinder) nanocrystalline W-Ti-Cr alloy shows a grain size of about 100 nm at nearly full density.

This particular sample had bulk dimensions of 6 mm diameter and 4 mm height; this is the first nanocrystalline tungsten alloy with such a combination of full density and fine grains produced in bulk through pressureless sintering of powders.

Grain sizes as a function of relative densities achieved using each sintering method: solid-state activated sintering, liquid phase sintering, and nano-phase separation sintering are presented in Figure *5.8*.

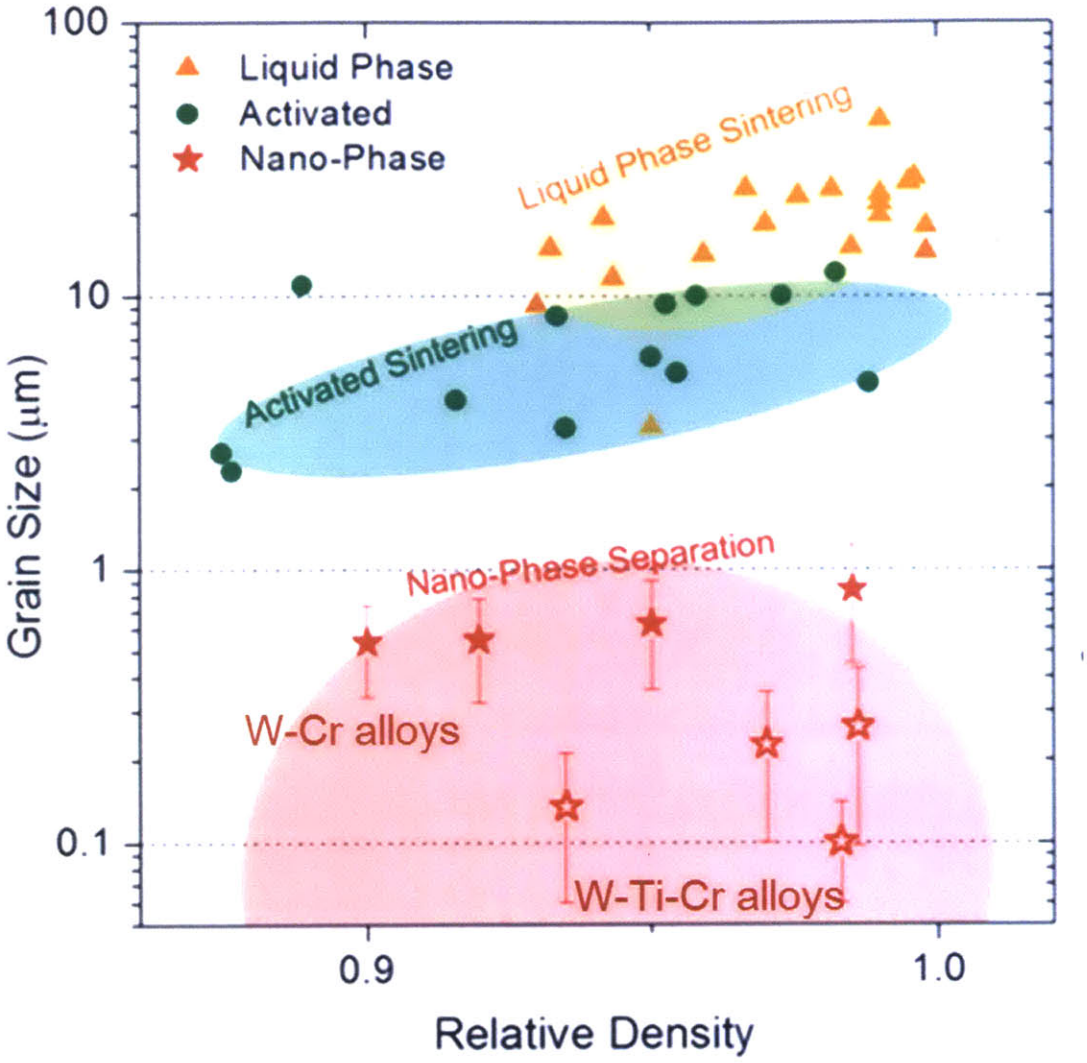

Figure 5.8 Further comparison of nano-phase separation sintering with liquid phase sintering and activated sintering of tungsten alloys as to grain size as function of relative density.

With the addition of a stabilizer element of Ti, the range of grain sizes accessible by nano-phase separation sintering is widened substantially, including into the nanoscale. Further optimization of alloy composition as well as the temperature-time cycle could allow a large measure of control over grain sizes.

Chapter 6 Concluding Remarks

New accelerated tungsten sintering method called nano-phase separation sintering is developed. Nano-phase separation sintering is demonstrated to be a method applicable to nanostructure tungsten alloys and to other nanostructure alloys as well. Finally, the control over grain sizes even to nanoscale dimensions of a sintered compact is permitted by nano-phase separation sintering. The significant conclusions elicited from this thesis are discussed below.

In Chapter 2, nanocrystalline W-15 at.% Cr alloy powder is synthesized through a high-energy ball mill. We show that the processed powder is comprised of micron-scale polycrystalline particles with nanoscale sub-grains; average particle and grain size is 1.2 μm and 12 nm, respectively. In addition, nanocrystalline W-15 at.% Cr is identified as a supersaturated solid solution after high-energy ball milling. This supersaturated solid solution does not align with the equilibrium phase diagram of W-Cr which expects almost no equilibrium solubility of chromium in tungsten at room temperature.

In Chapter 3, the compact of nanocrystalline W-15 at.% Cr is pressurelessly annealed and the onset of sintering at anomalously low temperature and the rapid rate of densification is confirmed. The role of nanoscale second phase precipitations during consolidation is analyzed by electron microscopy and x-ray diffraction. Accelerated sintering mechanism is established and named nano-phase separation sintering. The sintered compacts achieved through nano-phase separation sintering are identified to display much smaller grain sizes at comparable densities than those produced by conventional accelerated sintering methods such as solid-state activated sintering and liquid phase sintering.

In Chapter 4, thermodynamic conditions of nano-phase separation sintering are explored using a model binary phase diagram in order to establish the generality of the mechanism of nano-phase separation sintering. Based on the thermodynamic features discussed, nano-phase separation sintering is applied to chromium-nickel systems; with the addition of nickel, chromium consolidation is accelerated. The observation of a Ni-rich neck preferentially decorating particle surfaces and forming interparticle necks as well as assessed sintering activation energy explicitly implies that Ni-precipitates provide short-circuit diffusion paths to Cr atoms. This confirms the mechanism of nano-phase separation sintering.

In Chapter 5, nano-phase separation sintering is also identified as a method applicable to the production of nanocrystalline bulk tungsten alloys. Although the mechanism of nano-phase separation sintering is appropriate for the production of fine-grained materials, another element called a stabilizer might be necessary for further suppressing grain growth during a thermal cycle. By using Ti as a stabilizer, nanocrystalline bulk W-35 Ti-10 at.% Cr alloy is accomplished, showing a grain size of about 100 nm at nearly full density.

Powder consolidation has long been viewed as a prime route to form bulk nanocrystalline and ultrafine grained materials, but the challenges associated with rampant grain growth (*54*) and significant residual porosity (*55*) have delayed progress. In order to overcome such limitations, the field has seen a focusing tendency towards rapid consolidation methods assisted by large applied pressures (*55, 91, 92*) or pulsed electric current (*93, 94*), although limitations on component size and shape, as well as cost considerations, present complications for the broad usage of these techniques. It is our hope that nano-phase separation sintering, as a general new mechanism to accelerate sintering even in the absence of external forces, may broaden the opportunity for powder-route fabrication of bulk ultrafine and nanocrystalline alloys.

Chapter 7 Directions for Future Work

Some interesting future directions may be suggested:

- As shown in Figure *3.1*, the shrinkage of the nanocrystalline W-Cr compact exhibits a hump at initial stage. In-depth shrinkage studies at initial sintering stage would provide understandings of the shrinkage behavior of highly deformed alloys during annealing related to grain boundaries relaxation, recovery and etc. and how these affect its densification.
- Further optimization of alloy composition and time-temperature heating cycle including isothermal process for the sintering of W-Cr alloys could be explored to obtain full density sintered products with fine grain sizes. Studies of grain growth kinetics of the W-Cr system will help optimize processing parameters.
- A number of binary systems are provided in section 4.1 which expect to rapidly densify through nano-phase separation sintering; those alloy systems could be experimentally confirmed.

This study is mostly focused on establishing a new accelerated tungsten sintering method and succinctly touches on its application especially as to the production of nanocrystalline bulk tungsten alloys; further investigations below could provide some insights as to the design of sintering of nanocrystalline bulk alloys:

- There is no database of ternary phase diagram (W-Ti-Cr) at high temperature, which interrupts in-depth sintering studies of W-Ti-Cr alloys. Thus, construction of its ternary phase diagram could elucidate the role of phases present at high temperature in terms of accelerating densification and suppressing grain growth.

- The mechanical properties of nanocrystallline bulk tungsten alloys produced by nano-phase separation sintering method could be explored. Verification of shear localization will be crucial for the usage as kinetic energy penetrator materials.
- Optimization of alloy composition and time-temperature heating cycle for nanocrystalline bulk tungsten alloys could be investigated to achieve the best mechanical performance of tungsten alloys as to their deformation behavior.

References

1. E. Lassner, W.-D. Schubert, *Tungsten: properties, chemistry, technology of the elements, alloys, and chemical compounds*. (Springer, 1999).
2. S. W. Yih, C. T. Wang, *Tungsten: sources, metallurgy, properties, and applications*. (Plenum Press New York, 1979), vol. 500.
3. J. Vacek, Uber die Beeinflussung des Sinterverhaltens von Wolfram. *Methods of Influencing the Sintering Behaviour of Tungsten.) Planseeber. Pulvermet., bd* **7**, 6 (1959).
4. H. W. Hayden, J. H. Brophy, The Activated Sintering of Tungsten with Group-Viii Elements. *J Electrochem Soc* **110**, 805 (1963).
5. J. H. Brophy, H. W. Hayden, J. Wulff, Activated Sintering of Tungsten. *J Electrochem Soc* **108**, C182 (1961).
6. I. J. Toth, Lockingt.Na, Kinetics of Metallic Activation Sintering of Tungsten. *J Less-Common Met* **12**, 353 (1967).
7. R. M. German, Z. A. Munir, Enhanced Low-Temperature Sintering of Tungsten. *Metall Trans A* **7**, 1873 (1976).
8. R. M. German, Z. A. Munir, Systematic Trends in Chemically Activated Sintering of Tungsten. *High Temp Sci* **8**, 267 (1976).
9. R. M. German, V. Ham, Effect of Nickel and Palladium Additions on Activated Sintering of Tungsten. *Int J Powder Metall* **12**, 115 (1976).
10. J. H. Brophy, M. H. Kamdar, J. Wulff, The Ta-W-Re System. *T Metall Soc Aime* **221**, 1137 (1961).
11. I. Toth, N. Lockington, The kinetics of metallic activation sintering of tungsten. *Journal of the Less Common Metals* **12**, 353 (1967).
12. G. Samsonov, V. Yakovlev, Activation of the sintering of tungsten by the iron-group metals. *Soviet Powder Metallurgy and Metal Ceramics* **8**, 804 (1969).
13. G. Gessinger, H. Fischmeister, A modified model for the sintering of tungsten with nickel additions. *Journal of the Less Common Metals* **27**, 129 (1972).
14. W. Schintlmeister, K. Richter, "EFFECT OF NICKEL ON THE SINTERING AND SELF DIFFUSION OF TUNGSTEN" (Metallwerk Plansee AG, Reutte, Austria, 1970).
15. V. Panichkina, V. Skorokhod, A. Khrienko, Activated sintering of tungsten and molybdenum powders. *Soviet Powder Metallurgy and Metal Ceramics* **6**, 558 (1967).
16. G. Fletcher, M. James, J. Moon, The nickel activated sintering of tungsten. *Scripta Metall Mater* **5**, 105 (1971).
17. J. L. Johnson, R. M. German, Theoretical modeling of densification during activated solid-state sintering. *Metall Mater Trans A* **27**, 441 (Feb, 1996).
18. N. Hwang, Y. Park, D. Kim, D. Yoon, Activated sintering of nickel-doped tungsten: approach by grain boundary structural transition. *Scripta Mater* **42**, 421 (2000).
19. K. S. Hwang, H. S. Huang, Identification of the segregation layer and its effects on the activated sintering and ductility of Ni-doped molybdenum. *Acta Mater* **51**, 3915 (Aug 1, 2003).
20. J. Luo, V. K. Gupta, D. H. Yoon, H. M. Meyer, Segregation-induced grain boundary premelting in nickel-doped tungsten. *Appl Phys Lett* **87**, 231902 (Dec 5, 2005).
21. V. K. Gupta, D. H. Yoon, H. M. Meyer, J. Luo, Thin intergranular films and solid-state activated sintering in nickel-doped tungsten. *Acta Mater* **55**, 3131 (May, 2007).

22. R. M. German, *Sintering theory and practice*. (Wiley, New York, 1996), pp. xv, 550 p.
23. W. D. Kingery, Densification during Sintering in the Presence of a Liquid Phase .1. Theory. *J Appl Phys* **30**, 301 (1959).
24. S. J. L. Kang, K. H. Kim, D. N. Yoon, Densification and Shrinkage during Liquid-Phase Sintering. *J Am Ceram Soc* **74**, 425 (Feb, 1991).
25. R. M. German, *Liquid phase sintering*. (Plenum Press, New York, 1985), pp. xi, 240 p.
26. R. M. German, Microstructure of the gravitationally settled region in a liquid-phase sintered dilute tungsten heavy alloy. *Metall Mater Trans A* **26**, 279 (Feb, 1995).
27. S. M. Lee, S. J. L. Kang, Theoretical analysis of liquid-phase sintering: Pore filling theory. *Acta Mater* **46**, 3191 (May 22, 1998).
28. D. N. Yoon, W. J. Huppmann, Grain-Growth and Densification during Liquid-Phase Sintering of W-Ni. *Acta Metallurgica* **27**, 693 (1979).
29. J. K. Park, S. J. L. Kang, K. Y. Eun, D. N. Yoon, Microstructural Change during Liquid-Phase Sintering of W-Ni-Fe Alloy. *Metall Trans A* **20**, 837 (May, 1989).
30. J. S. C. Jang, J. C. Fwu, L. J. Chang, G. J. Chen, C. T. Hsu, Study on the solid-phase sintering of the nano-structured heavy tungsten alloy powder. *J Alloy Compd* **434**, 367 (May 31, 2007).
31. Z. W. Zhang, J. E. Zhou, S. Q. Xi, G. Ran, P. L. Li, Phase transformation and thermal stability of mechanically alloyed W-Ni-Fe composite materials. *Mat Sci Eng a-Struct* **379**, 148 (Aug 15, 2004).
32. H. J. Ryu, S. H. Hong, W. H. Baek, Microstructure and mechanical properties of mechanically alloyed and solid-state sintered tungsten heavy alloys. *Mat Sci Eng a-Struct* **291**, 91 (Oct 31, 2000).
33. K. S. Kumar, H. Van Swygenhoven, S. Suresh, Mechanical behavior of nanocrystalline metals and alloys. *Acta Mater* **51**, 5743 (Nov 25, 2003).
34. M. A. Meyers, A. Mishra, D. J. Benson, Mechanical properties of nanocrystalline materials. *Prog Mater Sci* **51**, 427 (May, 2006).
35. Q. Wei, S. Cheng, K. T. Ramesh, E. Ma, Effect of nanocrystalline and ultrafine grain sizes on the strain rate sensitivity and activation volume: fcc versus bcc metals. *Mat Sci Eng a-Struct* **381**, 71 (Sep 15, 2004).
36. Q. Wei, D. Jia, K. T. Ramesh, E. Ma, Evolution and microstructure of shear bands in nanostructured Fe. *Appl Phys Lett* **81**, 1240 (Aug 12, 2002).
37. D. Jia, K. T. Ramesh, E. Ma, Effects of nanocrystalline and ultrafine grain sizes on constitutive behavior and shear bands in iron. *Acta Mater* **51**, 3495 (Jul 16, 2003).
38. D. Jia, K. T. Ramesh, E. Ma, Failure mode and dynamic behavior of nanophase iron under compression. *Scripta Mater* **42**, 73 (Dec 17, 1999).
39. Q. Wei *et al.*, Mechanical behavior and dynamic failure of high-strength ultrafine grained tungsten under uniaxial compression. *Acta Mater* **54**, 77 (Jan, 2006).
40. L. S. Magness, High-Strain Rate Deformation Behaviors of Kinetic-Energy Penetrator Materials during Ballistic Impact. *Mech Mater* **17**, 147 (Mar, 1994).
41. L. S. Magness, D. Kapoor, R. Dowding, Novel Flow-Softening and Flow-Anisotropy Approaches to Developing Improved Tungsten Kinetic-Energy Penetrator Materials. *Mater Manuf Process* **10**, 531 (1995).
42. A. K. Zurek, P. S. Follansbee, A Comparison of Shear Localization Susceptibility in U-0.75 Wt Pct Ti and W-Ni-Fe during High-Strain Rate Deformation. *Metall Mater Trans A* **26**, 1483 (Jun, 1995).

43. Q. Wei, K. T. Ramesh, B. E. Schuster, L. J. Kecskes, R. J. Dowding, Nanoengineering opens a new era for tungsten as well. *Jom-Us* **58**, 40 (Sep, 2006).
44. Q. Wei *et al.*, Microstructure and mechanical properties of super-strong nanocrystalline tungsten processed by high-pressure torsion. *Acta Mater* **54**, 4079 (Sep, 2006).
45. A. G. Atkins, R. M. Caddell, The incorporation of work hardening and redundant work in rod-drawing analyses. *International Journal of Mechanical Sciences* **10**, 15 (1968).
46. R. Z. Valiev, R. K. Islamgaliev, I. V. Alexandrov, Bulk nanostructured materials from severe plastic deformation. *Prog Mater Sci* **45**, 103 (2000).
47. L. J. Kecskes *et al.*, Grain size engineering of bcc refractory metals: Top-down and bottom-up - Application to tungsten. *Mat Sci Eng a-Struct* **467**, 33 (Oct 15, 2007).
48. R. Malewar, K. S. Kumar, B. S. Murty, B. Sarma, S. K. Pabi, On sinterability of nanostructured W produced by high-energy ball milling. *J Mater Res* **22**, 1200 (May, 2007).
49. E. Y. Ivanov, C. Suryanarayana, B. D. Bryskin, Synthesis of a nanocrystalline W-25 wt.% Re alloy by mechanical alloying. *Mat Sci Eng a-Struct* **251**, 255 (Aug 15, 1998).
50. S. N. Alam, Synthesis and characterization of W-Cu nanocomposites developed by mechanical alloying. *Mat Sci Eng a-Struct* **433**, 161 (Oct 15, 2006).
51. S. S. Ryu, G. S. Kim, J. C. Kim, S. T. Oh, Y. Do Kim, The influence of annealing temperature on the microstructural development of W-Cu composite powder prepared by high-energy ball milling. *J Alloy Compd* **424**, 209 (Nov 9, 2006).
52. R. T. Ott, X. Y. Yang, D. E. Guyer, S. Chauhan, D. J. Sordelet, Synthesis of high-strength W-Ta ultrarine-grain composites. *J Mater Res* **23**, 133 (Jan, 2008).
53. E. Oda, H. Fujiwara, K. Ameyama, Nano grain formation in tungsten by severe plastic deformation-mechanical milling process. *Mater Trans* **49**, 54 (Jan, 2008).
54. J. S. Lian, R. Z. Valiev, B. Baudelet, On the enhanced grain-growth in ultrafine grained metals. *Acta Metall Mater* **43**, 4165 (Nov, 1995).
55. H. Gleiter, Nanocrystalline materials. *Prog Mater Sci* **33**, 223 (1989).
56. T. Chookajorn, H. A. Murdoch, C. A. Schuh, Design of Stable Nanocrystalline Alloys. *Science* **337**, 951 (Aug 24, 2012).
57. T. Chookajorn, M. Park, C. A. Schuh, Duplex nanocrystalline alloys: Entropic nanostructure stabilization and a case study on W-Cr. *Journal of Materials Research*, (*in press*).
58. P. E. A. Turchi, L. Kaufman, Z. K. Liu, Modeling of Ni-Cr-Mo based alloys: Part I - phase stability. *Calphad* **30**, 70 (Mar, 2006).
59. Z. C. Cordero, C. A. Schuh, Phase strength effects on chemical mixing in extensively deformed alloys. *Acta Mater* **82**, 123 (2015).
60. C. Suryanarayana, Mechanical alloying and milling. *Prog Mater Sci* **46**, 1 (2001).
61. T. Chookajorn, Massachusetts Institute of Technology. Department of Materials Science and Engineering., *Enhancing stability of powder-route nanocrystalline tungsten-titanium via alloy thermodynamics*. pp. 105 pages.
62. H. J. Fecht, Nanostructure formation by mechanical attrition. *Nanostruct Mater* **6**, 33 (1995).
63. D. B. Witkin, E. J. Lavernia, Synthesis and mechanical behavior of nanostructured materials via cryomilling. *Prog Mater Sci* **51**, 1 (Jan, 2006).
64. C. C. Koch, Materials Synthesis by Mechanical Alloying. *Annu Rev Mater Sci* **19**, 121 (1989).

65. A. R. Yavari, P. J. Desre, T. Benameur, Mechanically driven alloying of immiscible elements. *Phys Rev Lett* **68**, 2235 (Apr 6, 1992).
66. K. Uenishi, K. F. Kobayashi, K. N. Ishihara, P. H. Shingu, Formation of a super-saturated solid-solution in the Ag-Cu system by mechanical alloying. *Mat Sci Eng a-Struct* **134**, 1342 (Mar 25, 1991).
67. C. Gente, M. Oehring, R. Bormann, Formation of thermodynamically unstable solid-solutions in the Cu-Co system by mechanical alloying. *Phys Rev B* **48**, 13244 (Nov 1, 1993).
68. Z. C. Cordero *et al.*, Powder-Route Synthesis and Mechanical Testing of Ultrafine Grain Tungsten Alloys. *Metall Mater Trans A* **45A**, 3609 (Jul, 2014).
69. F. J. A. Broeder, Interface Reaction and a Special Form of Grain-Boundary Diffusion in Cr-W System. *Acta Metallurgica* **20**, 319 (1972).
70. D. Porter, The decomposition of tungsten-chromium solid solution. *Acta Metall Mater* **15**, 721 (1967).
71. Denbroed.Fj, W. G. Burgers, An X-Ray Diffraction Study of Decomposition of Tungsten-Chromium Solid Solution. *Acta Metall Mater* **16**, 265 (1968).
72. E. Lassner, W.-D. Schubert, *Tungsten : properties, chemistry, technology of the element, alloys, and chemical compounds*. (Kluwer Academic/Plenum Publishers, New York, 1999), pp. xix, 422 p.
73. G. C. Kuczynski, G. Matsumura, B. D. Cullity, Segregation in homogeneous alloys during sintering. *Acta Metallurgica* **8**, 209 (1960).
74. H. H. Hausner, Metal Powder Industries Federation., *Modern developments in powder metallurgy; proceedings*. (Plenum Press, New York, 1966), vol. 1.
75. H. H. Su, D. L. Johnson, Master sintering curve: A practical approach to sintering. *J Am Ceram Soc* **79**, 3211 (Dec, 1996).
76. J. D. Hansen, R. P. Rusin, M. H. Teng, D. L. Johnson, Combined-Stage Sintering Model. *J Am Ceram Soc* **75**, 1129 (May, 1992).
77. M. Park, K. C. Alexander, C. A. Schuh, Tungsten diffusion in chromium: Experiments and atomistic modeling. *J Alloy Compd* **611**, 433 (2014).
78. J. N. Mundy, S. J. Rothman, N. Q. Lam, H. A. Hoff, L. J. Nowicki, Self-diffusion in tungsten. *Phys Rev B* **18**, 6566 (1978).
79. S. M. Klotsman *et al.*, Chromium and Molybdenum Diffusion in Tungsten Single-Crystals. *Fiz Met Metalloved+* **67**, 767 (Apr, 1989).
80. L. E. Murr, *Interfacial phenomena in metals and alloys*. (Addison-Wesley Pub. Co., Advanced Book Program, Reading, Mass., 1975), pp. xiv, 376 p.
81. C. S. Nordahl, G. L. Messing, Sintering of alpha-Al2O3-seeded nanocrystalline gamma-Al2O3 powders. *J Eur Ceram Soc* **22**, 415 (Apr, 2002).
82. M. Kumagai, G. L. Messing, Controlled Transformation and Sintering of a Boehmite Sol-Gel by Alpha-Alumina Seeding. *J Am Ceram Soc* **68**, 500 (1985).
83. J. Luo, X. M. Shi, Grain boundary disordering in binary alloys. *Appl Phys Lett* **92**, (Mar 10, 2008).
84. J. Luo, H. K. Cheng, K. M. Asl, C. J. Kiely, M. P. Harmer, The role of a bilayer interfacial phase on liquid metal embrittlement. *Science* **333**, 1730 (Sep 23, 2011).
85. N. C. Kothari, Densification and Grain Growth during Liquid-Phase Sintering of Tungsten-Nickel-Copper Alloys. *J Less-Common Met* **13**, 457 (1967).

86. A. E. Nielsen, *Kinetics of precipitation*. International series of monographs on analytical chemistry, (Pergamon Press; distributed in the Western Hemisphere by Macmillan, Oxford, New York,, 1964), pp. x, 153 p.
87. K. Monma, H. Suto, H. Oikawa, Diffusion of Ni-63 and Cr-64 in Ni-Cr alloys. *J. Japan Inst. Metals* **28**, 188 (1964).
88. J. N. Mundy, C. W. Tse, W. D. Mcfall, Isotope-Effect in Chromium Self-Diffusion. *Phys Rev B* **13**, 2349 (1976).
89. T. Chookajorn, C. A. Schuh, Nanoscale segregation behavior and high-temperature stability of nanocrystalline W-20 at.% Ti. *Acta Mater* **73**, 128 (Jul, 2014).
90. H. Okamoto, Cr-Ti (chromium-titanium). *Journal of Phase Equilibria* **23**, 382 (2002).
91. S. C. Liao, W. E. Mayo, K. D. Pae, Theory of high pressure low temperature sintering of bulk nanocrystalline TiO2. *Acta Mater* **45**, 4027 (Oct, 1997).
92. H. Wang, Y. Z. Pei, A. D. LaLonde, G. J. Snyder, Weak electron-phonon coupling contributing to high thermoelectric performance in n-type PbSe. *P Natl Acad Sci USA* **109**, 9705 (Jun 19, 2012).
93. G. D. Zhan, J. D. Kuntz, J. L. Wan, A. K. Mukherjee, Single-wall carbon nanotubes as attractive toughening agents in alumina-based nanocomposites. *Nat Mater* **2**, 38 (Jan, 2003).
94. Y. Lee *et al.*, Contrasting role of antimony and bismuth dopants on the thermoelectric performance of lead selenide. *Nat Commun* **5**, (May, 2014).

Appendix A: Information of Samples for Control Experiments in the W-Cr System

We designed the series of control experiments in Figure 3.9 in order to establish that nano-phase separation sintering only occurs when powders with both (i) nanocrystalline internal grain sizes and (ii) alloy supersaturation are used. The control samples were intended to systematically test various W-Cr materials having feature (i) or (ii), but not both. All controls have micron-size particles (Table A.1 below) in order to remove particle size effects on the driving force and kinetics of sintering. The following table shows particles sizes of all control experiments including Cr-Ni systems.

Table A.1 Particle sizes of all control experiments including Cr-Ni systems.

Sample	Mean Size (μm)	Mode Size (μm)	Standard Deviation (μm)
nc-W(Cr)	1.25	0.94	0.74
nc-W	2.30	1.85	0.96
nc-W+15 at% Cr	1.09	1.07	0.71
Pure Cr	6.38	6.26	2.78
W(Cr)	4.99	5.45	2.30
W+15 at% Cr	3.35	2.77	1.42
nc-Cr(15 at% Ni)	4.75	4.78	2.22
nc-Cr(5 at% Ni)	5.09	4.79	2.33
nc-Cr	5.21	4.17	2.61
nc-Cr+5 at% Ni	3.41	2.79	2.35
Cr+5 at% Ni	5.06	4.79	3.17

Appendix B: Data and references corresponding to Figure 5.8

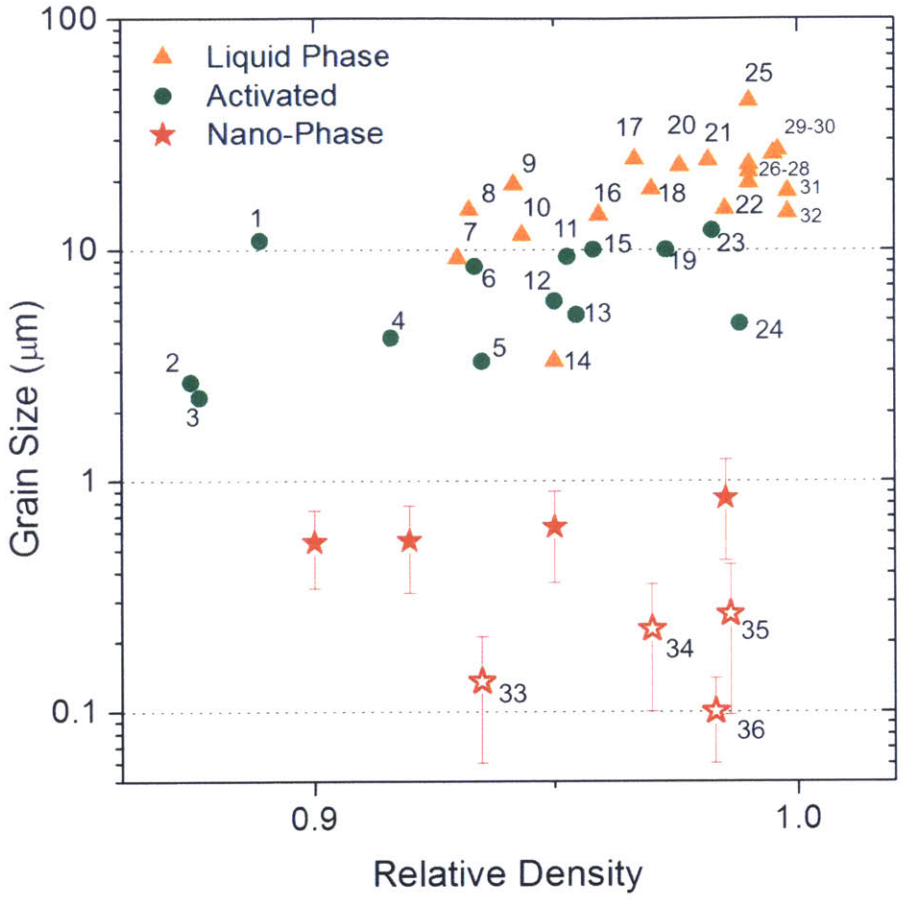

Figure B.1 Grain size versus density of sintered tungsten alloys with index numbers.

Table B.1 Data and References corresponding to Figure B.1.

Number	Materials	Grain size (μm)	Density	Ref.
1	W-1Ni	11	0.889	1
2	W-6Fe	2.68	0.874	2
3	W-8.4Ni-3.6Fe	2.3	0.876	3
4	W-2Fe	4.17	0.916	2
5	W-8.4Ni-3.6Fe	3.3	0.935	3

6	W-2Ni-2Fe	8.48	0.934	2
7	W-8Cu-3Ni	9.21	0.930	4
8	W-4Cu-7Ni	14.87	0.933	4
9	W-4Cu-7Ni	19.25	0.942	4
10	W-8Cu-3Ni	11.59	0.943	4
11	W-1Ni-1Fe	9.35	0.953	2
12	W-0.29Co	6	0.95	5
13	W-1Fe	5.24	0.955	2
14	W-9Cu-1Ni	3.3	0.95	6
15	W-6Ni	10.03	0.958	2
16	W-8Cu-3Ni	14.17	0.959	4
17	W-4Cu-7Ni	24.7	0.967	4
18	W-8Cu-3Ni	18.35	0.97	4
19	W-2Ni	10.03	0.973	2
20	W-4Cu-7Ni	23.1	0.976	4
21	W-8Cu-3Ni	24.47	0.982	4
22	W-1Ni-1Fe	15	0.985	7
23	W-1Ni	12.16	0.982	2
24	W-8.4Ni-3.6Fe	4.8	0.988	3
25	W-1Ni-1Fe	44	0.99	7
26	W-11.9Ni-5.1Fe	19.6	0.99	3
27	W-8.4Ni-3.6Fe	21.8	0.99	3
28	W-4.9Ni-2.1Fe	23.5	0.99	3
29	W-3.99Ni-1.71Fe	26	0.995	8
30	W-7Ni-3Fe	27	0.996	9
31	W-4Mo-7Ni-3Fe	17.9	1.00	9
32	W-8Mo-7Ni-3Fe	14.5	1.00	9
33	W-30Ti-10Cr	0.135	0.935	
34	W-15Ti-15Cr	0.227	0.97	
35	W-20Ti-15Cr	0.264	0.986	
36	W-35Ti-10Cr	0.1	0.983	

REFERENCES

1. Gupta VK, Yoon DH, Meyer HM, Luo J. Thin intergranular films and solid-state activated sintering in nickel-doped tungsten. Acta Mater 2007, 55(9): 3131-3142.
2. Amato I. On the mechanism of activated sintering of tungsten powders. Mater Sci Eng 1972, 10: 15-22.
3. Park SJ, Martin JM, Guo JF, Johnson JL, German RM. Grain growth behavior of tungsten heavy alloys based on the master sintering curve concept. Metall Mater Trans A 2006, 37A(11): 3337-3346.
4. Kothari NC. Densification and Grain Growth during Liquid-Phase Sintering of Tungsten-Nickel-Copper Alloys. J Less-Common Met 1967, 13(4): 457-468.
5. Li CJ, German RM. The Properties of Tungsten Processed by Chemically Activated Sintering. Metall Trans A 1983, 14(10): 2031-2041.
6. Johnson JL, German RM. Solid-state contributions to densification during liquid-phase sintering. Metall Mater Trans B 1996, 27(6): 901-909.
7. Park JK, Kang SJL, Eun KY, Yoon DN. Microstructural Change during Liquid-Phase Sintering of W-Ni-Fe Alloy. Metall Trans A 1989, 20(5): 837-845.
8. Lee WS, Chan TY. Microstructural Evolution and Mechanical Properties under High Strain Rate Testing of W-3.99Ni-1.71Fe Sintered by a Two-Stage Sintering Process. Mater Trans 2012, 53(7): 1318-1323.
9. Bose A, German RM. Microstructural Refinement of W-Ni-Fe Heavy Alloys by Alloying Additions. Metall Trans A 1988, 19(12): 3100-3103.

Appendix C: Diffusion of Tungsten in Chromium[4]

Because it is often used at elevated temperatures, diffusion in chromium has been studied experimentally, theoretically, and computationally for decades (*1-15*). Although there were some early discrepancies regarding the mechanisms and activation energy of Cr self-diffusion (*1, 10-12*), these were eventually resolved and Cr self-diffusion is now believed to follow the normal mechanisms identified for other BCC metals (*1, 10*), namely, monovacancy diffusion at lower temperatures, with a contribution from divacancy diffusion at higher temperatures (generally above about 1700 to 2000 K (*4, 14*)). Additionally, there exists a large body of work regarding diffusion in a number of Cr-alloys (*9, 16-22*). Diffusion in chromium-tungsten (Cr-W) alloys is among the least studied of these binary systems, with Ref. (*23*) providing the only discussion of it of which we are aware, and that being a qualitative analysis of Cr-W grain boundary diffusion.

As tungsten (W) is only mildly soluble in Cr, it is not surprising that this couple has not previously been given much attention. However, recent work on the stability of nanocrystalline alloys (*24, 25*) indicates that Cr-W is a good candidate system to form stable nanocrystalline phases (*24*). The possibility of fabricating nanocrystalline alloys with superior strength, hardness, and thermal stability in the Cr-W system is compelling, and nano-phase separation sintering occurring in W-Cr system also led to appreciate the need for a better understanding of the kinetics of the system. It is therefore the purpose of this study to address the gap in kinetic data in the literature for the diffusion of W in Cr.

In this study, Cr-W diffusion was investigated experimentally at temperatures in the range

[4] The contents of this appendix have been published previously in reference (*77*).

1526–1676 K in the low-concentration solid solution regime (i.e., W content below the solubility limit of ~30%) that is most relevant to applications of the Cr-W system.

Chromium discs (99.9% purity, 10 mm diameter, 5 mm thickness, from Alfa Aesar) were ground flat and parallel. To induce grain growth, the specimens were annealed at 1675 K for 24 hours. The final grain size was about 350–400 μm. A thin film (~1 μm) of high-purity tungsten (99.95%, from Alfa Aesar) was deposited on each disc by physical vapor deposition for 3 hours using an in-house sputter system operated under 155 W of RF power (from CESAR), while flowing 10 sccm Ar gas, with the chamber vacuum maintained below 10^{-7} Torr.

Each specimen was sealed in a quartz tube, first evacuated to 10^{-6} Torr using a turbo pump, and then backfilled with high-purity argon gas to 120 Torr. The sealed specimen was annealed in a furnace and exposed to temperatures of 1526, 1550, 1576, 1627, and 1676 K for 398, 212, 120, 48, and 22 hours, respectively. The diffusion depth in all cases was around 40 μm. After annealing, each specimen was laid on its side, embedded in an electrically conductive resin, and ground through half of its full width using an automatic polisher (TegraForce-5 from Struers) to expose the diffusion cross-section. A right angle between the side and top surface was achieved to within 0.2 degrees. An Electron Probe Micro Analyzer (EPMA, JXA-8200 from JEOL) was then used to obtain depth profiles of tungsten concentration in chromium. For each specimen, 5–12 concentration profiles were acquired, spaced at least 20 μm apart.

A cross section of a chromium disc after tungsten diffusion is shown in Figure C.1, where the image contrast from backscattered electrons and the inset energy-dispersive spectroscopy (EDS) map show the local tungsten content. The tungsten diffusion profile is uniform along the long axes of the specimen and approximates one-dimensional diffusion well.

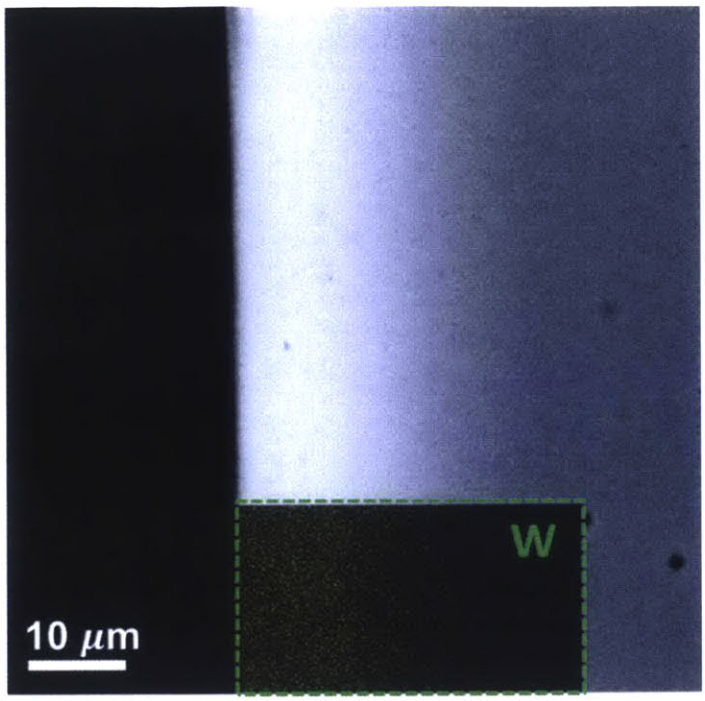

Figure C.1 Scanning electron microscopy (SEM) image taken in backscatter mode, for a chromium disc cross section after annealing at 1526 K. A tungsten elemental map from EPMA is shown in the inset.

Tungsten concentration as a function of diffusion depth at five different temperatures measured using EPMA is shown in Figure C.2.

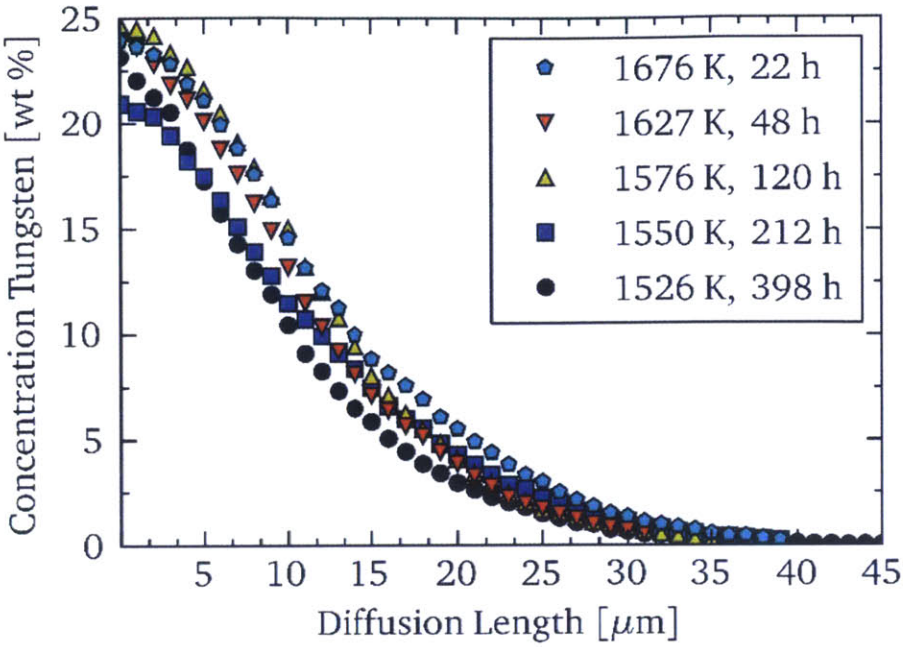

Figure C.2 Tungsten concentration versus penetration-distance at five different temperatures from EMPA measurements in a Cr−W diffusion couple. The diffusion length is zeroed at the initial Cr-W interface.

The diffusion of W into Cr in this experimental setup follows that for a semi-infinite one-dimensional solution of Fick's second law with a limited diffusant source:

$$C(x,t) = \frac{M}{\sqrt{\pi D t}} \exp\left(-\frac{x^2}{4Dt}\right) \tag{1}$$

Here, C is the concentration of tungsten at a distance x from the initial Cr-W interface after diffusion time t, and M is the total amount of deposited tungsten. D is the solute self-diffusion coefficient of tungsten in chromium. Concentration was converted to specific activity and is plotted vs. x^2 in Figure C.2.

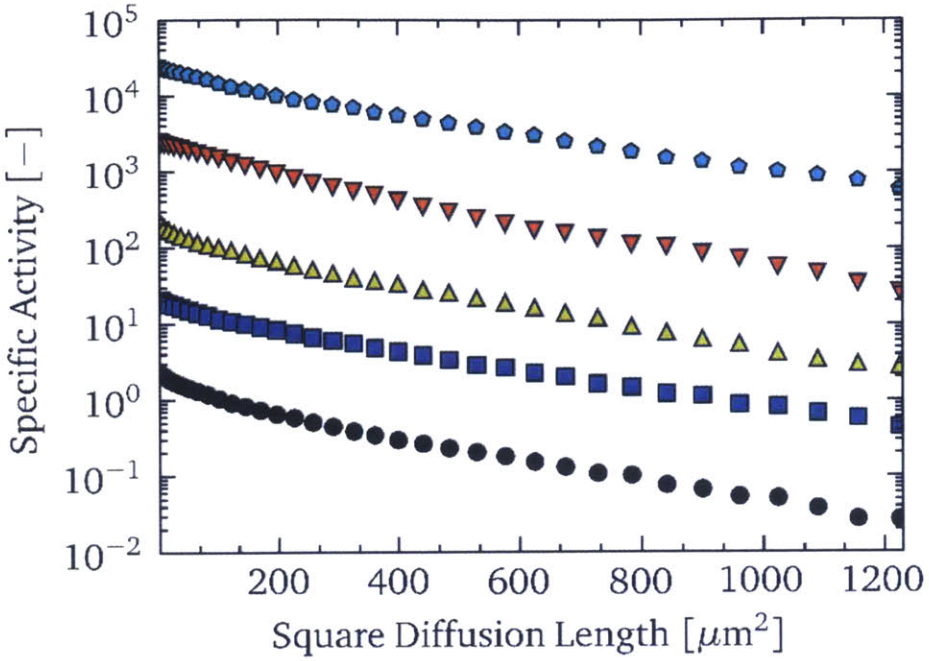

Figure C.3 Specific activity versus square-penetration-distance at five different temperatures, presented on a logarithmic scale.

Specific activity was obtained from concentration through division by the specimen density in any convenient units; for the data in Figure C.2, the units of density were chosen for each profile so as to provide uniform separation of the curves. From a fit of Eq. (1) to the data in Figure C.3 (with M treated as an unknown fitting parameter at each temperature), the diffusion coefficient was determined for each specimen (correlation coefficients $R^2 > 0.98$ were obtained for each profile), as listed in Table C.1, and an Arrhenius plot of $\ln D$ vs. $1/T$ is presented in Figure C.4. In Eq. (1), D is assumed to be independent of concentration; the use of this equation is valid in the present study because log (activity) vs x^2 was found to be linear and the thickness of the deposited solute layer was less than 1μm, which is much less than $(Dt)^{1/2}$ for every investigated temperature.

Table C.1 Measured solute diffusivity of tungsten in chromium at five temperatures

T [K]	D [m^2/s]	Diffusion Time [h]
1526	$5.27 \cdot 10^{-17}$	398.4
1550	$1.17 \cdot 10^{-16}$	212
1576	$2.24 \cdot 10^{-16}$	120
1627	$3.74 \cdot 10^{-16}$	48
1676	$1.08 \cdot 10^{-15}$	22

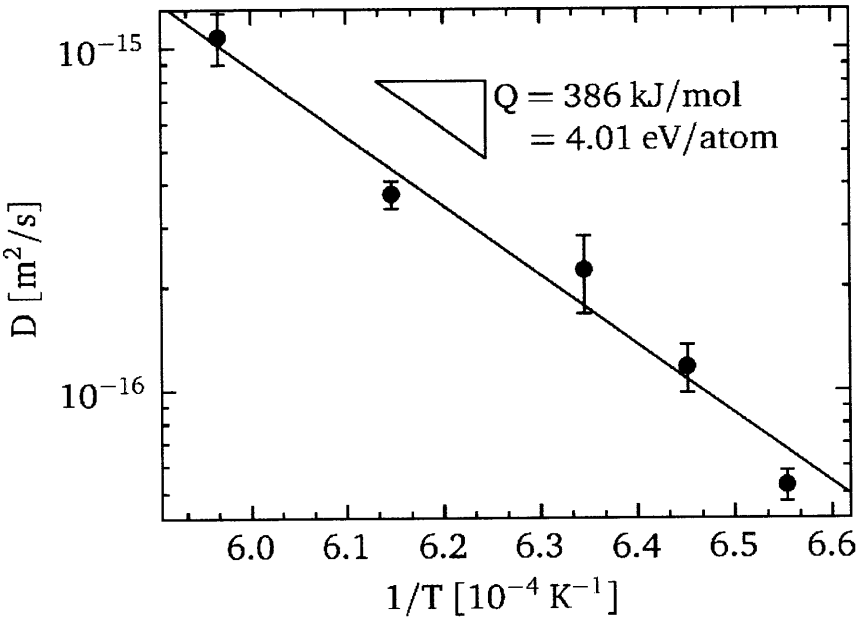

Figure C.4 Arrhenius plot of solute diffusion data for Cr−W diffusion experiments. Between 5−12 depth profiles are represented by each data point, and the error bars correspond to 95% confidence bounds on the mean value of the diffusivity calculated at each temperature.

The equation for the solute diffusion of tungsten in chromium can be described by an Arrhenius relationship:

$$D = D_0 \exp\left(-\frac{Q}{RT}\right) \tag{2}$$

A least squares regression analysis of the data from Figure C.4Figure C.4 yields the activation

energy, $Q = 386 \pm 33$ kJ/mol and the diffusion prefactor, $D_0 = A_0 \exp(-6.8 \pm 2.5)$ m^2/s where A_0 is the unit measure of diffusivity: 1 m^2/s, and the reported uncertainty ranges correspond to 95% confidence bounds.

REFERENCES

1. J. Askill, D. H. Tomlin, Self-Diffusion in Chromium. *Philos Mag* **11**, 467 (1965).
2. J. R. Stephens, W. D. Klopp, High-Temperature Creep of Polycrystalline Chromium. *J Less-Common Met* **27**, 87 (1972).
3. J. N. Mundy, C. W. Tse, W. D. Mcfall, Isotope-Effect in Chromium Self-Diffusion. *Phys Rev B* **13**, 2349 (1976).
4. J. L. Campbell, C. W. Schulte, Positron Trapping and Self-Diffusion Activation-Energies in Chromium. *Appl Phys* **19**, 149 (1979).
5. J. N. Mundy et al., Self-Diffusion in Chromium. *Phys Rev B* **24**, 658 (1981).
6. J. Johansson, A. Vehanen, J. Ylikauppila, P. Hautojarvi, P. Moser, Positron Lifetime Measurements on Electron-Irradiated Chromium. *Radiat Eff Lett* **58**, 31 (1981).
7. M. W. Finnis, J. E. Sinclair, A Simple Empirical N-Body Potential for Transition-Metals. *Philos Mag A* **50**, 45 (1984).
8. H. Schultz, Defect parameters of bcc metals: group-specific trends. *Materials Science and Engineering: A* **141**, 149 (1991).
9. J. Askill, Tracer diffusion in the chromium–nickel system. *physica status solidi (a)* **8**, 587 (1971).
10. A. Le Claire, Theory of impurity diffusion in metals: II. Homovalent impurities. *Philos Mag* **10**, 641 (1964).
11. W. C. Hagel, Self-Diffusion in Solid Chromium. *T Metall Soc Aime* **224**, 430 (1962).
12. H. Paxton, E. Gondolf, Cr Self-Diffusion Paxton Gondolf 1959. (2013).
13. P. Gruzin, S. Zemskiĭ, I. Rodina, J. Cornish, *Study of Diffusion of Carbon and Molybdenum in Chromium*. (Atomic Energy Research Establishment, 1965).
14. N. L. Peterson, Self-Diffusion in Pure Metals. *J Nucl Mater* **69-7**, 3 (1978).
15. A. D. Leclaire, Solute Diffusion in Dilute Alloys. *J Nucl Mater* **69-7**, 70 (1978).
16. G. Bonny, R. C. Pasianot, D. Terentyev, L. Malerba, Iron chromium potential to model high-chromium ferritic alloys. *Philos Mag* **91**, 1724 (2011).
17. J. Wallenius et al., Development of an EAM potential for simulation of radiation damage in Fe-Cr alloys. *J Nucl Mater* **329**, 1175 (Aug 1, 2004).
18. G. Bonny et al., On the mobility of vacancy clusters in reduced activation steels: an atomistic study in the Fe-Cr-W model alloy. *J Phys-Condens Mat* **25**, (Aug 7, 2013).
19. A. J. Mortlock, D. H. Tomlin, The Atomic Diffusion of Chromium in the Titanium-Chromium System. *Philos Mag* **4**, 628 (1959).
20. O. Fedchenko, S. Protsenko, P. Zukowski, M. Marszalek, Determination of diffusion

coefficients in film systems on the basis of Fe/Cr and Cu/Cr. *Vacuum* **86**, 1934 (Jul 20, 2012).
21. M. Danielewski, J. Dabek, S. Mrowec, G. Sieminska, Chemical Diffusion in Nonstoichiometric Chromium Sulfide, Cr2+Ys3. *Solid State Ionics* **17**, 331 (Nov, 1985).
22. J. Cermak, J. Ruzickova, A. Pokorna, Low-temperature tracer diffusion of chromium in Fe-Cr ferritic alloys. *Scripta Mater* **35**, 411 (Aug 1, 1996).
23. F. J. A. Broeder, Interface Reaction and a Special Form of Grain-Boundary Diffusion in Cr-W System. *Acta Metall Mater* **20**, 319 (1972).
24. T. Chookajorn, H. A. Murdoch, C. A. Schuh, Design of Stable Nanocrystalline Alloys. *Science* **337**, 951 (Aug 24, 2012).
25. H. A. Murdoch, C. A. Schuh, Stability of binary nanocrystalline alloys against grain growth and phase separation. *Acta Mater* **61**, 2121 (Apr, 2013).